

THESIS

SEEPAGE-INDUCED CONSOLIDATION TEST MINE TAILINGS

Submitted by

Zhengguang Tian

Department of Civil and Environmental Engineering

In partial fulfillment of the requirements

For the Degree of Master of Science

Colorado State University

Fort Collins, Colorado

Spring 2017

Master's Committee:

Advisor: Christopher A. Bareither

Co-Advisor: Joseph Scalia

Travis S. Bailey

Copyright by Zhengguang Tian 2017

All Rights Reserved

ABSTRACT

SEEPAGE-INDUCED CONSOLIDATION ON MINE TAILINGS

The objectives of this research were to design, construct, and evaluate the seepage induced consolidation testing (SICT) apparatus. Design of the SICT apparatus was based on existing apparatus at the University of Colorado-Boulder and University of British Columbia. Three materials were evaluated by the SICT and the odometer test to validate apparatus functionality: kaolin clay, fine synthetic tailings (FST), and average synthetic tailings (AST). This study consisted of the following tasks: (i) design and construction of the SICT apparatus; (ii) evaluation of geotechnical characteristics of kaolin clay, FST, and AST; (iii) conducting SICTs on kaolin clay, FST, and AST to determine the compressibility and hydraulic conductivity constitutive relationships; (iv) evaluation and comparison of the constitutive relationships of these materials with two constitutive models based on data from SICT; (v) conducting odometer tests on the same three materials to compare with results from the SICT; and (vi) evaluation of the effects of slurry composition on consolidation behavior (i.e., void ratio versus effective stress, $e-\sigma'$, and hydraulic conductivity versus void ratio, $k-e$).

The results of tasks *i-vi* support that the SICT apparatus constructed at Colorado State University (CSU) was reliable and repeatable based on benchmark tests conducted on kaolin clay. Constitutive relationship models generated from possible permutations of the seepage test and step loading test that comprise the SICT show a strong correlation. These models are compared to a composite model that combines all seepage and loading phases for a given SICT. The two models yield similar constitutive model parameters. Consolidation behavior ($e-\sigma'$ and $e-k$) of kaolin clay, FST and AST show a wide range of behavior due to the different material grain size distributions.

ACKNOWLEDGEMENTS

First, I would like to deeply thank my parents Shengjun Tian and Yan Xu for their deep love, care and support during my time at Colorado State University. I want you to know that you are both my heroes because you gave the best to me and my dear brother, He Tian, during every hard time. Also, I would like to let my brother know that I enjoyed every moment we spent together. I miss all the times we would fish, play video games, and fight together.

Second, I would like to dedicate this thesis to my advisor, Dr. Christopher Bareither, who provided constant support and guidance throughout my Master's thesis, and also spent time with me teaching me English.

Third, I would like to thank my co-advisor, Dr. Joseph Scalia, who gave me constant help on laboratory tests, thesis, and also organized all kinds of Geo-Events to bring us together as a group. I am glad that a new member, Lillian, arrived in our Geo-Family. She is adorable. I would also like to extend my thanks to Dr. Charles Shackelford, who believed in my abilities and Dr. Travis Bailey for serving on my graduate committee.

Fourth, I would like to thank my research colleagues at Colorado State University for their assistance with my laboratory work including Wesley Herweynen, Iman Babazadeh, Joe Wilmetti, Mohammad H. Gorakhki, Shahin Ghazizadeh, and Matteus Hamade.

Last, but not least, I would like to sincerely thank my brothers and sisters at Summitview Community Church for their love, care and prayers during my time in Fort Collins. You gave me a second family in the United States and I love and thank you all.

TABLE OF CONTENTS

ABSTRACT	ii
ACKNOWLEDGEMENTS	iii
LIST OF TABLES	vi
LIST OF FIGURES.....	vii
LIST OF SYMBOLS	xi
CHAPTER 1: INTRODUCTION	1
1.1 Research Motivation	1
1.2 Objectives and Scope of Research	2
CHAPTER 2: BACKGROUND	4
2.1 Mining Tailings	4
2.2 Tailings Behavior within a Tailings Impoundment	4
2.3 Consolidation Theory	5
2.3.1 Coordinate Systems.....	5
2.3.2 Large-Strain Consolidation Theory.....	6
2.3.3 Constitutive Relationships.....	9
2.4 Principle of Seepage Force.....	9
CHAPTER 3: SEEPAGE-INDUCED CONSOLIDATION APPARATUS	15
3.1 Equipment Overview	14
3.1.1 Loading Frame.....	15
3.1.2 Specimen Pedestal and Casing.....	15
3.1.3 Load Platen	16
3.1.4 Linear Variable Displacement Transducers	16
3.1.5 Seepage Control.....	17
3.1.6 Data Acquisition and Measurement	18
CHAPTER 4: MATERIALS AND METHOD	24
4.1 Materials.....	24
4.2 Methods	25
4.2.1 Sedimentation Test	25
4.2.2 Slurry Preparation	26

4.2.3 Odometer Test.....	26
4.2.4 Seepage-Induced Consolidation Test.....	28
4.2.5 Calculation of Compressibility and Permeability for a SICT	29
CHAPTER 5: RESULTS AND DISCUSSION	37
5.1 Consolidation Behavior in the SICT and Odometer	37
5.1.1 Seepage-Induced Consolidation.....	37
5.1.2 Oedometer Testing	41
5.1.3 Consolidation Comparison.....	42
5.2 Repeatability of the SICT	42
5.3 Slurry Composition Effects on Consolidation	44
5.3.1 Seepage-Induced Consolidation Data	44
5.3.2 Odometer Testing.....	45
5.3.3 Consolidation Comparison.....	46
5.4 Constitutive Relationships	47
5.5 Slurry Compositions and Constitutive Relationships	48
CHAPTER 6: SUMMARY AND CONCLUSION.....	81
REFERENCES	83
APPENDIX A: SEEPAGE-INDUCED CONSOLIDATION TESTING	87
A.1 Saturation of Lines	87
A.2 Sample Preparation	93
A.3 Seepage Phase	99
A.4 Step Loading Phase	102
A.5 Post Test.....	106
APPENDIX B: SICT CALIBRATIONS.....	107
B.1 Spring-return LP Calibration.....	107
B.2 Load Cell Calibration	110
APPENDIX C: VOID RATIO AT ZERO EFFECTIVE STRESS.....	112

LIST OF TABLES

Table 4.1 Physical characteristics and classification of natural and synthetic tailings (Alhomair 2016).....	32
Table 5.1 Material Properties of Slurry Samples in SICT and Odometer Test.	73
Table 5.2 SICT Experimental Results on Kaolin-1 at Steady State.....	74
Table 5.3 Experimental Results of Kaolin from Odometer Test.	75
Table 5.4 SICT Experimental Results on Kaolin-2 at Steady State.....	76
Table 5.5 SICT Experimental Results on Kaolin-3 at Steady State.....	77
Table 5.6 SICT Experimental Results on FST at Steady State.....	78
Table 5.7 SICT Experimental Results on AST at Steady State.....	79
Table 5.8 Experimental Results of FST from Odometer Test.	80
Table 5.9 Experimental Results of AST from Odometer Test.	80

LIST OF FIGURES

Fig. 2.1.	Schematic of coordinate system for (a) Eulerian coordinate system, definitions: x = Eulerian coordinate distance of fixed element from datum plane, (b) Lagrangian coordinate system, definitions: t_0 = initial state Lagrangian coordinate, and $\xi(a,t)$ = convective coordinate as function of a and time t , δa = thickness of PQRS element, and $\delta \xi$ = thickness of PQRS element.....	12
Fig. 2.2.	Phase relation of soil element. Definitions: z = solids coordinate, e_i = initial void ratio.....	13
Fig. 2.3.	Prepared slurry consolidates (a) under a downward water flow caused by a constant head difference and (b) stress state of soil element due to seepage force..	14
Fig. 3.1.	Photograph of the seepage-induced consolidation apparatus	20
Fig. 3.2.	Schematic of the seepage-induced consolidation apparatus	21
Fig. 3.3.	Cross-section and plan view schematics of the specimen pedestal (dimensions in mm)..	22
Fig. 3.4.	Cross-section and plan view schematics of the load platen (dimensions in mm)	23
Fig. 4.1.	Particle-size distribution for fine synthetic tailings, average synthetic tailings, and the upper-bound, lower-bound, and average from compiled mine tailings particle-size distribution (Alhomair et al., 2016).....	33
Fig. 4.2.	(a)Overall diagram of odometer at CSU, and (b) cross section view of confining ring	34
Fig. 4.3.	Soil profile of testing specimen. Soil column is divided into N layers when slurry sample is poured into sample casing and each layer has same thickness.....	35
Fig. 4.4.	Flow Chart of SICT Analysis.....	36
Fig. 5.1.	Experimental data of kaolin-1 during SICT: (a) differential pressure across the testing specimen versus time, Δu -max is the maximum excess pore water pressure generated at the bottom of testing specimen (b) deformation versus time; σ'_0 is the sum of self-weight of slurry sample and surcharge load caused by load platen, two extension rods and two LPs. Note: flow rate and applied load for each seepage are provided in Table 5.2.....	49
Fig. 5.2.	Distributions of (a) void ratio, and (b) hydraulic conductivity for kaolin-1 during self-weight and seepage induced consolidation processes at steady state	50
Fig. 5.3.	Constitutive relationships of kaolin-1 (a) effective stress-void ratio relationship (b) hydraulic conductivity-void ratio relationship.....	51
Fig. 5.4.	Experimental data of kaolin-1 during odometer test: (a) bottom pressure versus time (b) deformation versus time; σ'_a is the applied load.....	52
Fig. 5.5.	Constitutive relationships of kaolin-1 in SICT and odometer test (a) effective stress-void ratio relationship (b) hydraulic conductivity-void ratio relationship.....	53

Fig. 5.6.	Experimental data of kaolin-2 during SICT: (a) differential pressure across the testing specimen versus time, Δu -max is the maximum excess pore water pressure generated at the bottom of testing specimen (b) deformation versus time; σ'_0 is the sum of self-weight of slurry sample and surcharge load caused by load platen, two extension rods and two LPs. Note: flow rate and applied load for each seepage are provided in Table 5.3.	54
Fig. 5.7.	Experimental data of kaolin-2 during SICT: (a) differential pressure across the testing specimen versus time, Δu -max is the maximum excess pore water pressure generated at the bottom of testing specimen (b) deformation versus time; σ'_0 is the sum of self-weight of slurry sample and surcharge load caused by load platen, two extension rods and two LPs. Note: flow rate and applied load for each seepage are provided in Table 5.4.	55
Fig. 5.8.	Compilation of percentage pressure change and deformation of three kaolin clay (a) percentage of pressure change for each step loading test (b) deformation of three kaolin clay throughout SICT.	56
Fig. 5.9.	Compilation of variations of void ratio (e) and hydraulic conductivity (k) along soil profile for (a) kaolin-2 (e versus depth), (b) kaolin-2 (k versus depth), (c) kaolin-2 (e versus depth), and (d) kaolin-3 (k versus depth). Variations of e and k of these three materials are at steady state.	57
Fig. 5.10.	Constitutive relationships of kaolin-2 in SICT and odometer test (a) effective stress-void ratio relationship (b) hydraulic conductivity-void ratio relationship.	58
Fig. 5.11.	Constitutive relationships of kaolin-3 in SICT and odometer test (a) effective stress-void ratio relationship (b) hydraulic conductivity-void ratio relationship.	59
Fig. 5.12.	Experimental data of kaolin-2 during SICT: (a) differential pressure across the testing specimen versus time, Δu -max is the maximum excess pore water pressure generated at the bottom of testing specimen (b) deformation versus time; σ'_0 is the sum of self-weight of slurry sample and surcharge load caused by load platen, two extension rods and two LPs. Note: flow rate and applied load for each seepage are provided in Table 5.5.	60
Fig. 5.13.	Experimental data of kaolin-2 during SICT: (a) differential pressure across the testing specimen versus time, Δu -max is the maximum excess pore water pressure generated at the bottom of testing specimen (b) deformation versus time; σ'_0 is the sum of self-weight of slurry sample and surcharge load caused by load platen, two extension rods and two LPs. Note: flow rate and applied load for each seepage are provided in Table 5.6.	61
Fig. 5.14.	Distributions of (a) void ratio, and (b) hydraulic conductivity for FST during self-weight and seepage consolidation process at steady state.	62
Fig. 5.15.	Distributions of (a) void ratio, and (b) hydraulic conductivity for AST during self-weight and seepage consolidation process at steady state.	63
Fig. 5.16.	Bottom pressure of FST in odometer test; \square 'a is the applied load.	64
Fig. 5.17.	Deformation of AST and FST in odometer test.	65
Fig. 5.18.	Constitutive relationships of FST in SICT and odometer test (a) effective stress-void ratio relationship (b) hydraulic conductivity-void ratio relationship.	66

Fig. 5.19. Constitutive relationships of AST in SICT and odometer test (a) effective stress-void ratio relationship (b) hydraulic conductivity-void ratio relationship.....	67
Fig. 5.20. Compilation of constitutive relationship models of three kaolin clay (a) effective stress-void ratio relationship (b) hydraulic conductivity-void ratio relationship.....	68
Fig. 5.21. Compilation of composite models for (a) kaolin-2 (e versus effective stress), (b) kaolin-2 (e versus k), (c) kaolin-3 (e versus effective stress), and (d) kaolin-3 (e versus k).	69
Fig. 5.22. Composite models for FST (a) effective stress-void ratio relationship, (b) hydraulic conductivity-oid ratio relationship.....	70
Fig. 5.23. Composite models for AST (a) effective stress-void ratio relationship, (b) hydraulic conductivity-void ratio relationship	71
Fig. 5.24. Compilation of constitutive relationships of kaolin, FST and AST (a) effective stress-void ratio relationship (b) hydraulic conductivity-void ratio relationship.....	72
Fig. A.1. Apply vacuum grease to the edge of the sample pedestal.....	87
Fig. A.2. Filter paper and porous stone on top of the pedestal.....	88
Fig. A.3. Valve 12 connects the pump to the sample; Valve 11 connects to the pressure transducer.	88
Fig. A.4. Removal of air bubbles at in line pressure transducers	89
Fig. A.5. Removal of air bubbles from syringe	90
Fig. A.6. Pump Setup	91
Fig. A.7. Removal of air from lines between sample and pump	92
Fig. A.8. Placing slurry in sample casing	93
Fig. A.9. Shaking of specimen to provide level surface and remove any voids.	93
Fig. A.10. Placement of filter paper on top of specimen.....	94
Fig. A.11. Carefully placing water on top of sample using a syringe to avoid disturbance.....	94
Fig. A.12. Specimen with filter paper and porous plastic disc.	95
Fig. A.13. Specimen with loading plate in place	95
Fig. A.14. Top cap in place on top of sample casing.	96
Fig. A.15. LPs, extension rods and load shaft in place	97
Fig. A.16. Button to zero LPs.....	97
Fig. A.17. Flushing air out of line between top of sample and Mariotte bottle.	98
Fig. A.18. Display on flow pump (left), infusion/withdraw directions (right).....	99
Fig. A.19. Bubbles will appear in the line connected to valve 12.....	100
Fig. A.20. Example of steady state after seepage phase.....	101
Fig. A.21. Location of valve 2.	102
Fig. A.22. Selection of manual or control option for specifying load.....	103
Fig. A.23. Example output showing steady state after step load phase	104

Fig. A.24. Example of steady state being reached during hydraulic conductivity test.....	105
Fig. B.1. LP calibration device.....	108
Fig. B.2. Calibration curve for (a) left LP, (b) right LP	109
Fig. B.3. Calibration curve for load cell.....	111
Fig. C.1. The relationship between e_0 and aspect ratio of container	113

LIST OF SYMBOLS

LIR	load increment ratio	FST	fine synthetic tailings
AST	average synthetic tailings	$SICT$	seepage-induced consolidation test
LL	liquid limit	PI	plasticity index
d_{max}	maximum particle size	G_s	specific gravity
SC	solid content	e	void ratio
e_i	initial void ratio	e_0	void ratio at zero effective stress
e_f	final void ratio	U_{top}	top pressure of soil specimen
U_{bottom}	bottom pressure of soil specimen	$i_{ave.}$	hydraulic gradient across the specimen
σ'_0	initial load condition	σ'_a	applied load
σ'_s	seepage stress	σ'_f	final total stress
Q	flow rate	v	Darcy velocity
H_f	final sample height	k_{tf}	final hydraulic conductivity at surface of slurry
k_{mf}	final hydraulic conductivity at middle of slurry	k_{bf}	final hydraulic conductivity at bottom of slurry
e_{tf}	final void ratio at surface of slurry	e_{mf}	final void ratio at middle of slurry
e_{bf}	final void ratio at bottom of slurry	c_v	coefficient of consolidation
a_v	coefficient of compressibility	k_f	final hydraulic conductivity

CHAPTER 1: INTRODUCTION

1.1 Research Motivation

In the mining industry, large volumes of mine waste are generated during ore extraction processes, and often these waste materials are subsequently stored in perpetuity in waste management facilities. Mine tailings are a fine-grained, high water content waste generated from the crushing, grinding, and chemical processing of ore. Current mining operations are exploiting low-grade ores bodies due to the exhaustion of most high-grade ores. Mining low-grade ores increases significantly the volume of mine tailings generated due to the additional volume of rock that must be mined and processed to meet required economies of scale (West 2011).

Mine tailings commonly are generated as slurry and deposited in tailings storage facilities (TSFs) whereby solid particles experience flocculation, sedimentation, and self-weight consolidation (Bonin et al. 2014). Effective management of mine tailings in a given TSF requires an understanding of the physical changes in the material to facilitate activities ranging from daily management to final closure. Following deposition of tailings in a TSF, mine tailings will transition from slurry to soil as effective stress increases producing decreased volume and strength gain. These changes are controlled by consolidation, which is the process of dissipation of pore water due to hydraulic gradients induced from changes in excess pore water pressure. Constitutive relationships between void ratio (i.e. density), hydraulic conductivity, and effective stress are essential to understand the current state (density and stress) and changes in physical processes of mine tailings during consolidation.

The two frameworks to apply mathematical formulations to the consolidation process include small-strain theory and large-strain theory. Small-strain consolidation theory is based on an assumption that soil parameters for compressibility and hydraulic conductivity are constant during the consolidation process. In contrast, large-strain consolidation theory is based on

constitutive relationships between (i) void ratio and effective stress and (ii) hydraulic conductivity and void ratio to relate changes in effective stress to changes in material properties. A prediction of large-strain consolidation requires these compressibility and hydraulic conductivity constitutive relationships that characterize material behavior from initial effective stress (i.e., transition from slurry to soil) to higher effective stresses anticipated at depth in a full-scale TSF.

The seepage-induced consolidation test (SICT) is a laboratory methodology to measure constitutive relationships for slurried materials (Znidarcic et al. 2011). The underlying principle of the experiment is to use seepage at a controlled rate to induce changes in effective stress in a slurry material through a seepage drag force. Seepage forces can be precisely controlled, allowing for accurate application of low effective stresses. Thus, void ratio and hydraulic conductivity can be assessed in the low effective stress range (e.g., 0.1 kPa to 10 kPa) where pronounced changes in material behavior occur. Although the SICT is not a common laboratory experiment (e.g., no ASTM standard exists for the SICT), the methodology has been shown to effectively measure compressibility and hydraulic conductivity for a broad range of slurried geomaterials, including coal combustion residuals and mine tailings (e.g., Znidarcic et al. 2011; Estepho 2014).

1.2 Objectives and Scope of Research

The objectives of this research were to design, construct, and evaluate a SICT apparatus. Evaluation was completed via compressibility and permeability relationships for three materials tested in a traditional odometer (ASTM D2435) and with a SICT apparatus developed at Colorado State University (CSU). The following tasks were completed as part of this research:

- design and construction a SICT apparatus;
- evaluation of geotechnical characteristics for kaolin clay and two synthetic mine tailings;

- conducting SICTs on these three materials to determine the compressibility and hydraulic conductivity constitutive relationships; and
- conducting odometer tests (ASTM D2435) on the same three materials for comparison.

CHAPTER 2: BACKGROUND

2.1 Mine Tailings

There are three general types of tailings in the mining industry that are differentiated based on engineering characteristics: (i) hard rock tailings, (ii) phosphate tailings, and (iii) oil sand tailings. Hard-rock mine tailings are composed predominantly of sand- to silt-sized particles and exhibit high rates of particle setting and the smallest magnitudes of consolidation of the three types of tailings (Carrier et al. 1983). Phosphate mining produces tailings composed of phosphatic clay that has high plasticity indices in the range of 70 to 150 (Carrier et al. 1983). In general, phosphate tailings will achieve solids content of approximately 12% to 15% within 3 to 30 months following deposition (Znidarcic et al. 1992). Oil sand tailings are generated from the extraction of bitumen and are a mixture of sediment, bitumen, and water. Sediments consist of sand, silt, and clay, with the clay components consisting predominately of kaolinite and illite and a small amount of illite/smectite, and the typical bitumen and solids contents are 10% and 5% by total mass, respectively (Chalaturnyk et al. 2002; BGC Engineering 2010).

2.2 Tailings Behavior within a Tailings Impoundment

Mine tailings discharged into a TSF will experience flocculation, sedimentation, and self-weight consolidation (Imai 1981; Been and Sills 1981; Schiffman et al. 1988; Priscu 1999). Coarser and finer particles of the tailings tend to segregate following slurry deposition with coarser materials settling first to form a beach slope and finer particles flowing towards the lowest point of the TSF. Finer solid particles will form a dense fluid or slurry (Bonin et al. 2014) and flocculants present in the pore water promote development of fine-grained particle flocs via electro-chemical bonding (Mitchell 1976). This bonding aids in densifying particles to promote sedimentation and transition from slurry to soil, whereby effective stress develops via physical contacts between adjacent particles (Imai 1981). Continuation of this process will lead to particle

aggregation, increased effective stress, and consolidation. Consolidation due to self-weight of the tailings can require years to complete as compared to a few days for sedimentation; therefore, self-weight consolidation of mine tailings is commonly evaluated in lieu of sedimentation when assessing storage capacity of a given TSF (Znidarcic 1999).

2.3 Consolidation Theory

Consolidation is a time-dependent process that involves a reduction in total volume via expulsion of water from the void space of saturated soils due to excess pore water pressure (Terzaghi 1925; Taylor 1948). One-dimensional consolidation theory, also known as small-strain consolidation, was first proposed by Terzaghi (1925). The theory is based on the assumption that only small strains develop in a consolidating soil and the compressibility and hydraulic conductivity parameters are constant during the consolidation process. However, slurry materials (e.g., mine tailings) undergo large-strain consolidation such that compressibility and hydraulic conductivity will change during the consolidation process as a function of effective stress and the assumptions of small-strain consolidation theory are violated (Koppula 1970; Znidarcic 1982; Carrier et al. 1983; Caldwell et al. 1984; Abu-Hejleh et al. 1996; Fox and Berles 1997). Gibson et al. (1967) proposed a large-strain consolidation theory to predict the deformation behavior of slurry materials. Subsequently, laboratory experiments have been conducted that document the validity of large-strain consolidation theory to a broad range of geomaterials (Znidarcic 1982; Znidarcic 1983; Carrier et al. 1983; Pollock 1988; Huerta et al. 1988; Suthaker 1995; Znidarcic 2011; Jerravipoolvarn 2005; Azam 2011; Estepho 2014).

2.3.1 Coordinate Systems

Eulerian and Lagrangian coordinate systems applied to consolidation are shown in Fig. 2.1. Eulerian coordinates (x, t), also known as conventional coordinates, are used in the governing equation for small-strain consolidation, whereas Lagrangian coordinates (a, t) are

used in the governing equation of large-strain consolidation. In Eulerian coordinates, a given point of interest is defined at a distance x from a datum (Fig. 2.1a). As the soil consolidates under an external load, the mass of solids within a given soil element defined by boundaries $(x, x+dx)$ is assumed to remain constant. Although this assumption is relevant for small-strains, the mass within an analogous soil element applied to a large-strain consolidation problem will not remain constant. Thus, a “moving boundary” in Lagrangian coordinates was adopted for large-strain consolidation to create a more numerically stable governing equation (Lee 1979).

Lagrangian coordinates for the consolidation example are shown in Fig. 2.1b are fixed with respect to the mass of solids within a given soil element. The volume change of a given soil element is equal to the change in water volume. The initial soil element (P_0, Q_0, R_0, S_0) before consolidation has a Lagrangian coordinate $a = \xi(a, 0)$ relative to the datum, whereas for a given time (t) during consolidation, the soil element has coordinate $a = \xi(a, t)$ relative to the datum (Fig. 2.1b). Gibson et al. (1967) introduced a solids coordinate (z) shown in Fig. 2.2 to define the volume of solids per unit area within the soil layer, which does not change during consolidation. Thus, the Lagrangian coordinates within the soil element can be simplified as shown in Fig. 2.2 and the change in volume of the system is equivalent to the change in void volume.

2.3.2 Large-Strain Consolidation Theory

The large-strain consolidation theory developed by Gibson et al. (1967) overcomes many limiting assumptions of small-strain consolidation theory. Lagrangian coordinates were used to develop a 1-D large-strain consolidation equation that incorporates changes in compressibility and hydraulic conductivity during consolidation (Schiffman et al. 1988). Key assumptions in the large-strain consolidation equation include the following: (i) the soil skeleton is homogeneous and creep does not occur during consolidation; (ii) soil solids and fluid are incompressible; and (iii) the principle of effective stress (σ') is valid (i.e., $\sigma' = \sigma - u$, where u is

pore water pressure and σ is total stress). Based on these assumptions, Gibson et al. (1967) presented the following governing equation for large-strain consolidation:

$$\pm \left(\frac{\rho_s}{\rho_f} - 1 \right) \frac{d}{de} \left[\frac{k(e)}{1+e} \right] \frac{\partial e}{\partial z} + \frac{\partial}{\partial z} \left[\frac{k(e)}{\rho_f(1+e)} \frac{d\sigma'}{de} \frac{\partial e}{\partial z} \right] + \frac{\partial e}{\partial t} = 0 \quad (2.1)$$

where ρ_s is density of solid particles, ρ_f is density of fluid, $k(e)$ is hydraulic conductivity as a function of void ratio (e), and z is the solids coordinate measured from a datum to a point of interest in the soil layer at time t . The z coordinate is considered positive when defined opposite to the direction of gravity.

Derivation of Eq. 2.1 is presented herein and is based on the derivation in Lee (1979) of the original governing equation proposed by Gibson et al. (1967). The relative flow rate (v) between the solid and fluid phases can be defined as

$$v = n(v_f - v_s) \quad (2.2)$$

where n is the porosity, v_f is velocity of fluid flow, v_s is velocity of solid particle movement. Considering that solid volume is conserved within a given soil element, the rate of deformation with time is equal to the rate of fluid leaving the soil element. Applying continuity to Eq. 2.2 yields

$$\frac{\partial e}{\partial t} = -\frac{\partial v_D}{\partial z} = -\frac{\partial}{\partial t} [n(v_f - v_s)] \quad (2.3)$$

where v_D is the rate of fluid flow in the system. Darcy's law can be applied to v_D as

$$\frac{\partial e}{\partial t} = -\frac{\partial}{\partial z} (k * i) = -\frac{\partial}{\partial z} \left[k * \frac{\partial h}{\partial a} \right] \quad (2.4)$$

where k is hydraulic conductivity and ∂h is the difference in pressure head between the top and bottom boundaries of a soil element. In a Lagrangian system, ∂a (Fig. 2.1b) can be expressed as shown in Eq. 2.5.

$$\partial a = (1+e) \partial z \quad (2.5)$$

The ∂h can be related to the difference in excess pore water pressure (∂u_e) and unit weight of water (γ_w) as shown in Eq. 2.6.

$$\partial h = \partial u_e / \gamma_w \quad (2.6)$$

Substituting Eq. 2.5 and Eq. 2.6 into Eq. 2.4, the continuity equation can be expressed as shown in Eq. 2.7.

$$\frac{\partial e}{\partial t} = -\frac{\partial}{\partial z} \left[\frac{k}{\gamma_w} \frac{1}{1+e} \frac{\partial \mu_e}{\partial z} \right] \quad (2.7)$$

The ∂u_e can be connected to changes in σ' as

$$\frac{\partial u_e}{\partial z} = \frac{\partial \sigma}{\partial z} - \frac{\partial \sigma'}{\partial z} - \frac{\partial u_h}{\partial z} \quad (2.8)$$

where u_h is hydrostatic pore water pressure. Total stress and u_h can be expressed shown in the following equations.

$$\frac{\partial \sigma}{\partial a} = -\frac{\gamma_s + \gamma_w e}{1+e} \quad (2.9)$$

$$\frac{\partial \sigma}{\partial z} = \frac{\partial \sigma}{\partial a} \frac{\partial a}{\partial z} = -(\gamma_s + \gamma_w e) \quad (2.10)$$

$$\frac{\partial u_h}{\partial z} = \frac{\partial u_h}{\partial a} \frac{\partial a}{\partial z} = -(1+e)\gamma_w \quad (2.11)$$

Substituting Eq. 2.9 and Eq. 2.10 into Eq. 2.8 yields Eq. 2.12 in terms of ∂u_e .

$$\frac{\partial u_e}{\partial z} = -(\gamma_s - \gamma_w) - \frac{\partial \sigma'}{\partial z} \quad (2.12)$$

Subsequently, substituting Eq. 2.12 into Eq. 2.7 yields the governing equation in Eq. 2.13 for large-strain consolidation:

$$\pm \left(\frac{\gamma_s}{\gamma_w} - 1 \right) \frac{d}{de} \left[\frac{k(e)}{1+e} \right] \frac{\partial e}{\partial z} + \frac{\partial}{\partial z} \left[\frac{k(e)}{\gamma_w (1+e)} \frac{d\sigma'}{de} \frac{\partial e}{\partial z} \right] + \frac{\partial e}{\partial t} = 0 \quad (2.13)$$

Eq. 2.13 is identical to the governing equation shown in Eq. 2.1. Although changes in compressibility ($d\sigma'/de$) and k are accounted for in Eq. 2.13, constitutive relationships for $e = f(\sigma')$ and $k = f(e)$ are required for computing large-strain consolidation.

2.3.3 Constitutive Relationships

Constitutive relationships for large-strain consolidation include compressibility ($e-\sigma'$) and hydraulic conductivity ($k-e$). These constitutive relationships are commonly expressed by the following power functions (Somogyi 1980; Liu et al. 1991; Gjerapic et al. 2008):

$$e = A \cdot \sigma'^B \quad (2.14)$$

$$e = A \cdot (\sigma' + Z)^B \quad (2.15)$$

$$k = C \cdot e^D \quad (2.16)$$

where A , B , C , D , and Z are constitutive parameters that can be determined experimentally through a SICT (Znidarcic et al. 1992). The parameters A and B are dimensionless, whereas Z has units of stress. Eq. 2.15 is an extended form of Eq. 2.14 and is commonly used to express the $e-\sigma'$ relationship since a e at zero effective stress (e_0) can be defined. This zero effective stress void ratio ($e_0 = A \cdot Z^B$) represents the e of the slurry at top of the consolidating layer (Huerta et al. 1988).

2.4 Principle of Seepage Force

A schematic of consolidation via seepage is shown in Fig. 2.3, which is based on the concept of using seepage to consolidate slurry-like materials proposed by Imai (1979). A slurry is subjected to downward water flow induced by two constant heads at the upper and lower boundaries (Fig. 2.3a). The seepage forces acts downward on all particles in the soil to induced consolidation. When the system reaches steady state, there is a constant flow rate and hydraulic gradient across the specimen.

A schematic of a soil element within the slurry specimen at steady-state is shown in Fig. 2.3b. The relationship between the elevation z and $z+dz$ is defined as

$$d\sigma = \gamma_t dz \quad (2.17)$$

where $d\sigma$ is change in total stress, γ_t is unit weight of the soil, and dz is the height increment. According to the principle of effective stress, the change in effective stress ($d\sigma'$) is

$$d\sigma' = \gamma_t dz - du \quad (2.18)$$

where du is the change in pore water pressure. Hence, the change in total head can be computed as in Eq. 2.19,

$$dh = \frac{(du - \gamma_w dz)}{\gamma_w} \quad (2.19)$$

Substituting Eq. 2.18 in Eq. 2.19 yields Eq. 2.20,

$$\frac{d\sigma'}{dz} = -\gamma_w \frac{dh}{dz} + \gamma' \quad (2.20)$$

where γ' is the buoyant unit weight of the soil. In soil mechanics, seepage force is typically expressed as force per unit volume of soil as

$$j = -\gamma_w \frac{dh}{dz} = \gamma_w i \quad (2.21)$$

where i is hydraulic gradient ($-dh/dz$). Therefore, Eq. 2.21 may be written as

$$\frac{d\sigma'}{dz} = j + \gamma' \quad (2.22)$$

which implies that the change in σ' with depth is caused by seepage force and buoyant unit weight of soil specimen.

The seepage-induced consolidation analysis is used to numerically solve the compressibility ($e-\sigma'$, Eq. 2.15) and permeability ($k-e$, Eq. 2.16) constitutive relationships based on experimental data from a SICT. When the system reaches steady-state, pore water pressure and sample height remain constant, which means that the deformation rate ($\partial e/\partial t$) in the

governing equation (Eq. 1) equals zero. The principle of σ' and integral form of large-strain consolidation can be combined to yield an integral to solve for σ' at a depth in the soil specimen. The principle of effective stress is defined as

$$\sigma' = \sigma_T - u_h - u_e \quad (2.23)$$

where u_h is hydrostatic pore water pressure. Rewriting Eq. 2.23 in integral form yields Eq. 2.24.

$$\int_0^z \frac{\partial \sigma'}{\partial a} dz = \int_0^z \frac{\partial \sigma_T}{\partial a} dz - \int_0^z \frac{\partial \mu_e}{\partial a} dz - \int_0^z \frac{\partial \mu_h}{\partial a} dz \quad (2.24)$$

The terms in Eq. 2.24 can be expressed in Lagrangian coordinates as

$$\frac{\partial \sigma_T}{\partial a} = \frac{e \gamma_w}{1 + e_0} \quad (2.25)$$

$$\frac{\partial u_s}{\partial a} = \frac{1 + e_0}{1 + e} \gamma_w \quad (2.26)$$

$$\frac{\partial u_e}{\partial a} = \frac{V_D \gamma_w}{K} \frac{1 + e}{1 + e_0} \quad (2.27)$$

Substituting Eq. 2.25 through Eq. 2.27 in Eq. 2.24 yields Eq. 2.28,

$$\sigma'(z) = \sigma'_0 + \int_0^z (\gamma_s - \gamma_w) dz + \int_0^z \frac{V_D \gamma_w}{K} (1 + e) dz \quad (2.28)$$

This formulation is another form of the governing equation (i.e., Eq. 2.1) for large-strain consolidation at steady-state. The first two terms on the right hand side represent the applied surface load and self-weight of soil solids and the final term represent the seepage force.

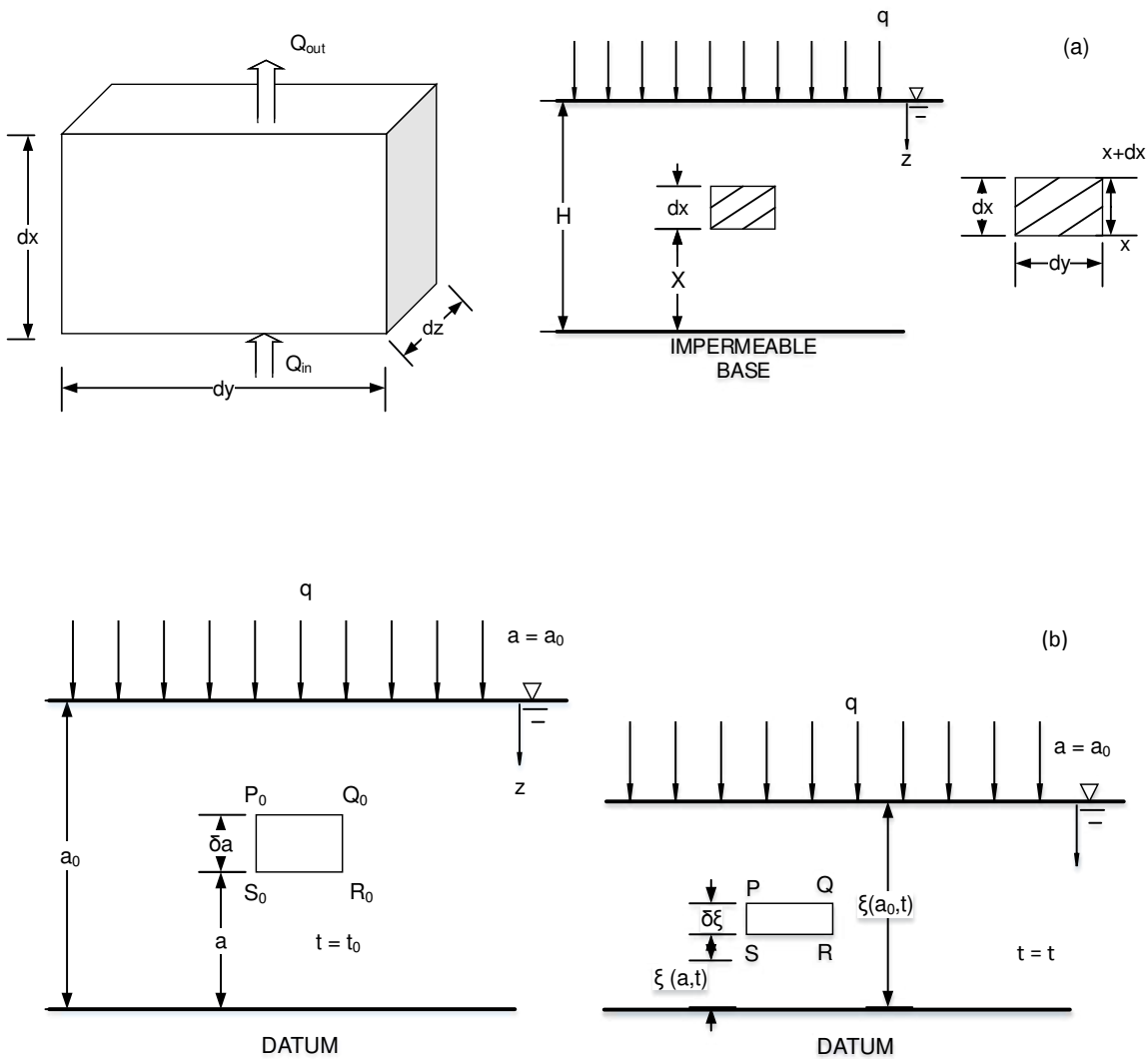


Fig. 2.1. Schematic of coordinate system for (a) Eulerian coordinate system, definitions: x = Eulerian coordinate distance of fixed element from datum plane, (b) Lagrangian coordinate system, definitions: t_0 = initial state Lagrangian coordinate, and $\xi(a, t)$ = convective coordinate as function of a and time t , δa = thickness of $P_0Q_0R_0S_0$ element, and $\delta \xi$ = thickness of $PQRS$ element.

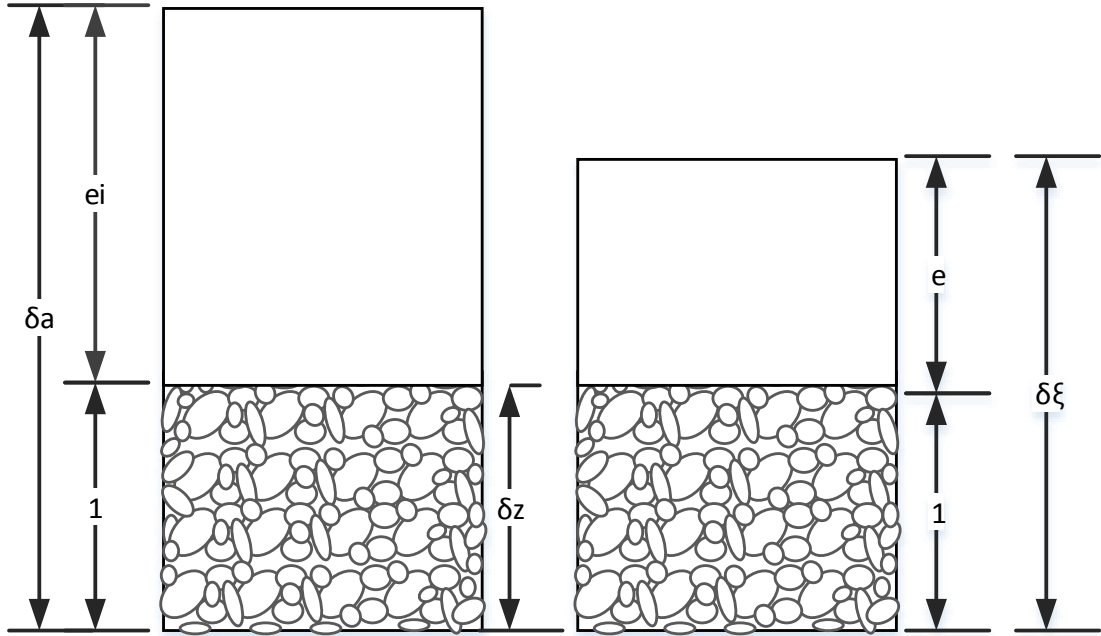


Fig. 2.2. Phase relation of soil element. Definitions: z = solids coordinate, e_i = initial void ratio.

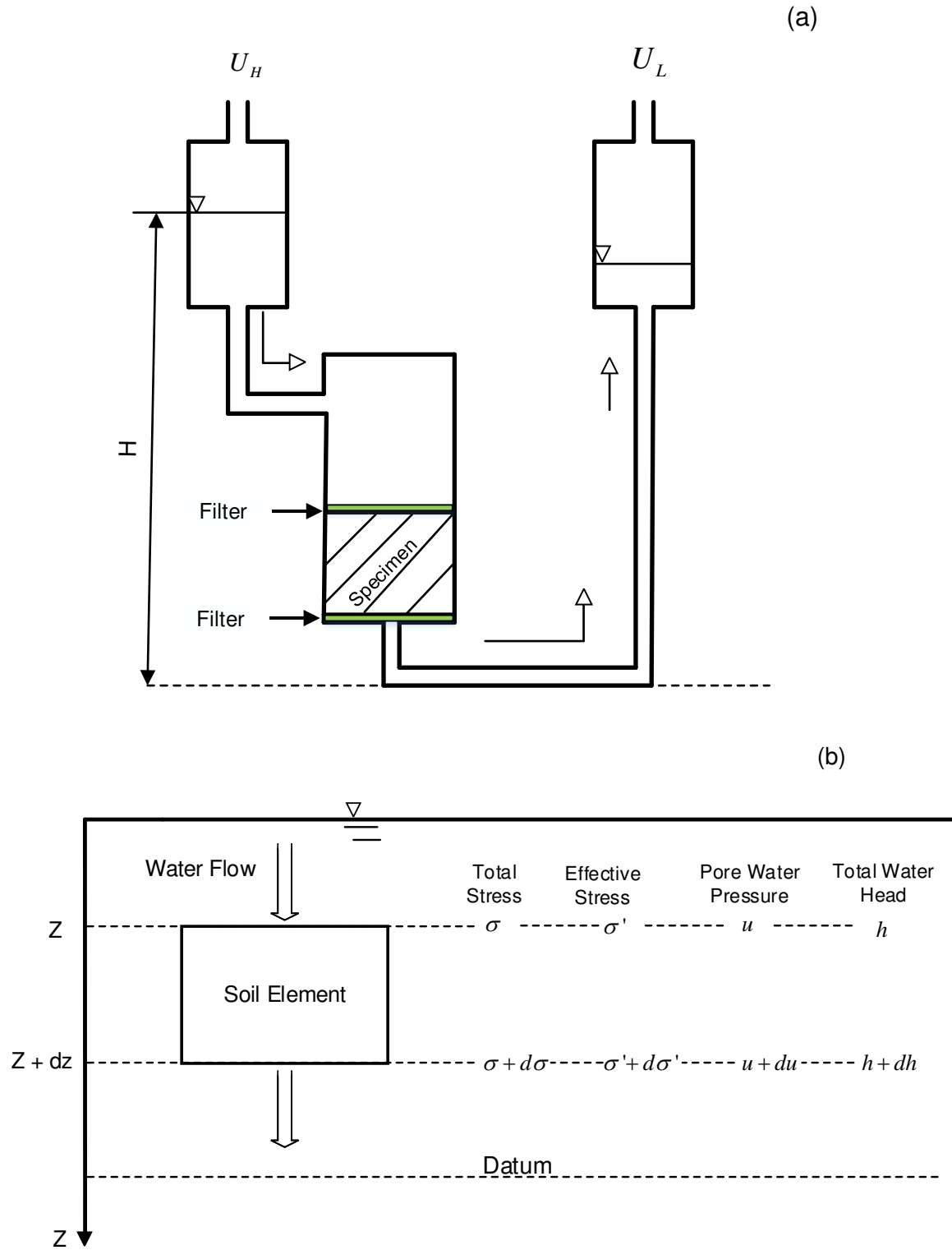


Fig. 2.3. Prepared slurry consolidates (a) under a downward water flow caused by a constant head difference and (b) stress state of soil element due to seepage force.

CHAPTER 3: SEEPAGE-INDUCED CONSOLIDATION APPARATUS

A photograph of the constructed SICT apparatus at CSU is shown in Fig. 3.1 and a schematic of the SICT apparatus is shown in Fig. 3.2. The main components of the SICT apparatus include the (i) load frame, (ii) specimen cell, (iii) load platen, (iv) seepage control, and (v) data acquisition and control system.

3.1 Equipment Overview

3.1.1 Loading Frame

The load frame consists of threaded rods, a top metal plate with an air bellofram, and bottom metal plate (Figs. 3.1 and 3.2). The threaded rods serve as a stable platform for the top metal plate and to dissipate the reaction force generated from the air bellofram that is applied to the SICT specimen. The top and bottom metal plates were machined from 25-mm-thick low carbon steel.

3.1.2 Specimen Pedestal and Casing

Design drawings for the specimen pedestal are shown in Fig. 3.3. The specimen pedestal was machined from polyvinyl chloride (PVC) and serves the following functions: (i) provide a platform for the bottom porous disk, filter paper, and specimen; and (ii) provide a water tight seal to the specimen casing. A small groove was cut horizontally in the middle section of the pedestal and two vertical through-holes pass through the pedestal to connect to the flow pump and pressure transducers. O-ring grooves were machined around the circumference and base of the pedestal to provide a water-tight connection with the specimen casing. A vertical threaded hole was made in the bottom, middle, of the pedestal to secure the pedestal to the base plate of the specimen cell (Fig. 3.2).

The specimen casing was machined from an acrylic tube (Figs. 3.1 and 3.2) that had an inside diameter of 152.4 mm, which corresponds to a specimen cross-sectional area of 0.0182 m². A larger diameter test specimen was included in the SICT design relative to other equipment (e.g., Znidarcic et al. 1992). The larger specimen reduced the Darcy velocity for a given flow rate, which should correspond to reduced specimen disturbance and less influence from side wall friction.

3.1.3 Load Platen

Design drawings of the load platen are shown in Fig. 3.4. The load platen was fabricated from a single piece of Teflon[®] and served to provide a uniform low-stress surcharge on top of the specimen. The load platen was machined in a step-pattern of concentric, stacked disks of different diameter to enhance rigidity while minimizing mass. Vertical holes passed through each step to the base of the platen to allow water flow into the specimen. Filter paper and a porous plastic disk were placed between the specimen and load platen (Fig. 3.2). The load platen weighted 1325.5 g, which corresponded to a stress of 0.35 kPa on the surface of specimen when the platen was completely submerged in water. The bottom disk of the load platen (i.e., largest diameter disk) included two small sections without drainage holes where two linear potentiometers (LP) were positioned in contact with the load platen (Fig. 3.5).

3.1.4 Linear Potentiometers

The LPs used to measure vertical deformation of the specimen surface during the SICT were positioned above the top plastic plate and to the sides of the load cell (Fig. 3.1). Extension rods were machined from aluminum and passed through linear bearings on the top plastic plate to be in contact with the load platen. The linear bearings assisted in maintaining a vertical position of the extension rods throughout a given experiment. The extension rods were 6.35 mm diameter by 304.8 mm long, and combined with the spring-return LPs, added a 0.23 kPa stress

to the top load platen. Thus, the total seating stress (σ) on a given slurry specimen was 0.58 kPa due to the load platen, LP extensions, and internal LP springs. Two LPs were used to provide redundant measurements of vertical deformation and also to avoid eccentric loading of the test specimen. The LPs were not attached to the central load piston because the piston is not used during the initial seepage phases of the experiment (described subsequently).

3.1.5 Seepage Control

Seepage was controlled in the SICT via a flow pump and Mariotte bottle (Fig. 3.2). The flow pump was used to pull fluid out of the bottom of the test specimen at a constant rate. This constant volumetric flow rate creates a vertical downward seepage condition within the specimen. The rate of seepage can be correlated to an effective stress and an increase in the rate of seepage (i.e., increase in the flow pump rate) corresponds to an increase in effective stress. The Mariotte bottle was used as a reservoir for fluid supplied to the top surface of the specimen. A Mariotte bottle was selected in lieu of a simple tank reservoir to maintain a constant head on the top surface of the specimen.

The flow pump used in the SICT apparatus as CSU was KDS Legato 200 Series Syringe Pump (KDS Scientific, Holliston, MA) that can accommodate different syringe sizes (0.5 μ L to 140 mL) that correspond to a broad range of flow rates (3.06 pL/min to 216 mL/min). The flow pump interfaces with a valve control box to provide four different operations modes: (i) infuse only, (ii) withdraw only, (iii) infuse/withdraw, and (iv) withdraw/infuse. The flow pump was used with two 50-mL plastic syringes, such that a 30-mL volume of each syringe defined the functional volume for the flow pump. This setup achieved flow rates as low as 0.001 mL/min. Low flow rates are preferable in a SICT since high flow rates have the potential to develop negative water pressure at the bottom of a specimen that can lead to cavitation.

The Mariotte bottle was fabricated from acrylic plastic tube and a small plastic tube with an outside diameter of 7 mm and inside diameter of 3.5 mm was inserted through the top of the

bottle to control the pressure head (Fig. 3.2). The pressure at the bottom of the small air inlet tube is always equal to atmospheric pressure. If the water level in the specimen casing is equal to the height of bottom of air inlet, water will not flow into the specimen casing from the Mariotte bottle since the total heads are equal. During the seepage phase, water elevation in sample casing will decrease because water is pumped out by the flow pump. The total head in the sample casing is smaller than the total head in Mariotte bottle and water is delivered under a constant head to the inflow side of the specimen, regardless of the water level change in the Mariotte bottle.

3.1.6 Data Acquisition and Measurement

The data acquisition (DAQ) and control system consisted a National Instrument (NI) USB-6215 DAQ board connected to a PC and controlled via LabVIEW and MICAS-X 2.1.2 software (Original Code Consulting, Boulder, CO). Measurements were recorded from the two LPs, two in-line pressure transducers, and load cell (during the loading stage; described subsequently) every second and post-processed via a moving-window average technique in Microsoft Excel (Microsoft®, Redmond, WA). All sensors were powered via an external power supply (CSI3003X III, Circuit Specialists®, Tempe, AZ). The digital flow pump was not computer-controlled and the flow rate was recorded manually from the flow pump.

In-line pressure transducers were used to measure pressure at the top and bottom boundaries of a specimen. These in-line pressure transducers had a capacity of 103.4 kPa and measurement accuracy of ± 0.2 kPa (PX309-015G5V, OMEGA®, Stamford, CT).

Vertical force applied to a specimen during the loading phase of a SICT was generated via a frictionless air bellofram (S-24-F-SM-900056000, Marsh Bellofram®, Newell, WV). Air pressure supplied to the air cylinder was computer-controlled via an air regulator (S-Type 1001-966-490-000, MARSH BELLOFRAM®, Newell, WV) to adjust the air pressure based on the target normal force. The load cell was used to measure vertical force and used as feed-back

control for the air regulator. Detailed information on each transducer and calibration curves are in Appendix B.

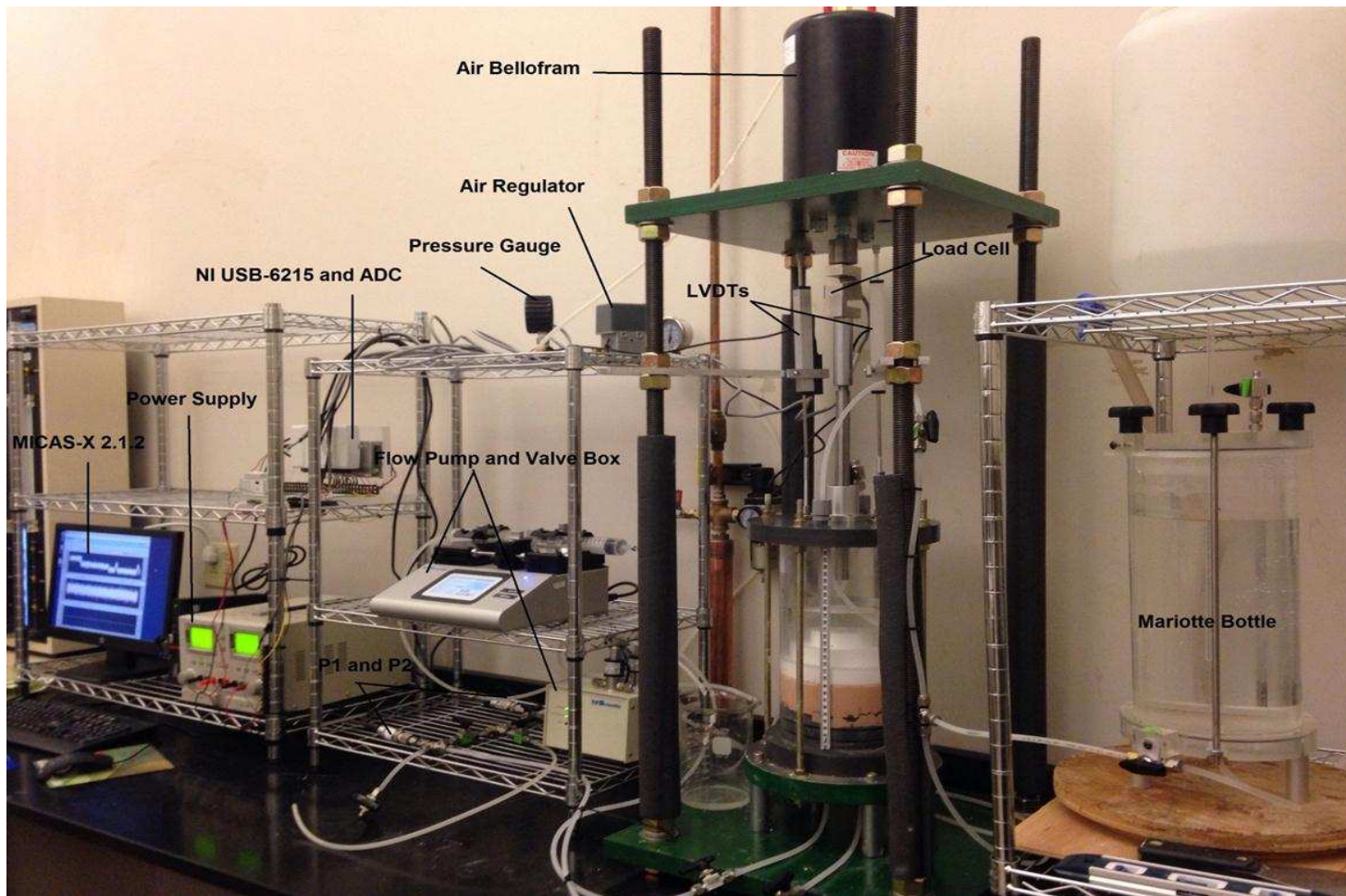


Fig. 3.1. Photograph of the seepage-induced consolidation apparatus

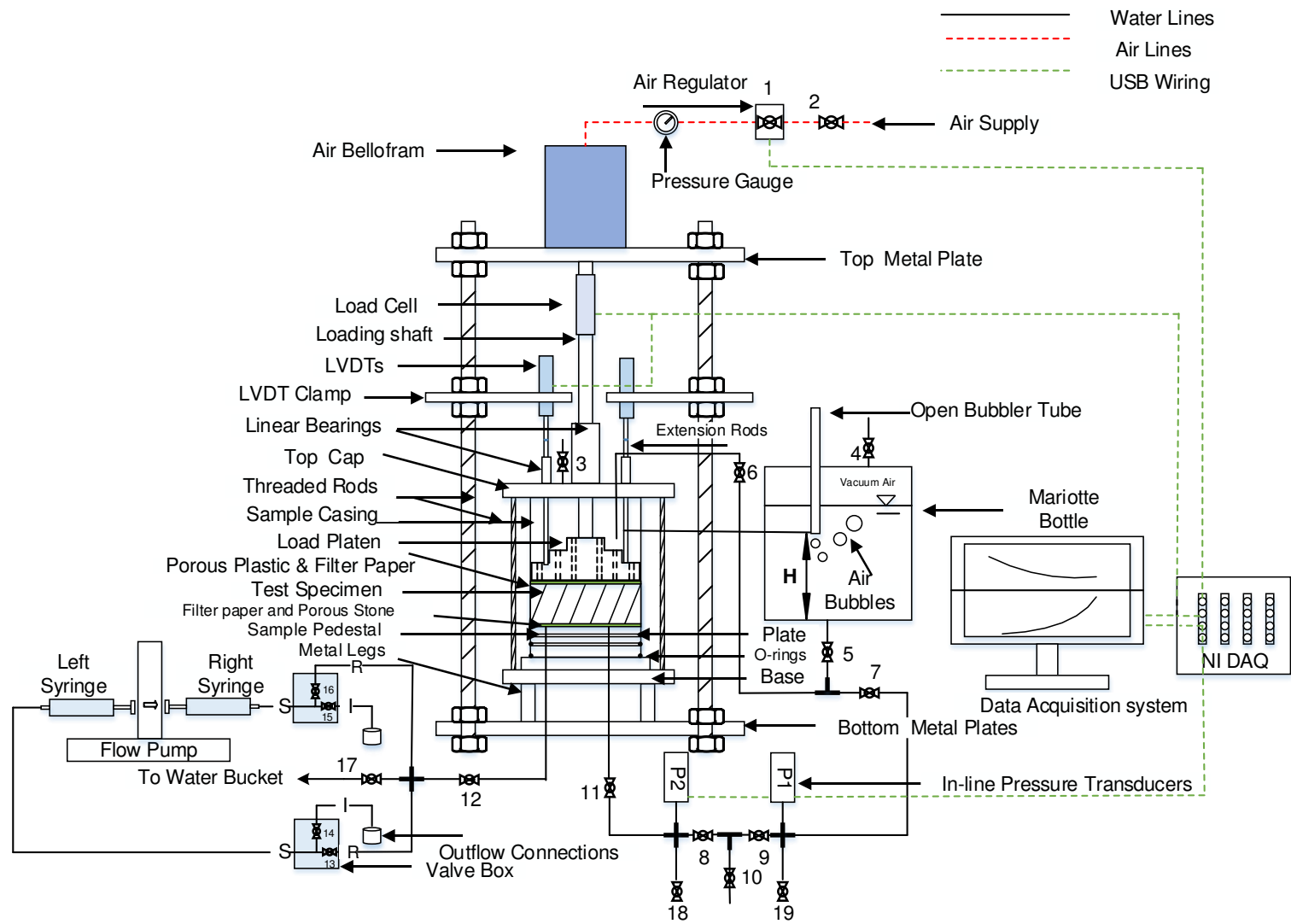


Fig. 3.2. Schematic of the seepage-induced consolidation apparatus

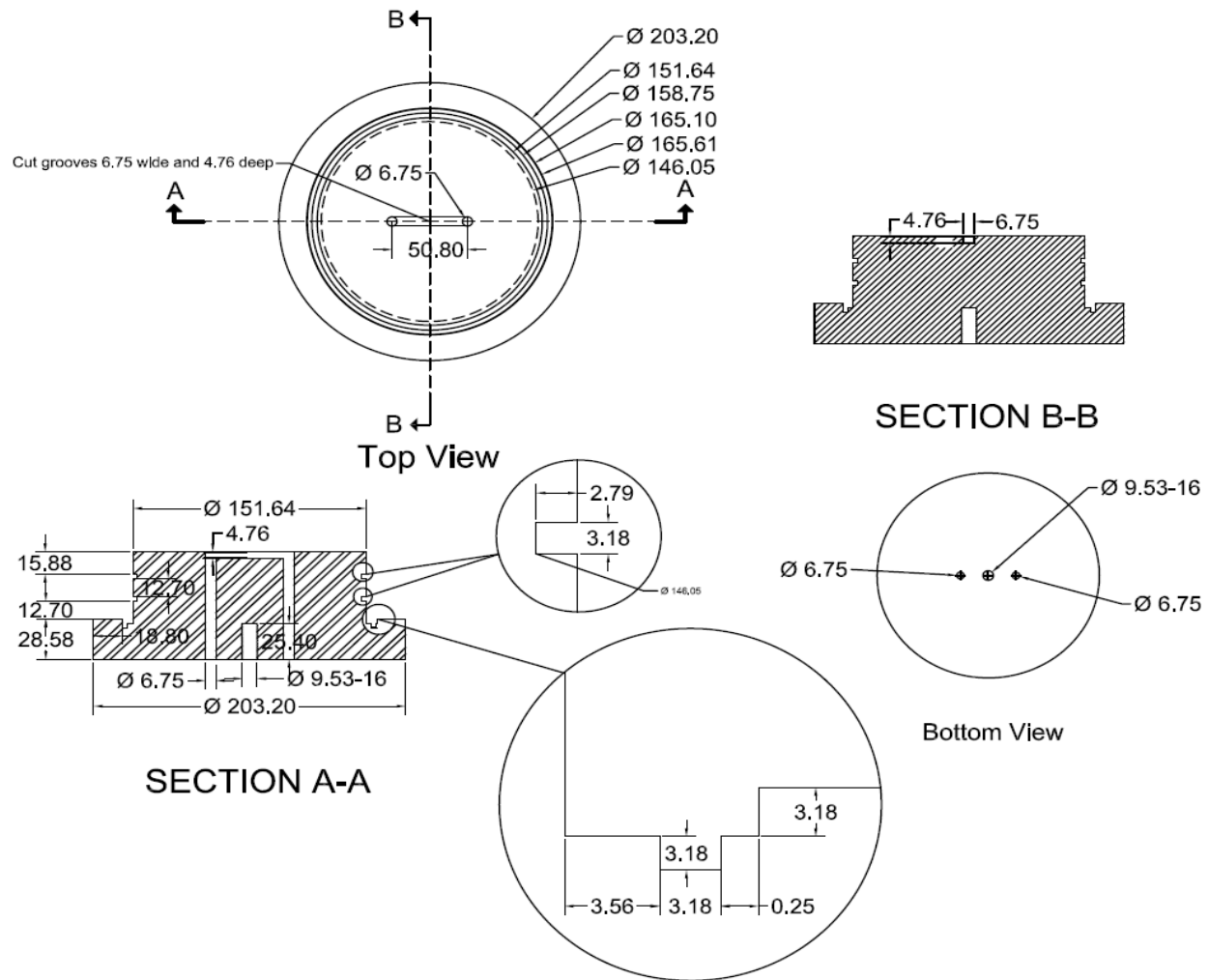


Fig. 3.3. Cross-section and plan view schematics of the specimen pedestal (dimensions in mm)

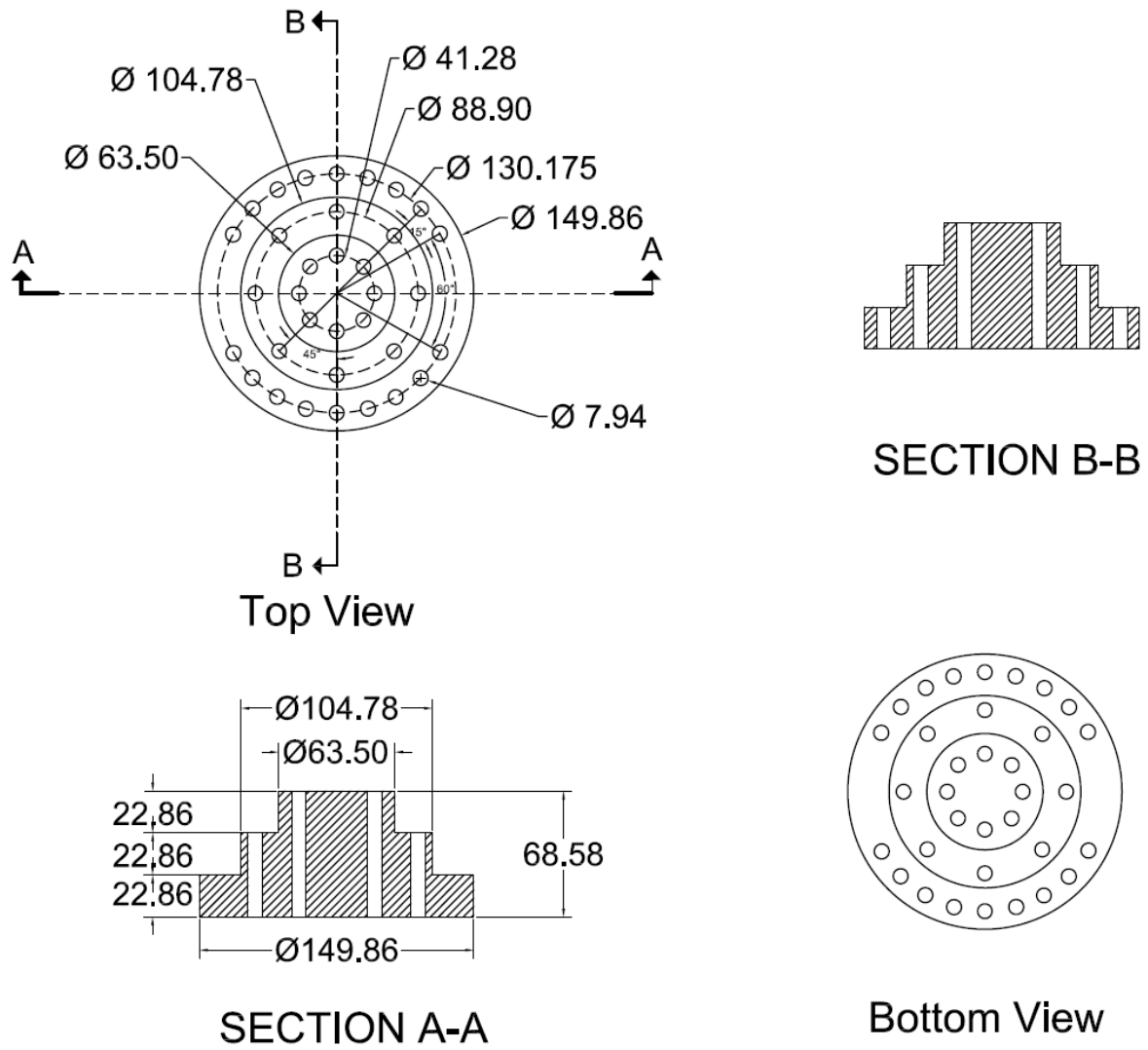


Fig. 3.4. Cross-section and plan view schematics of the load platen (dimensions in mm)

CHAPTER 4: MATERIALS AND METHOD

Three materials were used in this study: (i) kaolin clay, (ii) fine synthetic tailings (FST), and (iii) average synthetic tailings (AST). Kaolin clay was obtained from Thiele Kaolin Company (Georgia, USA) and used to evaluate reliability of the SICT apparatus and compare results with similar experiments conducted by others (e.g., Estepho 2014). Synthetic tailings were created from commercially-available soils to capture typical characteristics of hard-rock mine tailings (Alhomair et al., 2016; Hamade, 2016; Gorakhki and Bareither, 2017). Consolidation tests were performed via SICT and traditional odometer on all three materials to (i) compare measured consolidation behavior and (ii) assess the influence of slurry composition on consolidation behavior.

4.1 Materials

Physical characteristics and the classification of the synthetic tailings and kaolin clay are in Table 4.1. Particle size distribution (PSD) curves of the AST and FST are shown in Fig. 4.1 along with an average, upper-bound, and lower-bound PSD curve determined from a compilation of actual hard-rock mine tailings (Alhomair et al. 2016). The FST was prepared to represent the upper-bound of PSD (i.e., finer grained) and AST were used to represent the average PSD. Fine synthetic tailings was prepared as 60% silica flour (US silica, USA) and 40% kaolin clay, and classified as low-plasticity clay (CL) according to Unified Soil Classification System (USCS) (ASTM D2487). Average synthetic tailings was prepared as 20% road-base sand with a maximum particle diameter of 2 mm and 80% silica flour. The AST was predominantly silt-size particles ($0.005 \text{ mm} < \text{particle diameter} < 0.075 \text{ mm}$) and classified as low-plasticity silt (ML) according to the USCS.

4.2 Methods

4.2.1 Sedimentation Test

Sedimentation tests were conducted on all three tailings to determine the solids content (SC) at which the slurried materials transitioned to a soil. Initially, particles start to build a soil skeleton due to the gravity of solids particles and then effective stress builds up due to material self-weight and the slurry materials start to behave as a soil (Bonin et al., 2014). The SC for each material was used to prepare slurried materials for consolidation tests. Sedimentation tests were conducted in 1-L glass cylinders that had an inside diameter of 63.5 mm and height of 457 mm. Each sedimentation test included 50 g of dry soil that was mixed (described below) with Fort Collins, CO, tap water and subsequently allowed to settle freely out of suspension.

Dry soil was added to a dispersion cup with 250 ml of tap water and mixed at a speed \geq 10,000 rpm for 1 min. The slurry was then poured into a 1-L glass cylinder and additional tap water was added to achieve a total volume of 1 L. Sedimentation cylinders were covered with a rubber stopper and agitated vigorously for 1 min and then placed on a laboratory table until all particles settled out of suspension and a clearly-defined interface formed between the supernatant liquid and settled material.

The final height of the settled material was measured to compute total volume (V_t) of the soil. Supernatant water was removed and the all solids were removed and oven-dried to determine the mass of dry soil (M_s). The volume of solids (V_s) was computed using the soil specific gravity (G_s) and then the volume (V_w) and mass of water (M_w) were computed assuming complete saturation. Solids content was then computed as the ratio of M_s to total mass ($M_t = M_s + M_w$). The SC for kaolin for kaolin was 36%, the SC for FST was 50%, and the SC for AST was 73%. As expected, the SC decreased with increase in clay content (Table 4.1).

4.2.2 Slurry Preparation

Slurries composed of kaolin clay, AST, and FST were prepared to the target SCs determined from the sedimentation tests. All slurries were prepared by mixing air-dried soil with tap water in a 305-mm diameter by 254-mm tall bucket. Materials were blended manually with stainless steel spatula, allowed 24 hr for hydration, and then blended again immediately prior to testing.

4.2.3 Oedometer Test

A photograph of an oedometer test assembly and schematic of an oedometer cell used in this study are shown in Fig. 4.2. A porous stone and filter paper were placed at the bottom of a consolidation cell and a filter paper and porous Teflon[®] load platen were placed on top of the specimen (Fig. 4.2b). The Teflon[®] load platens were used in lieu of conventional porous stones and steel load platens to minimize the initial load applied to the slurry specimens. These Teflon[®] load platens ranged from 41 to 42 g, which resulted in a vertical stress of approximately 0.1 kPa. Pressure transducers were connected to valves at the bottom of the oedometer to monitor excess pore pressure during loading. Spring-return LPs were used to measure vertical deformation of the specimen (ART.NR. 023263, Novotechnik). The springs of the LPs generated a small vertical stress (~ 0.8 kPa) on the slurry specimens; this spring force was accounted for when monitoring initial deformation.

An initial loading sequence of an oedometer specimen involved placing the Teflon[®] load platen on top of the specimen, positioning the loading bar and loading shaft, and positioning the potentiometer (Fig. 4.2). The Teflon[®] load platen was placed on top of the specimen and then the loading shaft of the oedometer was positioned in contact with the load platen (Fig. 4.2a). The loading bar of the oedometer was locked in place via a threaded rod below the moment arm to avoid additional loading of a specimen. The potentiometer was positioned above the load and data collection was initiated. The threaded rod securing the moment arm was lowered and

loading from the potentiometer and load shaft was transferred to the specimen. The initial loading corresponded to a σ'_0 of approximately 0.9 kPa. Each odometer frame was calibrated such that vertical seating load due to the Teflon[®] platens, potentiometers, and load shafts were known. Vertical deformation of the specimen during setup of each odometer test was assumed negligible such that all vertical deformation was recorded via the LPs. All odometer tests were conducted with a load increment ratio 1.0 (ASTM D2435). Vertical loads were applied every 24 hr to a maximum vertical stress of 100 kPa. Measurements of vertical deformation and excess pore pressure were recorded via a data logger connected to a PC.

The square root of time method (Taylor 1948, ASTM D2435) was used to estimate hydraulic conductivity at the end of primary consolidation in each oedometer test. The advantage of square root of time method is that consolidation does not have to pass 100% to determine time-rate characteristics (Coduto et al. 2014). The following equations were used to calculate hydraulic conductivity at the end of primary consolidation:

$$k_f = \frac{a_v \cdot \gamma_w \cdot c_v}{1 + e_f} \quad (4.1)$$

$$a_v = \frac{\Delta e}{\Delta \sigma'} \quad (4.2)$$

$$c_v = \frac{0.848 \cdot H_f^2}{t_{90}} \quad (4.3)$$

where k_f = hydraulic conductivity at the end of primary consolidation, e_f = void ratio at the end of primary consolidation, a_v = coefficient of compressibility, c_v = coefficient of consolidation, H_f = thickness, and t_{90} = elapsed time at 90% primary consolidation (Coduto et al. 2014). The t_{90} , H_f , and a_v were determined from deformation measurements for each vertical load increment to estimate k_f at each stress level.

4.2.4 Seepage-Induced Consolidation Test

The SICT apparatus was described in detail in Chapter 3. A step-by-step procedure of the SICT is provided in Appendix A. A brief summary of the testing sequence for each SICT specimen follows.

Prior to all testing, all air present in water lines should be removed. Place porous stone and filter paper on top of sample pedestal, and then place sample casing on the sample pedestal. The homogeneous test specimen is poured into then sample casing through a funnel with an inflow diameter of 190 mm and outflow diameter of 10 mm. The height of funnel was 190 mm and the drop height of slurry was approximate 64 mm. The height of the final slurry specimen should be between 38 mm to 51 mm (Znidarcic et al. 1994). The prepared slurry specimen should have a horizontal surface or the central portion of the specimen surface should be slightly higher than the perimeter to prevent the loading plate from wedging in the sample casing (Znidarcic et al. 1994). To attain a horizontal surface, the sample casing may be gently agitated side-to-side. The specimen initial height should be recorded and then filter paper is placed on top of testing specimen. A hand held syringe should be used to add water on top of filter paper to minimize disturbance to the slurry sample. A saturated porous plastic disc with an outside diameter of 150 mm and thickness of 3 mm is placed on top of filter paper to evenly distribute liquid across the surface of the specimen during the SICT. The load platen is then placed atop the porous plastic disc and extension rods and spring-LPs are installed on top of load platen.

To initiate the SICT, open valve 12 (valve numbers are labeled in Figure 3.2) and turn on flow pump at a flow rate 0.14 ml/min (Estepho 2014). The first seepage phase is run until steady state conditions are achieved. Steady state is defined as no change in the differential pressure across the specimen for at least one hour. After steady state conditions are achieved, a higher flow rate is selected for a subsequent seepage test. Seepage testing steps can be stopped

when the resulting pressure difference across the specimen is between 2 kPa and 5 kPa (Abu-Hejleh and Znidarcic et al., 1996).

During the step loading test, valve 17 is closed and valve 2 is open to provide air pressure for the air Belloram to provide normal load. A minimum vertical stress 10 kPa is applied to the top load platen. When a step load is applied, water pressure at the lower specimen boundary increases due to the load. Steady state is also defined for the step load phase as when no additional specimen vertical deformations are observed for 1 hr. A constant rate of flow permeability test is conducted to measure the hydraulic conductivity of the specimen. Valve 17 is opened a permeability test is performed using flow pump at one tenth of the flow rate used for the seepage phase (Abu-Hejleh and Znidarcic et al., 1992 and Estepho, 2014). A LIR of 1.0 is selected for step loading if additional specimen compression is necessary (these tests provide redundant step-load data; discussed subsequently).

During the SICT, sample height is recorded when the system achieves the steady state to calculate the void ratio. After testing the specimen is extracted and oven dried to determine the total solids mass for calculation of final void ratio and solids content. Final void ratio and solids content are used as redundant data to compare the final void ratio and solids content calculated known input solids content and final height of testing specimen.

4.2.5 Calculation of Compressibility and Permeability for a SICT

A flow diagram for the analysis approach applied to each SICT is shown in Fig. 4.4. A SICT analysis has been described in Znidarcic (1994), and Abu-Hejleh and Znidarcic (1996), and was adapted for this study. The SICT analysis is designed to yield the compressibility ($e-\sigma'$) and hydraulic conductivity ($k-e$) constitutive relationships and requires data from a sedimentation test and one step loading phase of a SICT to assess consolidation behavior during the seepage phase.

The constitutive relationships for $e-\sigma'$ and $k-e$ in Eqns. 2.15 and 2.16 were solved as shown in Eqns. 4.4 through 4.6 to yield functions for A , Z , and C as a function of empirical parameters B and D .

$$A = \frac{e_0}{Z^B} \quad (4.4)$$

$$Z = \frac{\sigma'_f}{\left(\frac{e_f}{e_0}\right)^{1/B} - 1} \quad (4.5)$$

$$C = \frac{k_f}{(e_f)^D} \quad (4.6)$$

Eq. 4.4 was obtained assuming that σ' in Eq. 2.15 was equal to zero to correspond to the zero effective stress void ratio (e_0). The e_0 measured in a sedimentation test was adopted herein to represent the density state of the slurry for $\sigma' = 0$. Eq. 4.5 was obtained via assuming the A parameter is constant and setting Eq. 4.4 equal to Eq. 2.15 solved for A as a function of the final stress and void ratio (σ'_f , e_f) conditions at the end of the step loading phase in the SICT. The σ'_f and e_f at the end of the loading phase are assuming uniform across this thickness of the specimen such that these can be computed from imposed stress conditions and weight-volume relationships. Finally, Eq. 4.6 was obtained via solving Eq. 2.16 directly for C and relating conditions imposed on the SICT specimen at the end of the loading phase. At the end of the loading phase the flow pump was used to impose a steady-state seepage condition such that k could be computed directly from Darcy's law. This k coincides with the e_f of the slurry (i.e., k_f) and was assumed constant across the specimen at this stage.

The SICT analysis requires iteration to search for the optimal values of B and D in Eqns. 4.4 through 4.6 to find the $e-\sigma'$ and $k-e$ constitutive relationships that provide a solution to the steady-state conditions of a seepage phase in the SICT. This procedure was completed analytically in Microsoft Excel using Solver to optimize the B and D parameters. The thickness

of the specimen was divided into N layers (Fig. 4.3) in Excel such that the thickness of each layer was less than 1 mm to assume a given layer had constant e , σ' , and k . The first iteration was to determine e and k at the end of consolidation due to self-weight of the slurry and the load platen. Subsequently, iterations were applied to the steady-state seepage phase, whereby σ' was calculated by Eq. 2.28, e was calculated by Eq. 2.15, and k was calculated by Eq. 2.16 for each layer of the specimen.

The iterative process included B and D as optimized variables to directly solve for A , C , and Z (Eqns. 4.4-4.6). Constraints were imposed on B (-5 to -0.05) and D (0.1 to 8) as recommended by Znidaricic (1992). The iterative procedure was continued until the normalized difference in void ratio met a user-defined error threshold. The error (ε) in the iterative calculation was computed as

$$\sum_{i=1}^{i=N} \frac{e_i^{j+1} - e_i^j}{e_i^j} < \varepsilon \quad (4.7)$$

where e_i^j is the computed void ratio for layer i and iteration j , and e_i^{j+1} is the void ratio for layer i and iteration $j+1$. Based on the total normalized difference provided by Abu-Hejleh and Znidaricic et al. (1992), a $\varepsilon \leq 10^{-4}$ was used as the convergence criterion for all SICTs in this study.

Table 4.1 Physical characteristics and classification of kaolin clay and synthetic tailings

Material	<i>LL</i> (%)	<i>PI</i> (%)	<i>USCS</i>	d_{max} (mm)	Sand Content (%)	Fines Content (%)	Clay Content (%)	G_s
Fine Synthetic	37	15	CL	0.05	0.0	100.0	42	2.63
Average Synthetic	NA	NA	ML-CL	2.0	14.2	85.8	13	2.66
Kaolin Clay	76	42	CH	0.002	0.0	100.0	100	2.60

Note: *LL* = liquid limit; *PI* = plasticity index (ASTM D4318); *USCS* = Unified Soil Classification System (ASTM D2487); d_{max} = maximum particle size (ASTM D422); G_s = specific gravity (ASTM D854); NA = not applicable. Synthetic tailings data are from Alhomair et al. (2016).

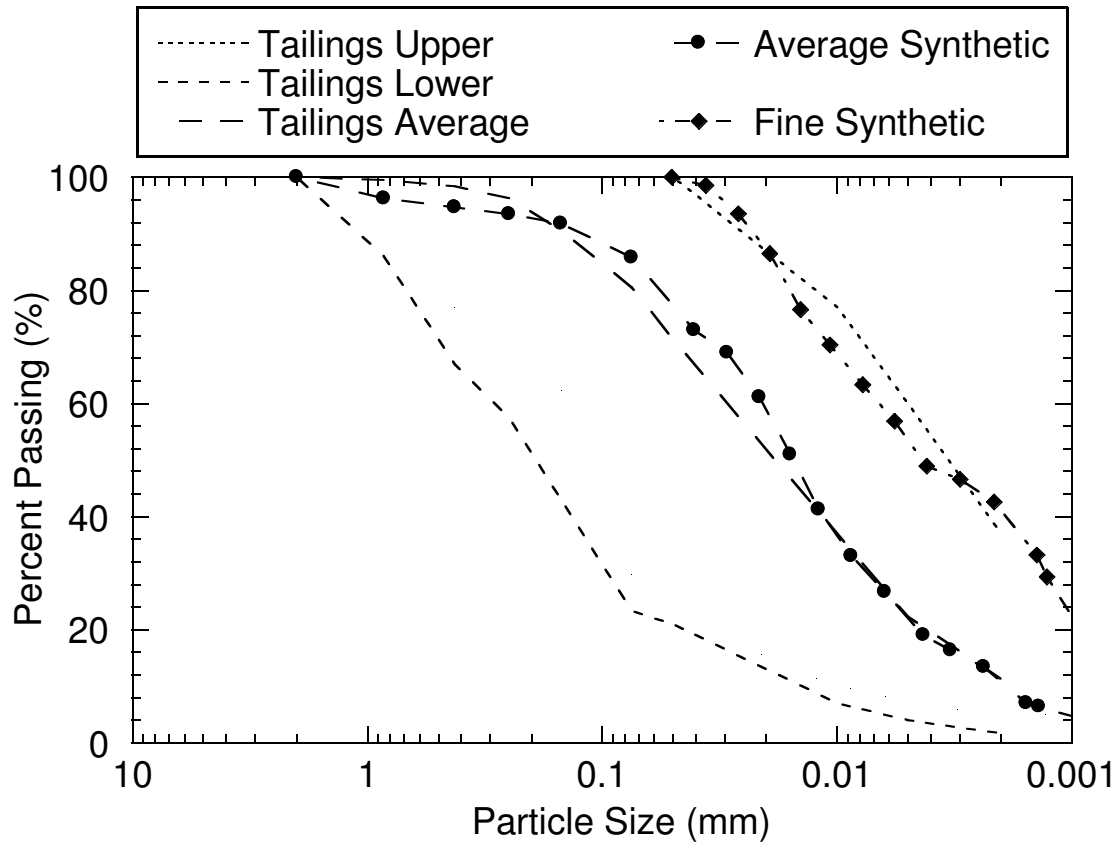


Fig. 4.1. Particle-size distribution for fine synthetic tailings, average synthetic tailings, and the upper-bound, lower-bound, and average from compiled mine tailings particle-size distribution (Alhomair et al., 2016).

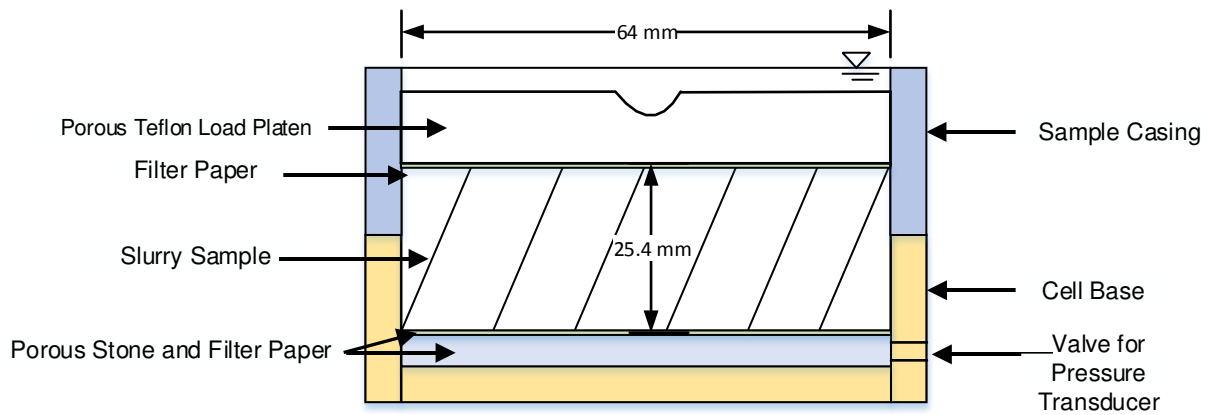
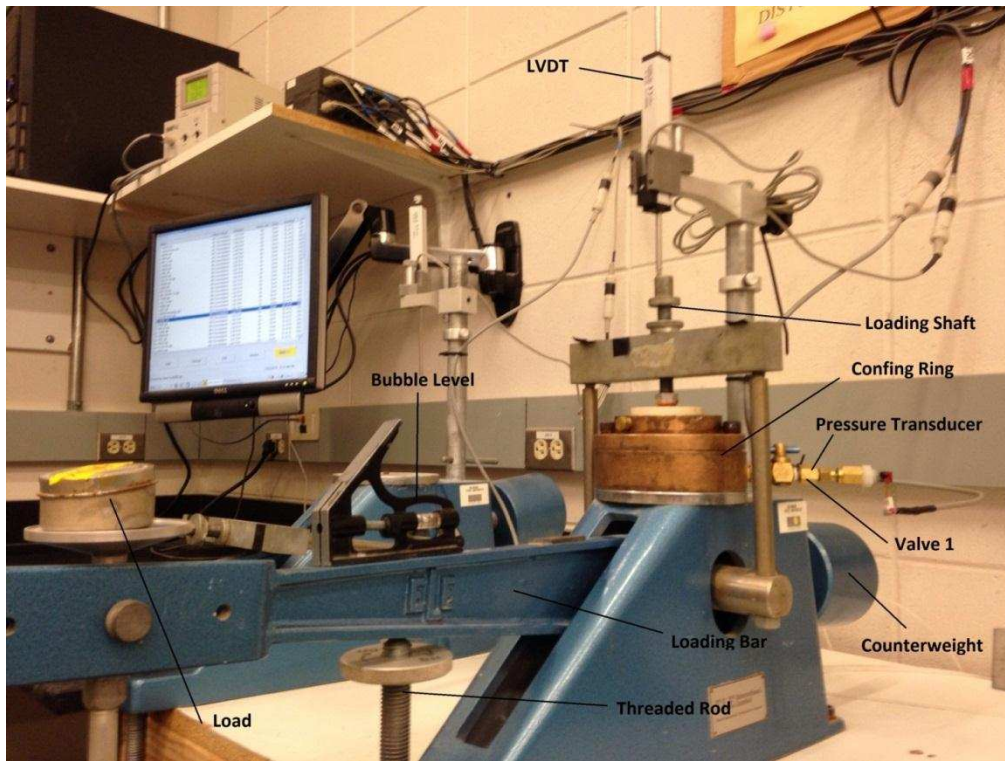


Fig. 4.2. (a)Overall diagram of odometer at CSU, and (b) cross section view of confining ring

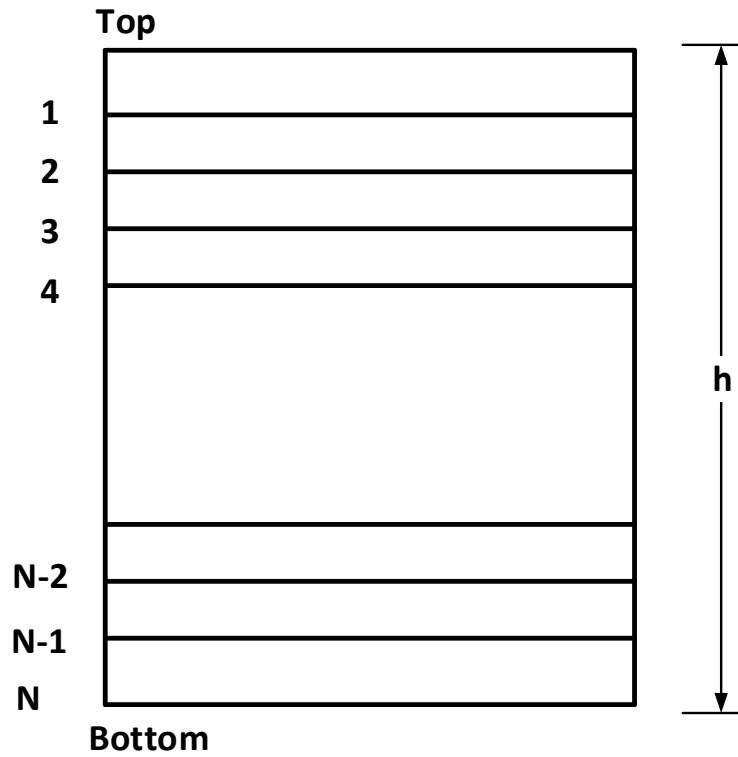


Fig.4.3. Soil profile of testing specimen. Soil column is divided into N layers when slurry sample is poured into sample casing and each layer has same thickness.

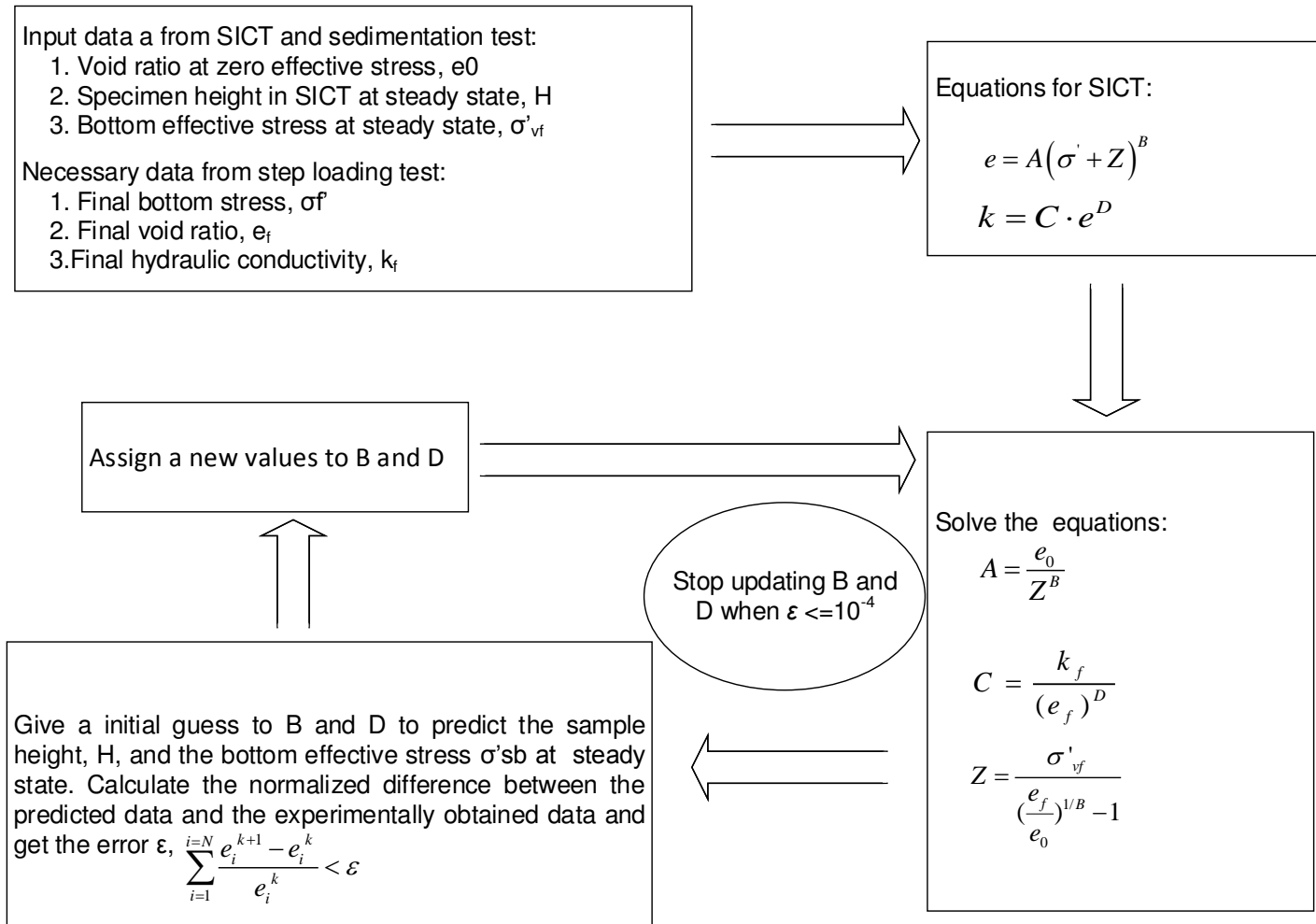


Fig. 4.4. Flow Chart of SICT Analysis

CHAPTER 5: RESULTS AND DISCUSSION

A summary of the SICTs and odometer tests conducted for this study is in Table 5.1. These experiments were conducted to achieve the following objectives: (i) verify that the SICT and odometer test yield comparable consolidation behavior and constitutive relationships ($e-\sigma'$, $e-k$); (ii) assess repeatability of the SICT; and (iii) evaluate the effect of slurry composition on consolidation behavior. Data compiled in Table 5.1 include the following: SC of the slurry specimens after applying the seating load; initial void ratio of the slurry specimens (e_i); e_0 at zero effective stress based on a sedimentation test; initial height of the slurry specimen (H_i); initial height of unconsolidated sample (H_0), and initial height of soil solids (H_s). The SC s for the odometer specimens were slightly higher than the SICT specimens due to a higher σ'_0 (≈ 0.8 kPa in oedometer tests and ≈ 0.58 kPa in SICTs). Initial void ratio and void ratio σ'_0 were determined before the test (a detailed procedure for this determination is provided in Appendix C). Initial height and e_0 are used to calculate the height of solids in sample based on soil phase relationships. Void ratio at zero effective stress is used as input data for Eq. (4.4).

5.1 Consolidation Behavior in the SICT and Odometer

5.1.1 Seepage-Induced Consolidation

Temporal relationships of differential pressure (ΔP) between pore pressure on the top (u_t) and bottom (u_b) surfaces of a SICT specimen ($\Delta P = u_b - u_t$) and settlement for Kaolin-1 are shown in Fig. 5.1. Each SICT included three phases that induced consolidation: (i) self-weight of the slurry and placement of the load platen; (ii) seepage; and (iii) loading. These three phases are identified in Fig. 5.1 along with stages of successive seepage (i.e., Seepage 1, 2, and 3) and loading (i.e., Loading 1, 2, 3, and 4) that increased σ' . A summary of the flow, stress, and deformation characteristics for each stage of the SICT on Kaolin-1 is in Table 5.2.

The data compilation in Table 5.2 includes the following: average hydraulic gradient (i_{ave}); vertical effective stress at the bottom of the specimen induced by initial placement of the load platen (σ'_0), stress from the air bellofram (σ'_a), stress from seepage (σ'_s), and the final condition effective at steady-state (σ'_f); flow rate induced by the flow pump (Q); specimen thickness at steady-state (H_f); hydraulic conductivity for final steady-state conditions at the top (k_{ft}), middle (k_{fm}), and bottom (k_{fb}) of the specimen; and void ratio for final steady-state conditions at the top (e_{ft}), middle (e_{fm}), and bottom (e_{fb}) of the specimen. Similar data in the form of temporal ΔP and settlement plots and tabulated test parameters are included for all SICTs conducted for this study and are discussed subsequently.

Consolidation settlement was initially allowed to occur for one day following placement of the load platen and LPs on the SICT specimen. The e and k of the specimen were considered uniform throughout the specimen at the end of this initial phase (Table 5.2) such that e was computed from weight-volume relationships and k was estimated via Eq. (2.16) after best constitutive parameters are updated by Solver. The three seepage stages followed the initial loading phase with the duration dependent on the time to reach steady-state conditions. Flow rates were increased for the three seepage stages (0.14, 0.4, and 0.8 mL/min) to continuously induce higher σ' within the test specimen at a load increment ratio (LIR) of approximately 1.0 at the bottom of the specimen (Table 5.2).

The temporal relationships of ΔP for Kaolin-1 (Fig. 5.1a) show localized changes in ΔP during a given seepage stage. These localized changes in ΔP correspond to points in time when the flow pump reached capacity of the syringes (i.e., 30 mL for each of two 50-mL syringes) and reversed direction to maintain the target flow rate. Thus, application of a given seepage rate via the flow pump required the pump to continuously fill and discharge water from each syringe. The magnitude of ΔP decreased during flow to approach a constant value, which is characteristic of a pressure difference and induced hydraulic gradient across a test specimen.

The ΔP increased towards 0 when the flow pump paused and reversed direction, which allowed pressure at the bottom of the specimen to slowly increase due to the ponded water on top of the specimen. Following the change in direction of the flow pump, a short elapsed time was needed to re-establish steady-state conditions. The change in direction of the flow pump and change in ΔP did not affect settlement, and a relatively smooth settlement curve was measured for each seepage stage (Fig. 5.1b).

Vertical loads were applied to a given SICT specimen after σ'_f ranged between 5 to 10 kPa (Abu-Hejleh and Znidarcic 1994). The magnitude of σ'_a was selected to maintain LIR ≈ 1 (Table 5.2). Flow through the specimen was not induced via the flow pump during initial application of a given σ'_a , which created a no-flow boundary at the bottom of the specimen. Thus, a positive u_e developed at the bottom of the specimen due to σ'_a that corresponded to a positive ΔP across the specimen. Steady-state during a loading stage was defined by $\Delta P \approx 0$ kPa, and a permeability test was conducted once steady-state conditions were achieved to measure k_f (Table 5.2). A flow rate of approximately 0.5 mL/min was induced across the test specimen at the end of a given loading stage and k_f was computed once ΔP remained constant for at least one hour. Although only a single loading stage is required to determine the e - σ' and e - k constitutive relationships, four loading stages were applied to each SICT specimen to generate redundant data and assess the uniqueness of the constitutive relationships computed for different combinations of seepage and loading stages.

Vertical deformation of a SICT specimen was recorded via two LPs and the average of two LP measurements is shown in Fig. 5.1b. The difference between the two LPs never exceeded 3 mm in any of the experiments conducted for this study. Thus, the average settlement is shown for each SICT and all void ratios were computed based on the average settlement. Furthermore, a single e and k are reported for a SICT during each loading stage (Table 5.2). A pronounced magnitude of vertical deformation always occurred for the first

loading stage (i.e., Loading 1) due to the variation in e throughout a given specimen during seepage. This vertical deformation was assumed to reduce any variation in e throughout a test specimen such that a single e and k were representative after step loading.

The variation in e_f and k_f as a function of normalized depth throughout the SICT specimen Kaolin-1 at steady-state for induced loading from the load platen and each seepage stage are shown in Fig. 5.2. These distributions were obtained following the algorithm technique in Excel along with data from the sedimentation test and Loading 1. The Top, Middle, and Bottom points identified in Fig. 2 correspond to the e_f and k_f values compiled in Table 5.2. Each SICT was divided into $N = 40$ layers in Excel for the iterative algorithm technique, and the first layer corresponded to e_{tf} and k_{tf} , the average of the 20th and 21st layers corresponded to e_{mf} and k_{mf} , and the 40th layer corresponded to e_{bf} and k_{bf} .

Prior to seepage, e_f and k_f were approximately constant with depth. Application of vertical downward flow included a variation in σ' across the specimen, which created denser conditions (i.e., lower e) with depth and lower k that were reflective of these lower e . Additionally, the variation in e_f and k_f throughout the specimen increased with an increase in seepage flow rate (i.e., from Seepage 1 to Seepage 2 to Seepage 3), which was due to a larger variation in σ' across the specimen.

Relationships of e versus σ' and e versus k for Kaolin-1 are shown in Fig. 5.3. Data in Fig. 5.3 include e_f , σ'_f , and k_f points for the top, middle, and bottom of the specimen for each seepage stage as well as single points representative of the middle of the specimen during each of the loading stages. The data compiled in Fig. 5.3 identify the shape of the e - σ' and e - k constitutive relationships. The e - σ' and e - k constitutive relationships (Eqs. 2.15 and 2.16) can be determined for each combination of seepage and loading stages (12 combinations total) as well as fit through all data shown in Fig. 5.3 to create composite constitutive relationships.

Development and assessment of these potential constitutive relations is discussed subsequently.

5.1.2 Oedometer Testing

Temporal relationships of u_e measured at the bottom of the specimen and settlement for kaolin clay measured in an oedometer cell are shown in Fig. 5.4. A summary of loading steps in the oedometer test on kaolin is in Table 5.3. The initial SC of the kaolin clay in the oedometer was slightly higher (44%) compared to the SICT specimen (35%), which facilitated forming the specimen and avoided squeezing-out material during loading. An $LIR \approx 1.0$ was used for all step loads in the oedometer test, and c_v and a_v were computed for each load (Eqs. 4.2 and 4.3) to calculate an estimate of k_f (Eq. 4.1).

Consolidation of kaolin clay measured in the oedometer cell exhibited typical behavior for consolidation of a fine-grained soil. A rapid accumulation of settlement coincided with each step load, which was followed by a reduced rate of settlement characterized by secondary compression (Fig. 5.4b). The u_e measured at the bottom of the specimen spiked with each load increase (Fig. 5.4a); however, the magnitude of u_e was only a fraction of the actual applied load. Yilmaz et al. (2010) reported u_e between 0% and 96% of the applied vertical stress (σ'_a) for 203-mm-thick specimens due to drainage valve(s) remaining open. The top drainage boundary for oedometer tests conducted for this study was always a free-drainage boundary such that u_e could begin dissipating immediately following load application, and thus, u_e was less than σ'_a for all applied loads for kaolin.

5.1.3 Consolidation Comparison

Relationships of compressibility ($e-\sigma'$) and hydraulic conductivity ($e-k$) for kaolin clay measured in the SICT (Kaolin-1) and odometer test are shown in Fig. 5.5. Similar trends of decreasing e with increasing σ' and decreasing k with decreasing e are observed in data generated from both experiments. The trends in $e-\sigma'$ from the SICT and oedometer overlap for $\sigma' > 7$ kPa (Fig. 5.5a), which suggest that the relationship of $e-\sigma'$ for kaolin clay was effectively captured in both experiments. A small difference in the $e-\sigma'$ trends exists at low σ' (< 5 kPa), which was attributed to (i) differences in SC between the two specimens and (ii) minor over-consolidation of the oedometer specimen incurred when placing (with a spatula) the paste-consistency material in the odometer ring.

Hydraulic conductivities calculated from odometer test data were underestimated relative to k measured in the SICT (Fig. 5.5b). The measured k in the SICT are believed to be more accurate since Darcy's law was applied directly to monitoring data and the flow and boundary conditions were known. In contrast, k computed from oedometer test data were based on small-strain consolidation theory (i.e., Eqs. 4.1 – 4.3). Regardless of the differences in k between the SICT and oedometer test, the $e-k$ trends were similar and k was always within the same order of magnitude for a given e .

5.2 Repeatability of the SICT

Temporal relationships of ΔP and settlement for the SICTs on Kaolin-2 and Kaolin-3 are shown in Figs. 5.6 and 5.7, respectively. A compilation of the three loading phases and specific seepage and applied loading stages for Kaolin-2 and Kaolin-3 are in Table 5.4 and Table 5.5, respectively. These two experiments were conducted similar to Kaolin-1 to assess repeatability of the SICT. The only difference between the three SICTs on kaolin clay was that Kaolin-3 only included two seepage stages versus the three seepage stages in the other two experiments.

The ΔP data recorded for Kaolin-2 and Kaolin-3 were similar to Kaolin-1, whereby a negative ΔP coincided with seepage and a positive ΔP coincided with the step loading phase (Figs. 5.1, 5.6, and 5.7). In addition, the accumulation of settlement was similar between all three experiments.

Relationships of settlement strain ($\epsilon_v = \Delta h/H_0$) for the entire all three phases of the SICTs on kaolin clay and normalized excess pore water pressure (u_e / σ'_a) during the loading phase are shown in Fig. 5.8 as a function of σ'_f . These normalized relationships further emphasize the similarity in consolidation behavior measured between the three SICTs and support repeatability of the equipment. The u_e measured at the bottom of the SICT specimens was at least 70% of the applied loads (Fig. 5.8a). The reduction in u_e with increasing σ' was attributed to a reduction in drainage path and corresponding shorter time needed to dissipate u_e . Similar behavior has been reported in literature (Yilmaz, 2010; Chakrabarti and Horvath, 1986).

The distributions of e and k as a function of normalized depth in the SICT specimen for Kaolin-2 and Kaolin-3 are shown in Fig. 5.9. Similar e and k distributions were observed between Kaolin-2 and Kaolin-3, as well as to distributions shown for Kaolin-1 in Fig. 5.2. The e and k distributions support an increase slurry density (decrease in e) with depth in a given SICT specimen due to the increased seepage force with specimen depth that translates to higher σ' . The reductions in e with depth in all SICT specimens consisting of kaolin clay coincide with reduced k due to smaller voids.

Relationships of compressibility ($e-\sigma'$) and hydraulic conductivity ($e-k$) for Kaolin-2 and Kaolin-3 measured in the SICT and kaolin clay in the odometer test are shown in Figs. 5.10 and 5.11, respectively. Similar consolidation behavior was observed between both SICTs (Kaolin-2 and Kaolin-3) and the oedometer test. Minor deviations between the $e-\sigma'$ trends for Kaolin-2 and Kaoline-3 and the oedometer test data were observed for $\sigma' < 5$ kPa, whereby e measured in the oedometer were smaller for a given σ' at low stress conditions. This observation was also

made for Kaolin-1 and attributed to differences in initial SC of the specimens as well as modest overconsolidation of the oedometer specimen due to physically placing the paste-like slurry into the oedometer cell.

5.3 Slurry Composition Effects on Consolidation

Temporal relationships of ΔP between the top and bottom specimen surfaces and settlement for FST and AST are shown in Fig. 5.12 and Fig. 5.13, respectively. These two seepage-induced consolidation tests were conducted on two different materials to study the effects of slurry composition on consolidation behavior. Additionally, two oedometer tests were conducted on same materials to provide extra verification of the slurry composition effects on consolidation behavior.

5.3.1 Seepage-Induced Consolidation Data

Material properties and experimental data on FST and AST are provided in Table 5.1, Table 5.5 and Table 5.6. Two seepage stages and four step loading stages were conducted on FST as shown in Fig. 6.12. Flow rates 0.14ml/min and 0.5 ml/min were selected for seepage test, and flow rates 0.05 ml/min and 0.04 ml/min were selected for permeability based on previous test conducted on kaolin clay (Table 5.5). When testing specimen achieved the steady state after first permeability test, the flow pump did not switch the direction due to the mistake made by tester (Fig. 5.12a). Fortunately, steady state had been achieved before the flow pump was stopped.

Temporal relationships of ΔP between the top and bottom specimen surfaces and settlement for AST are shown in Fig. 5.13. Preliminary testing on this material (i.e., failed SICT) resulted in significant squeezing out of material when the load platen was placed. Therefore, testing specimens were allowed to self-weight consolidate for two hours prior to placement of

the load platen. During the test, three seepage stages and four step loading stages were conducted on AST. Since 20% of sand was mixed in the materials, testing specimen achieved steady state in less than 2 hours and 2 mm deformation was obtained during the self-weight consolidation as shown in Fig. 5.13a. Flow rates 0.14 ml/min, 0.28 ml/min and 1 ml/min were selected for seepage test to maintain LIR of 1.0 (Table 5.6). Overall, nearly 50% deformation was obtained during the seepage phase. During the step loading phase, excess pore water pressure was dissipated in less than 10 mins (5.13a) due to relatively large k . However, at least 1 hour was needed to dissipate excess pore water for FST (Fig. 5.12a) due to an order of magnitude in k between AST (10^{-7} m/s) and FST (10^{-8} m/s).

Variations of e and k along the testing specimen for FST and AST are shown in Fig. 5.14 and Fig. 5.15, respectively. FST is characterized as silty clay and AST is characterized as sandy silt (Table 4.1). Because of the effects of composition, variations of e and k are different for these two materials. Before the seepage phase, the changes in e and k are insignificant for FST and AST, but the initial e of FST is greater than AST. With induce of flow rates in the specimen, the variations of e and k along the soil profile become greater for FST, however, the variations of e and k along the soil profile for AST were not significant (Fig. 5.15). As anticipated, the effects of slurry composition have a large impact on the consolidation behavior on the large strain consolidation behavior of initially slurried materials.

5.3.2 Oedometer Testing

FST was prepared in an initial void ratio of 2.1, initial height of 25.4 mm and solids content of 60% by mass. Temporal relationships of differential pressure (Δu) between the top and bottom specimen surfaces and settlement of FST and AST are shown in Fig. 5.16. The response of u_e for FST is similar in oedometer test and SICT. Both tests took at least 1 hour to dissipate u_e as shown in Fig. 5.12 and Fig. 5.16. The square root of time method was also used

to analyze the consolidation behavior of FST to compute the k and the results are listed in Table 5.8.

AST was prepared in an initial void ratio of 0.95, initial height of 25.4 mm and solids content of 75% by mass. No AST data for Δu since u_e dissipated rapidly due to the sand and silt content. Vertical load of 2.02 kPa, 4.04 kPa, 10.13 kPa, 20.26 kPa, 51.92 kPa and 107.12 kPa were used in the test during the step loading test. Additionally, the deformation for AST does not appear significant (Fig. 5.17) and similar consolidation behavior is observed in SICT as shown in Fig. 5.13b. Square root of time method was also used to analyze the consolidation behavior of AST to compute the k , and the results are listed in Table 5.9.

5.3.3 Consolidation Comparison

Compressibility and permeability relationship of FST are shown in Fig. 5.18. Results generated from odometer test and SICT are represented in open and solid symbols, respectively. Before seepage was initiated, variations of e and k were small along the soil profile as shown in Fig. 5.14. When seepage was started in the test, the change of effective stress along the soil profile increased and generating variation in e and k along the soil profile (Fig. 5.14). During the step loading phase, the test specimens were vertically loaded in a similar manner yielding overlapping e and k data (Fig.5.18).

Consolidation behavior of FST from odometer has a good match with the data generated from SICT in step loading phase. During the seepage stage, the initial e from the odometer was slightly lower than the e generated by the SICT due to the higher solids content used in odometer test. Additionally, some minor over-consolidation of the slurry specimen may have occurred due to physical placement of the slurry, paste-consistency material in the odometer ring. The relationship between e and k for the odometer test deviate slightly from the data calculated from the SICT because k calculated from odometer test are based on small-strain consolidation theory.

Consolidation behavior of AST from odometer tests matches data generated from the SICT (Fig. 5.19). Due to the small difference of initial solids content between SICT and odometer test specimens, consolidation behavior between SICT and odometer initially overlap. Additionally, although k calculated from the odometer test are based on small-strain consolidation theory, the difference between SICT and odometer test appear to be minimal, likely because small strains were observed throughout SICT on AST (Fig. 5.13b).

5.4 Constitutive Relationships

Constitutive relationships are used to simulate consolidation behavior, e.g., predict the long-term field behavior of lab tested tailings. Data from the seepage test and step loading test phases are used as input data for SICT to calculate compressibility ($\sigma'-e$) and permeability ($\sigma'-k$) curves for a material. Constitutive relationships of kaolin-1 are shown in Fig. 5.20. Three seepage test phases and four step loading test phases are used as SICT input data yielding 12 permutations that simulate the consolidation-permeability behavior of kaolin-1. Additionally, a composite model using all data from a single SICT is used to simulate the consolidation-permeability behavior of kaolin-1. The composite model is based on the same constitutive equations (Eq. 2.15 and Eq. 2.16); constitutive parameters A , B , C , D , and Z are updated by Microsoft SOLVER to minimize the SSR.

In Fig. 5.20, results generated from odometer test and SICT are represented in open symbols and solid symbols, respectively. Constitutive relationships generated from the 12 possible combinations provide similar fits with SICT data. The 12 resultant compressibility and permeability curves nearly overlap. Theoretically, one seepage test phase and one step loading test phase are the minimum data needed to model consolidation and permeability behavior of the tested material (Znidarcic et al., 1992). However, if the initial flow rate is too high, resulting in a seepage stress in excess of 5 to 10 kPa (Abu-Hejleh and Znidarcic et al., 1996), a second test may be needed to attain requisite low-stress-range.

Fig. 5.20 illustrates that the composite model provides a good fit of SICT data, similar to fit generated from the other 12 constitutive models. Additionally, consolidation behavior of kaolin-2, kaolin-3, FST, and AST are simulated by composite model and yield results similar to the observed data (Fig. 5.21 to Fig. 5.23). These results support that the composite model can be used as a tool to predict the consolidation behavior for a broad range of σ' as well as for different types of (initially) slurry materials.

5.5 Slurry Compositions and Constitutive Relationships

Constitutive relationships for kaolin-1, kaolin-2, kaolin-3, FST, and AST are shown in Fig. 5.24. Consolidation behavior ($e-\sigma'$) of tested specimens illustrate a wide range of behaviors as a result of different slurry compositions. Kaolin clay is more compressible than FST and AST because the clay component dominates the material. FST has 80% of silt and 20% of clay (Table 5.1) and the recompression index (C_r) and compression index (C_c) are smaller than kaolin clay (Fig. 5.24a). AST contains 20% of sand and 80% of silt and the consolidation behavior is dominated by the sand fraction. AST exhibits minimal deformation and C_r and C_c are small compared to kaolin clay and FST. The relationship between e and k further substantiates that the constitutive relationship is a function of slurry composition. AST has the largest k and the change of k over the σ' tested is minimal due to the small change in e throughout the test. The magnitude of changes in e and k for kaolin clay are larger than for FST (Fig. 5.24b).

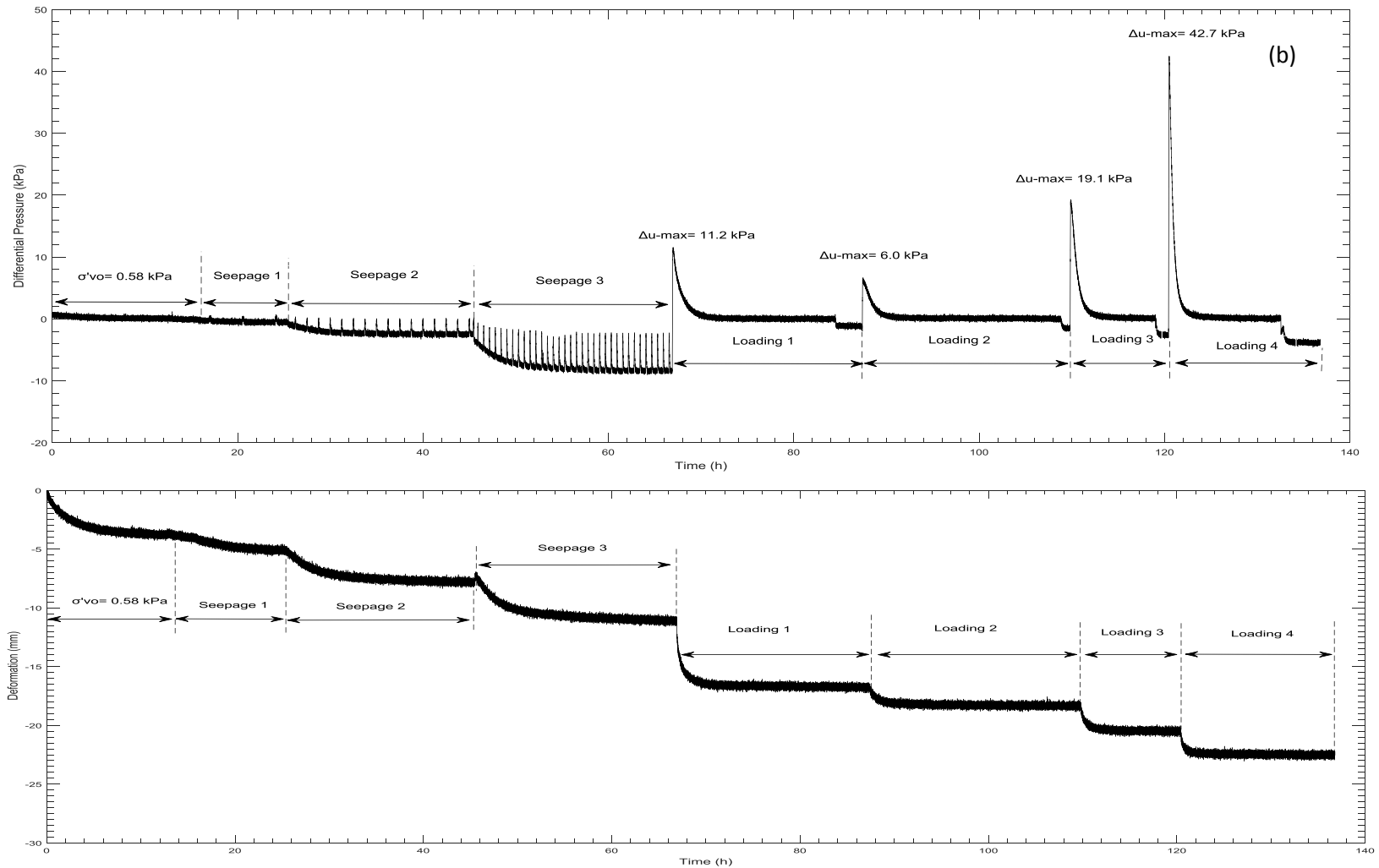


Fig. 5.1. Experimental data of kaolin-1 during SICT: (a) differential pressure across the testing specimen versus time, Δu -max is the maximum excess pore water pressure generated at the bottom of testing specimen (b) deformation versus time; σ'_0 is the sum of self-weight of slurry sample and surcharge load caused by load platen, two extension rods and two LPs. Note: flow rate and applied load for each seepage are provided in Table 5.2.

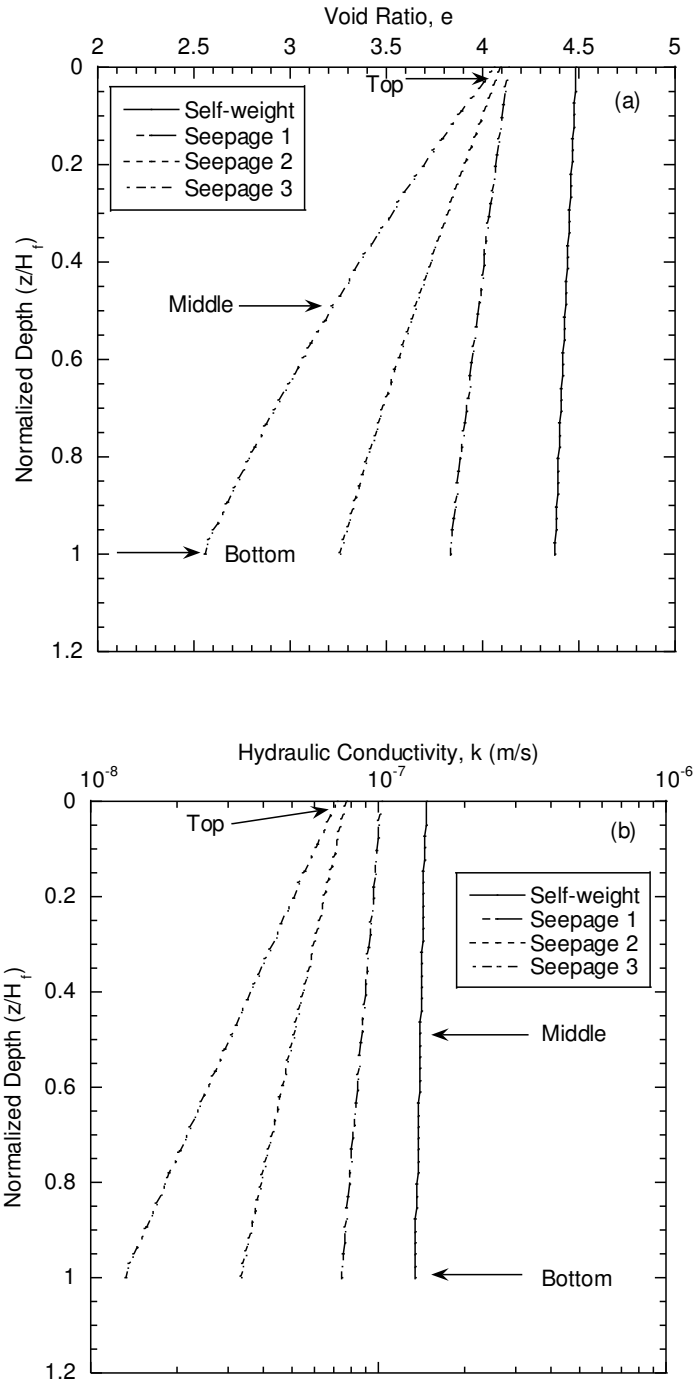


Fig. 5.2. Distributions of (a) void ratio, and (b) hydraulic conductivity for kaolin-1 during self-weight and seepage induced consolidation processes at steady state

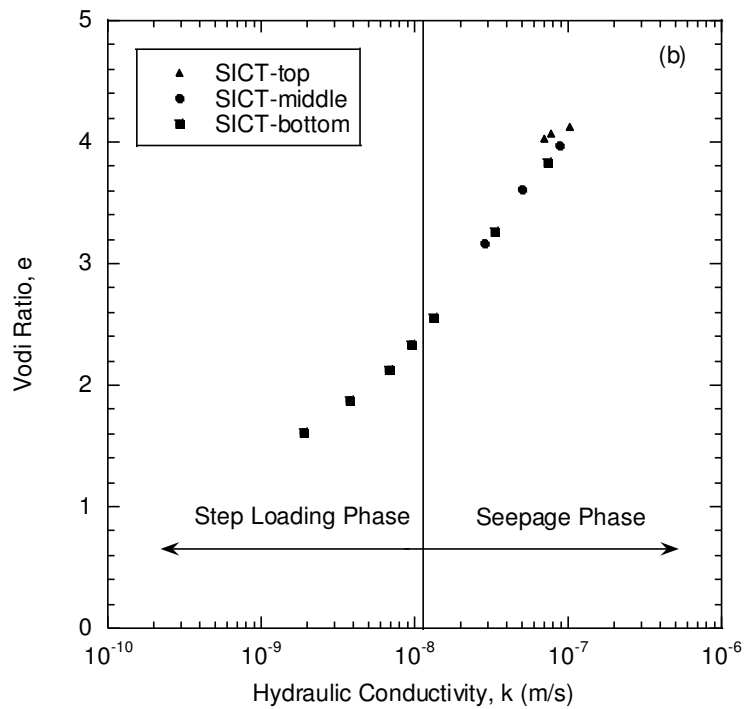
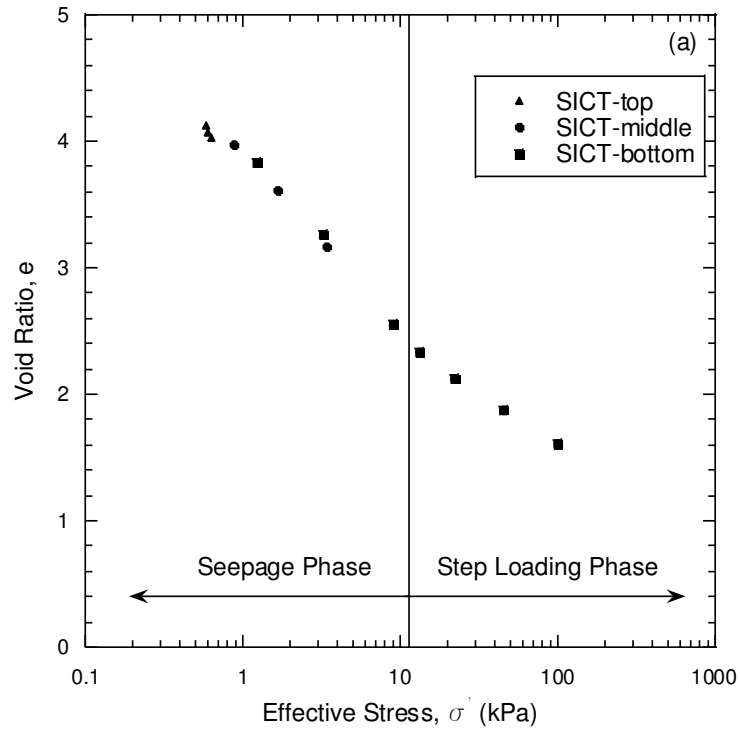


Fig. 5.3. Constitutive relationships of kaolin-1 (a) effective stress-void ratio relationship (b) hydraulic conductivity-void ratio relationship.

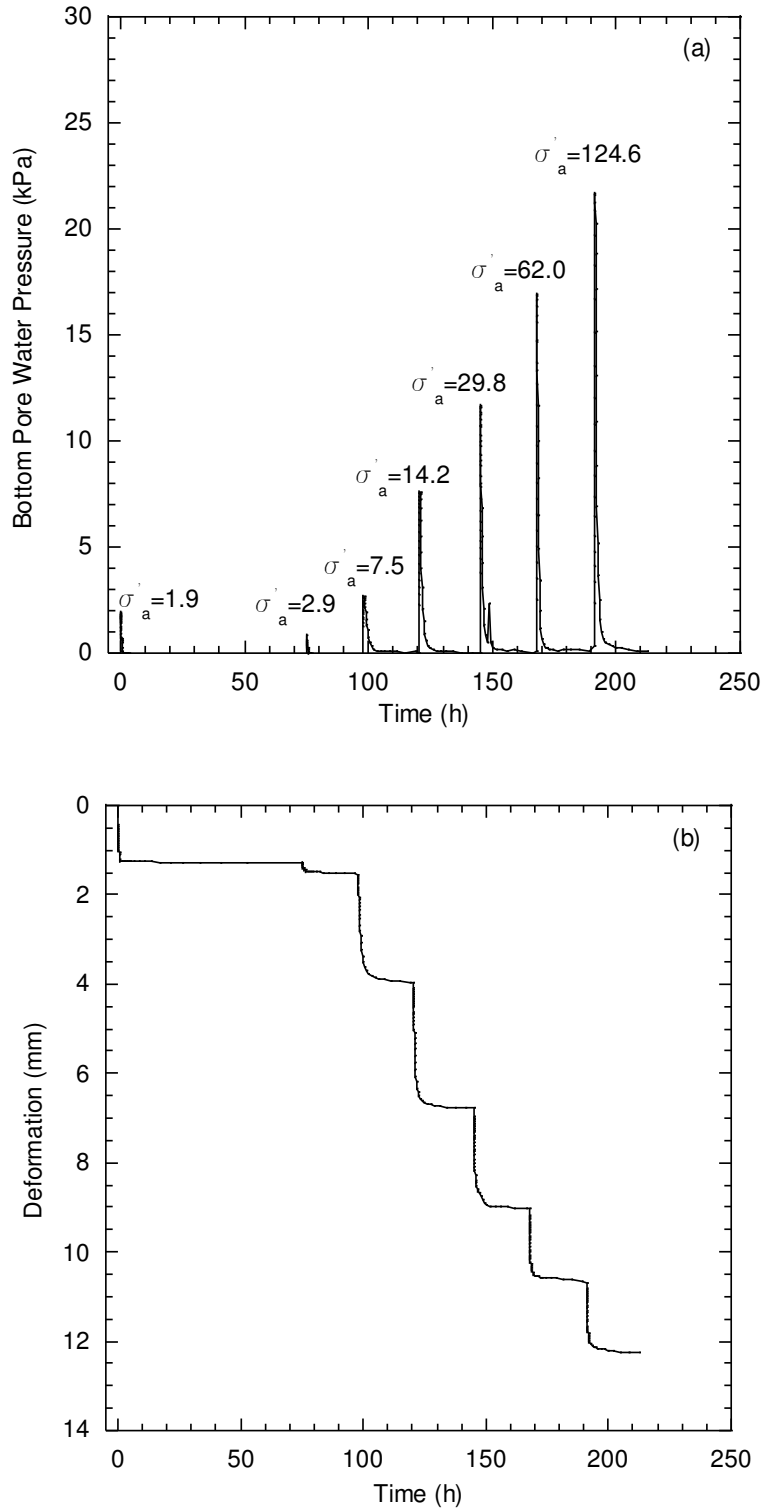


Fig. 5.4. Experimental data of kaolin-1 during odometer test: (a) bottom pressure versus time (b) deformation versus time; σ'_a is the applied load.

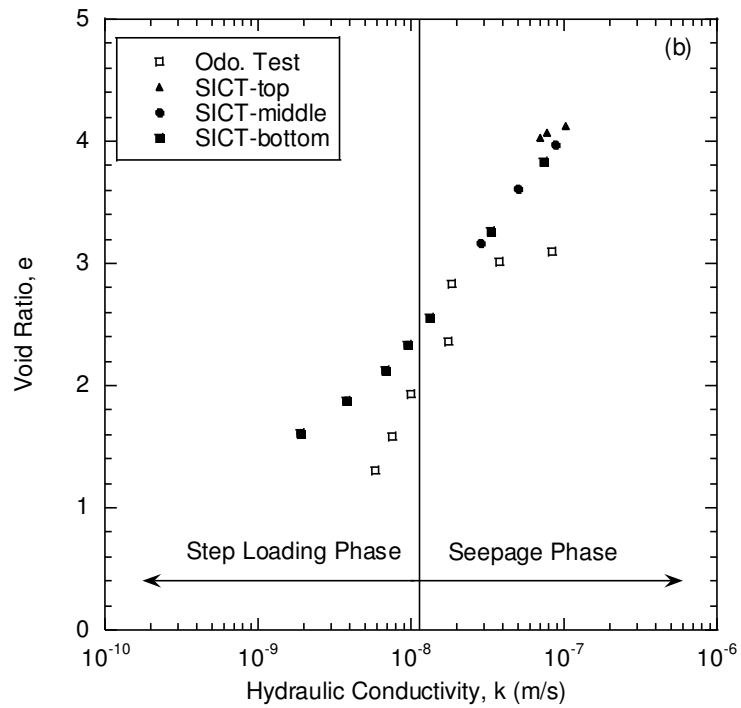
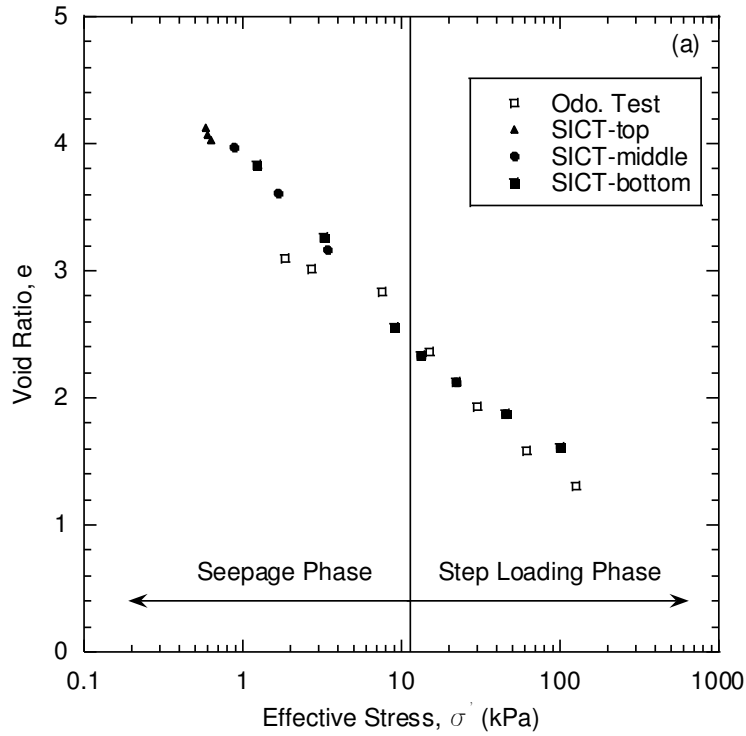


Fig. 5.5. Constitutive relationships of kaolin-1 in SICT and odometer test (a) effective stress-void ratio relationship (b) hydraulic conductivity-void ratio relationship.

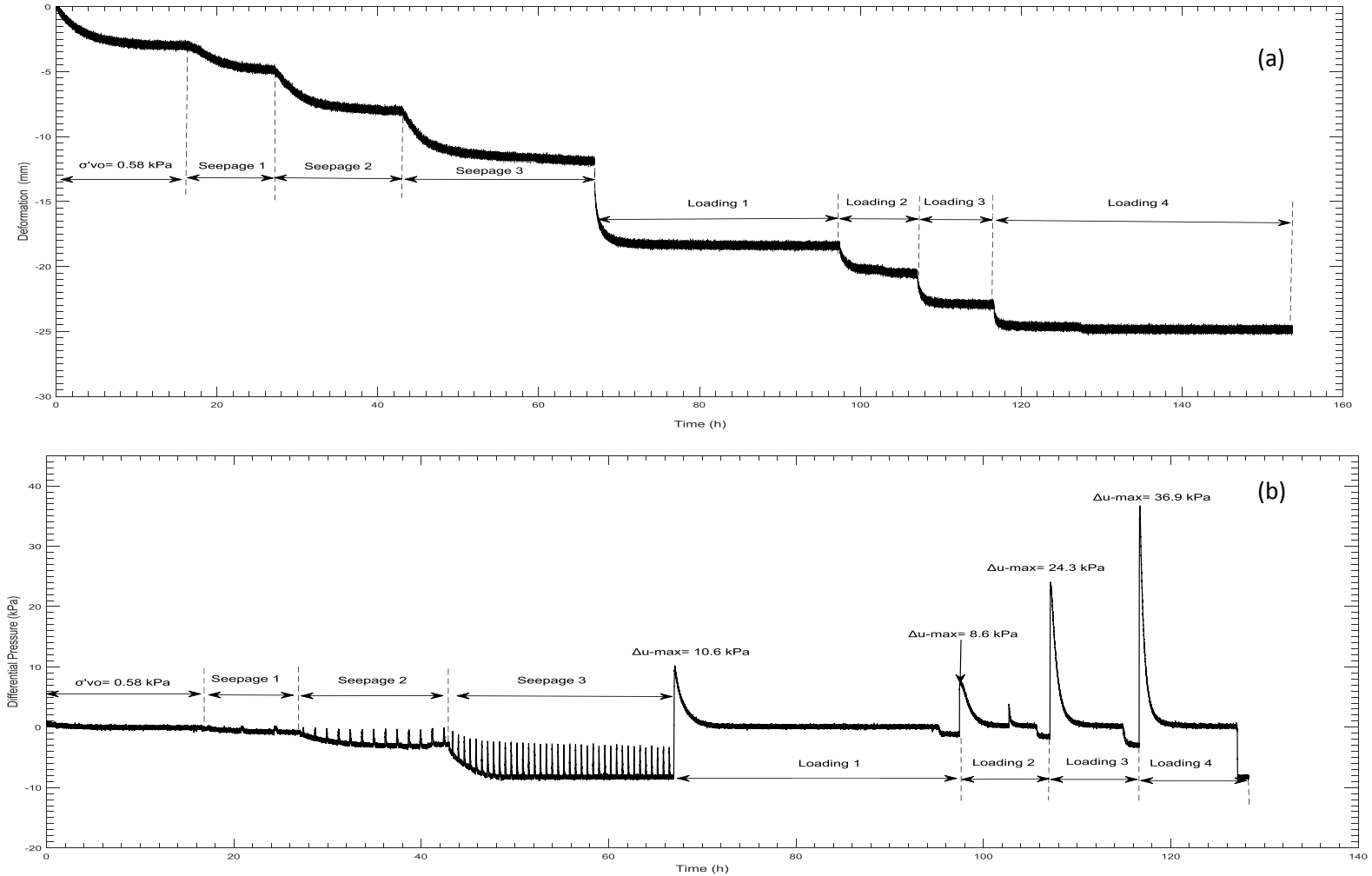


Fig. 5.6. Experimental data of kaolin-2 during SICT: (a) differential pressure across the testing specimen versus time, $\Delta u\text{-max}$ is the maximum excess pore water pressure generated at the bottom of testing specimen (b) deformation versus time; σ'_0 is the sum of self-weight of slurry sample and surcharge load caused by load platen, two extension rods and two LPs. Note: flow rate and applied load for each seepage are provided in Table 5.3.

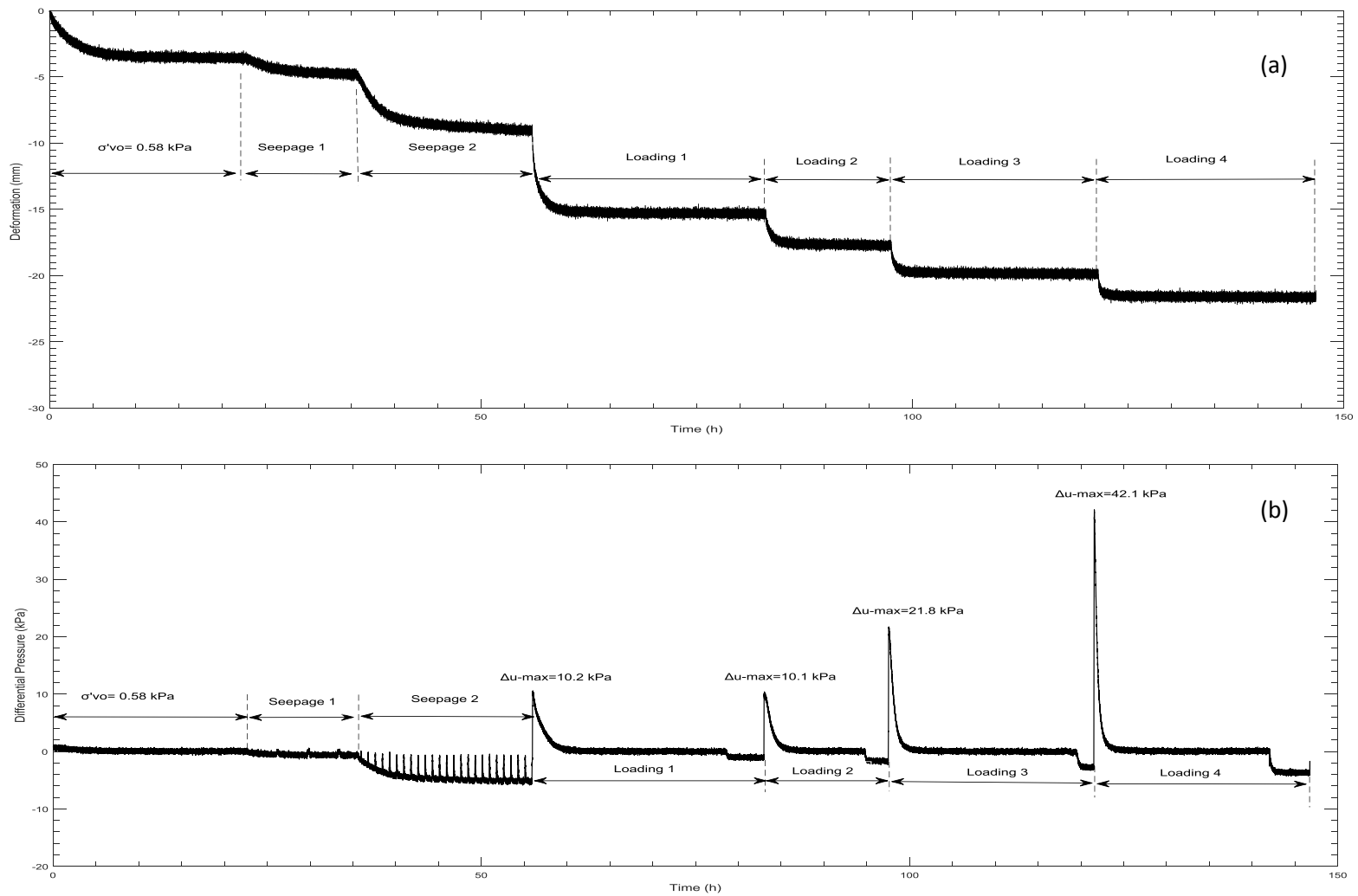


Fig. 5.7. Experimental data of kaolin-2 during SICT: (a) differential pressure across the testing specimen versus time, $\Delta u\text{-max}$ is the maximum excess pore water pressure generated at the bottom of testing specimen (b) deformation versus time; σ'_{vo} is the sum of self-weight of slurry sample and surcharge load caused by load platen, two extension rods and two LPs. Note: flow rate and applied load for each seepage are provided in Table 5.4.

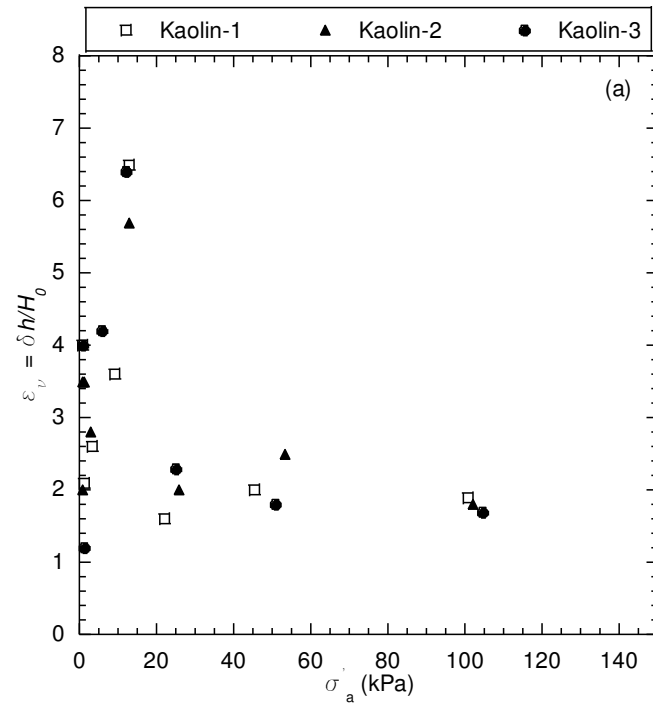
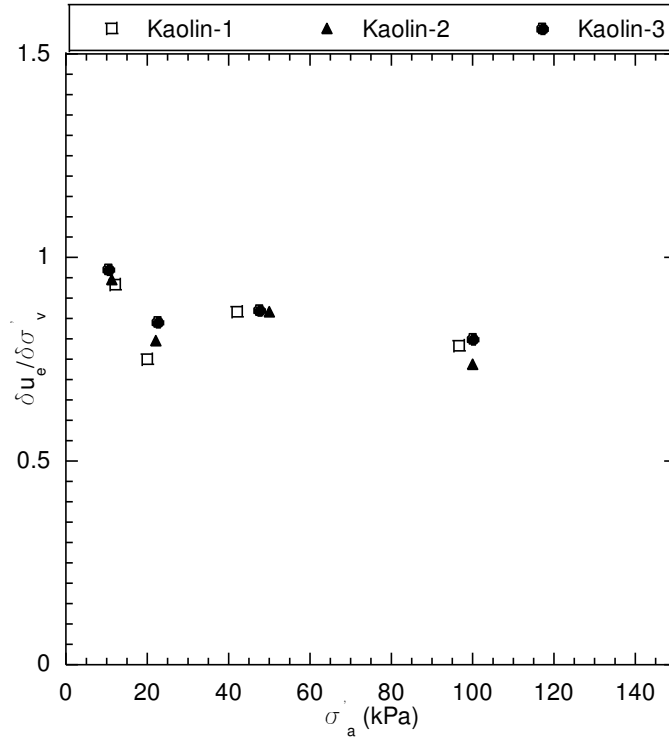


Fig. 5.8. Compilation of percentage pressure change and deformation of three kaolin clay (a) percentage of pressure change for each step loading test (b) deformation of three kaolin clay throughout SICT.

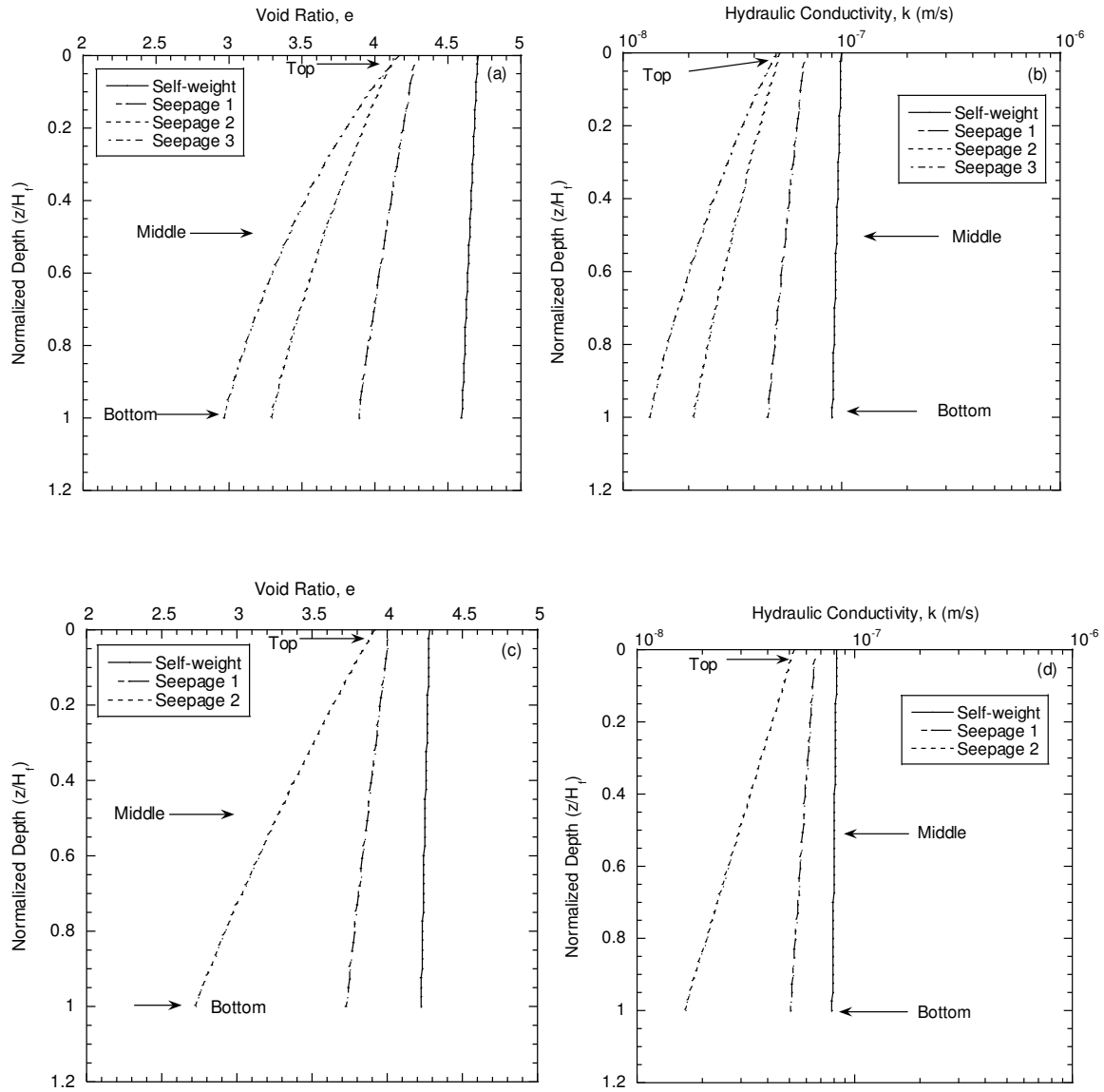


Fig. 5.9. Compilation of variations of void ratio (e) and hydraulic conductivity (k) along soil profile for (a) kaolin-2 (e versus depth), (b) kaolin-2 (k versus depth), (c) kaolin-2 (e versus depth), and (d) kaolin-3 (k versus depth). Variations of e and k of these three materials are at steady state.

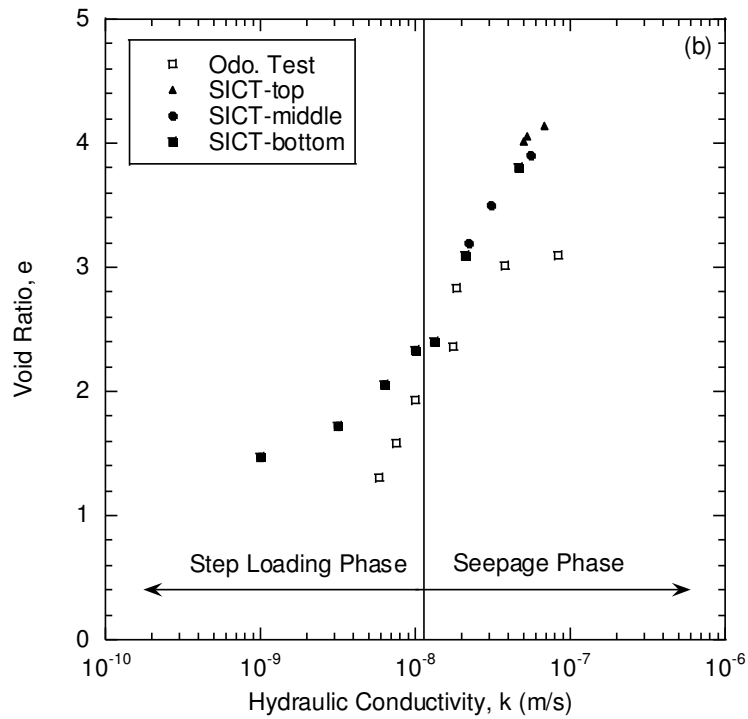
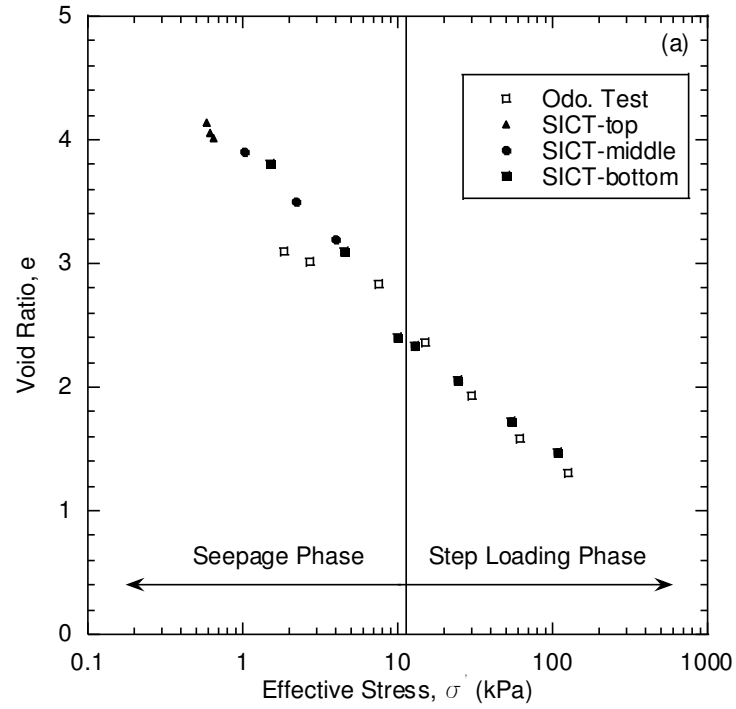


Fig. 5.10. Constitutive relationships of kaolin-2 in SICT and odometer test (a) effective stress-void ratio relationship (b) hydraulic conductivity-void ratio relationship.

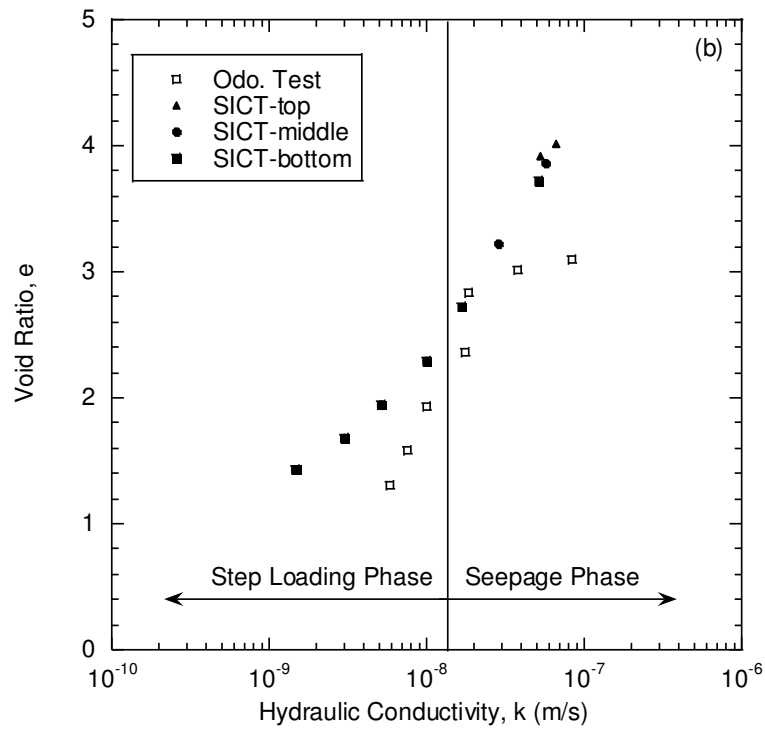
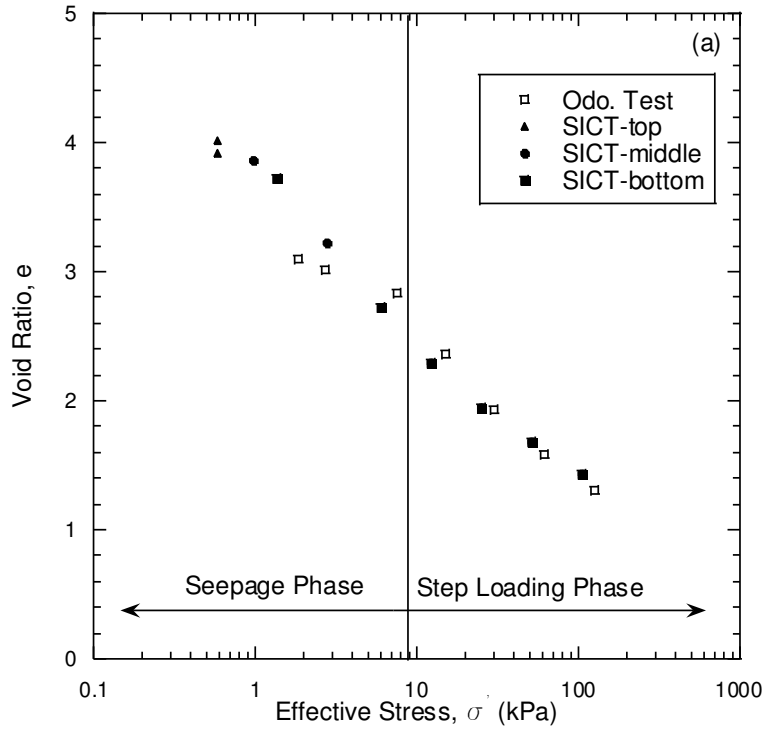


Fig. 5.11. Constitutive relationships of kaolin-3 in SICT and odometer test (a) effective stress-void ratio relationship (b) hydraulic conductivity-void ratio relationship.

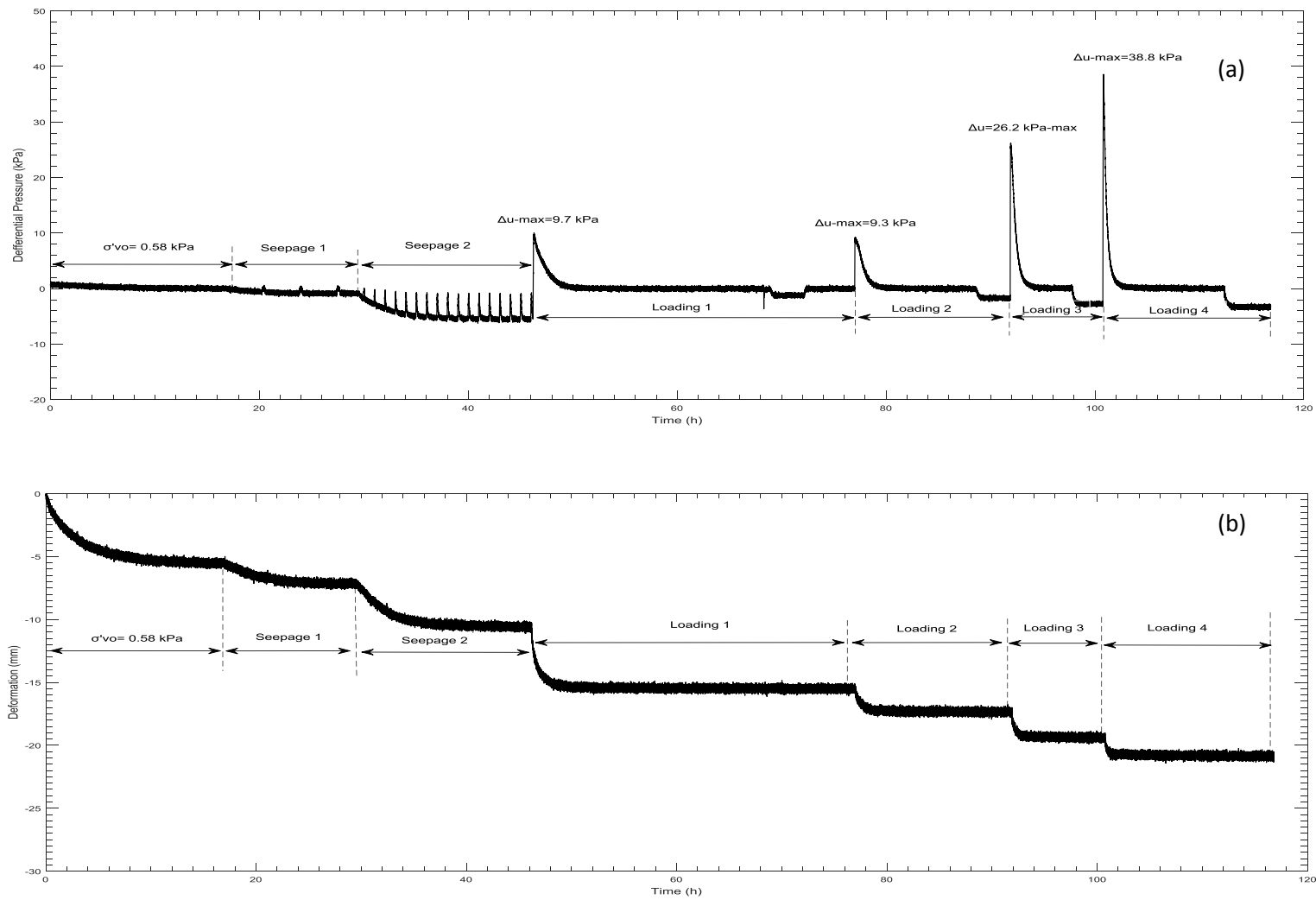


Fig. 5.12. Experimental data of kaolin-2 during SICT: (a) differential pressure across the testing specimen versus time, $\Delta u\text{-max}$ is the maximum excess pore water pressure generated at the bottom of testing specimen (b) deformation versus time; σ'_0 is the sum of self-weight of slurry sample and surcharge load caused by load platen, two extension rods and two LPs. Note: flow rate and applied load for each seepage are provided in Table 5.5.

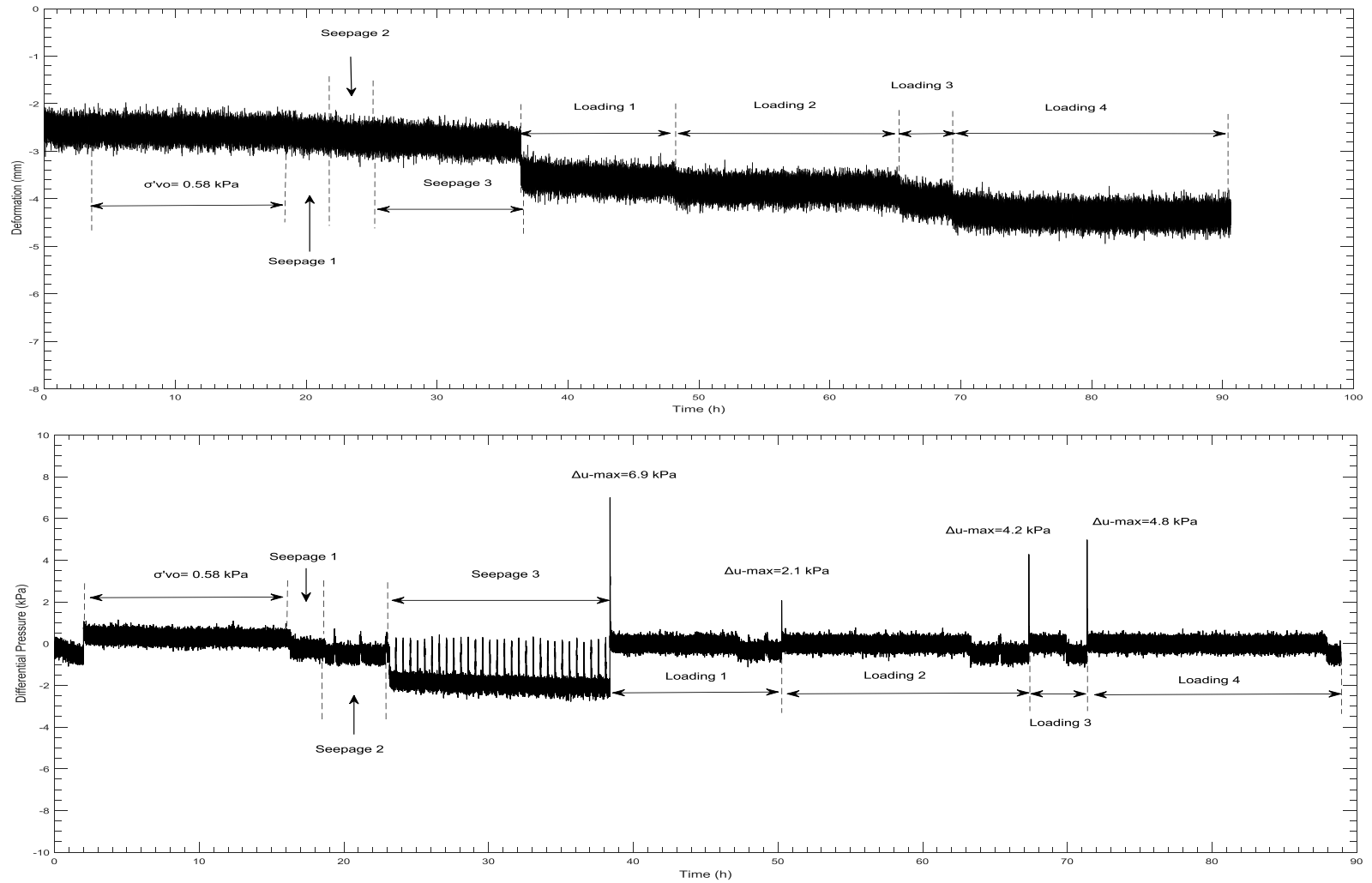


Fig. 5.13. Experimental data of kaolin-2 during SICT: (a) differential pressure across the testing specimen versus time, $\Delta u\text{-max}$ is the maximum excess pore water pressure generated at the bottom of testing specimen (b) deformation versus time; σ'_0 is the sum of self-weight of slurry sample and surcharge load caused by load platen, two extension rods and two LPs. Note: flow rate and applied load for each seepage are provided in Table 5.6.

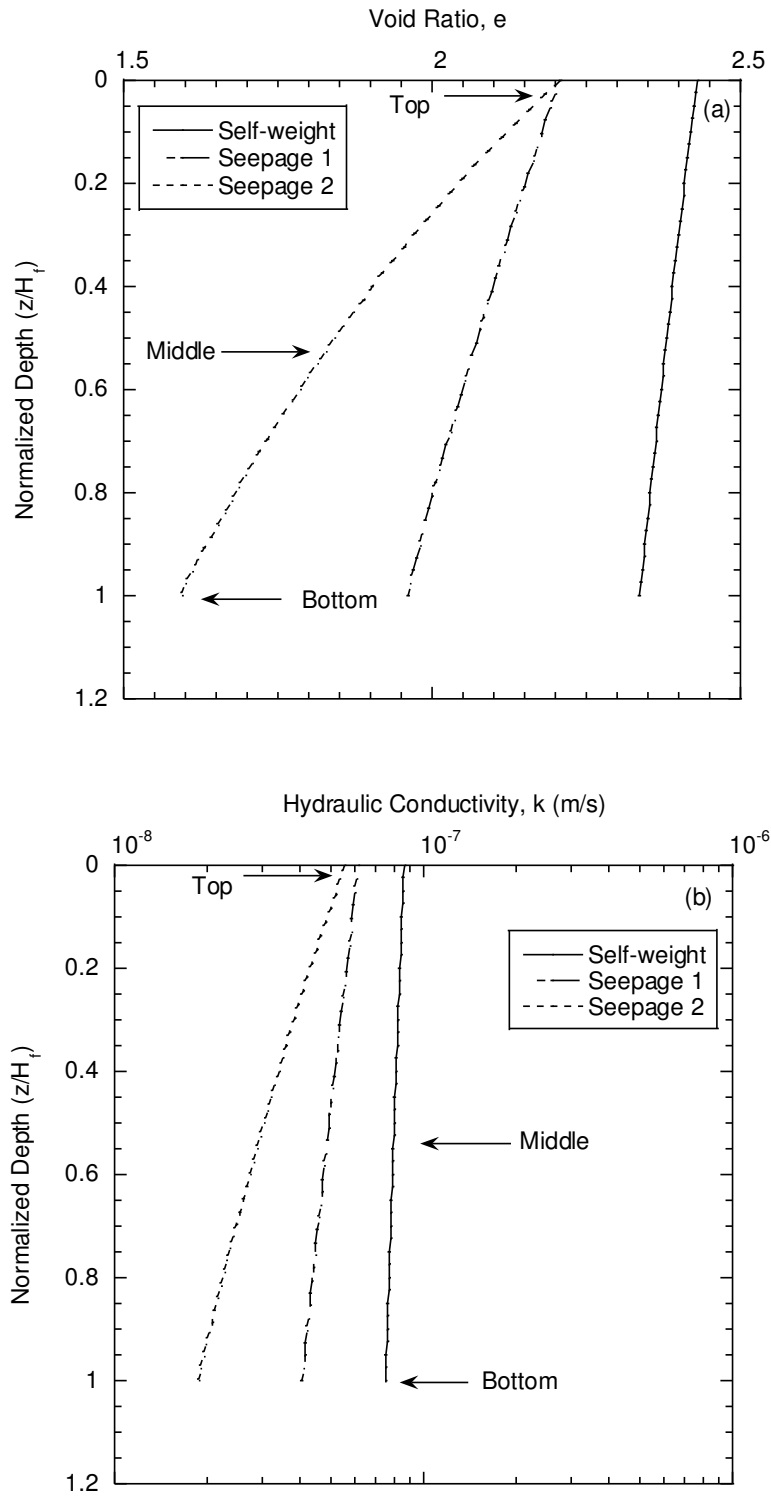


Fig. 5.14. Distributions of (a) void ratio, and (b) hydraulic conductivity for FST during self-weight and seepage consolidation process at steady state.

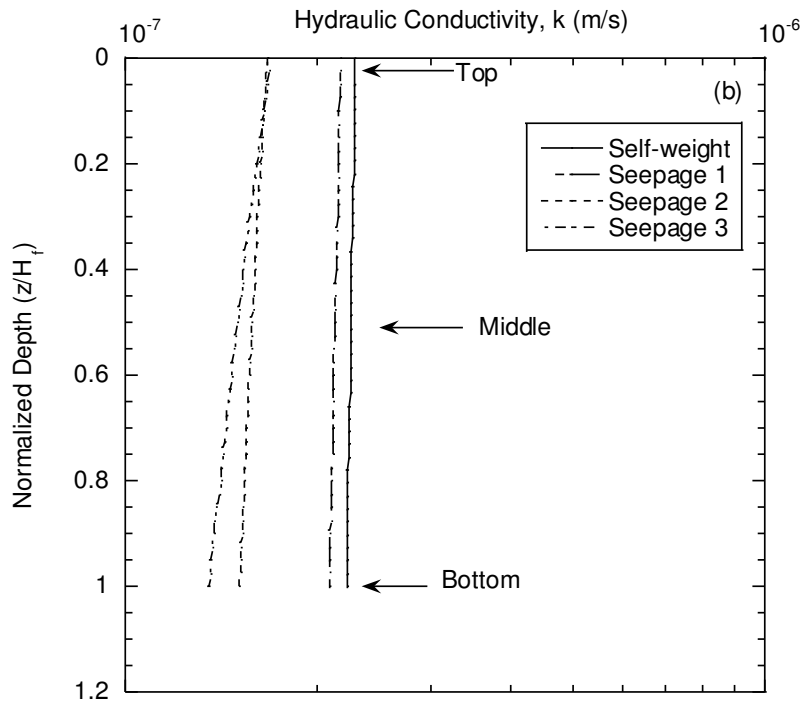
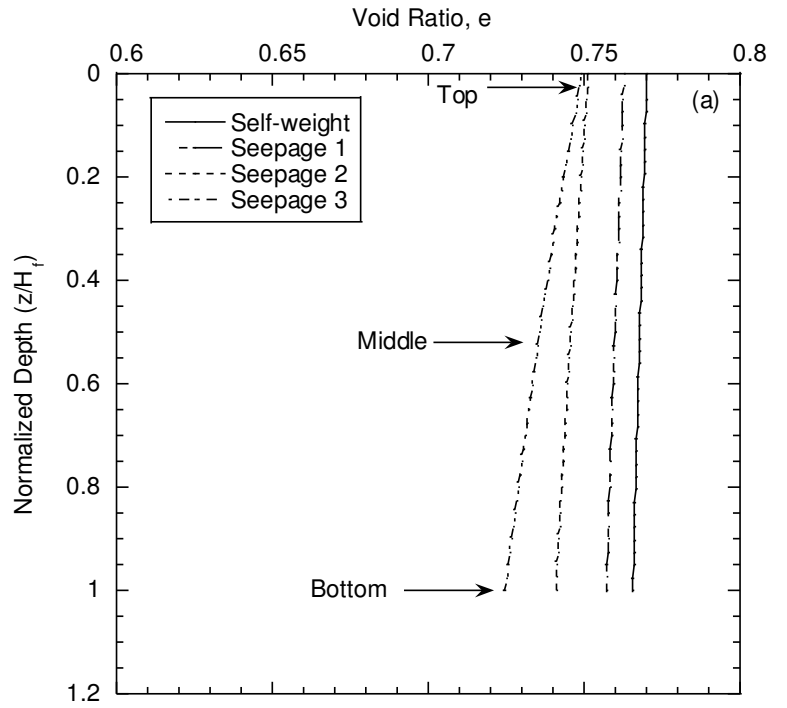


Fig. 5.15. Distributions of (a) void ratio, and (b) hydraulic conductivity for AST during self-weight and seepage consolidation process at steady state.

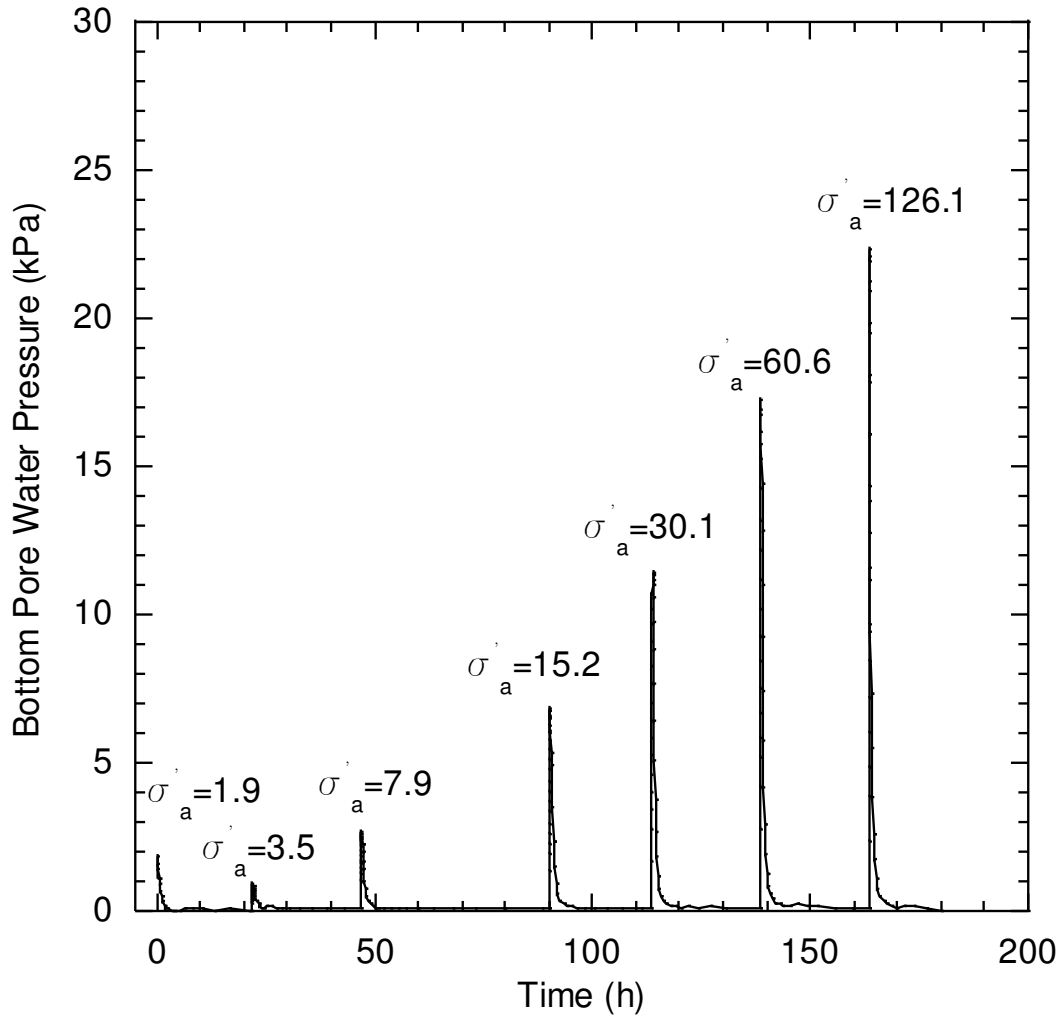


Fig. 5.16. Bottom pressure of FST in odometer test; σ'_a is the applied load.

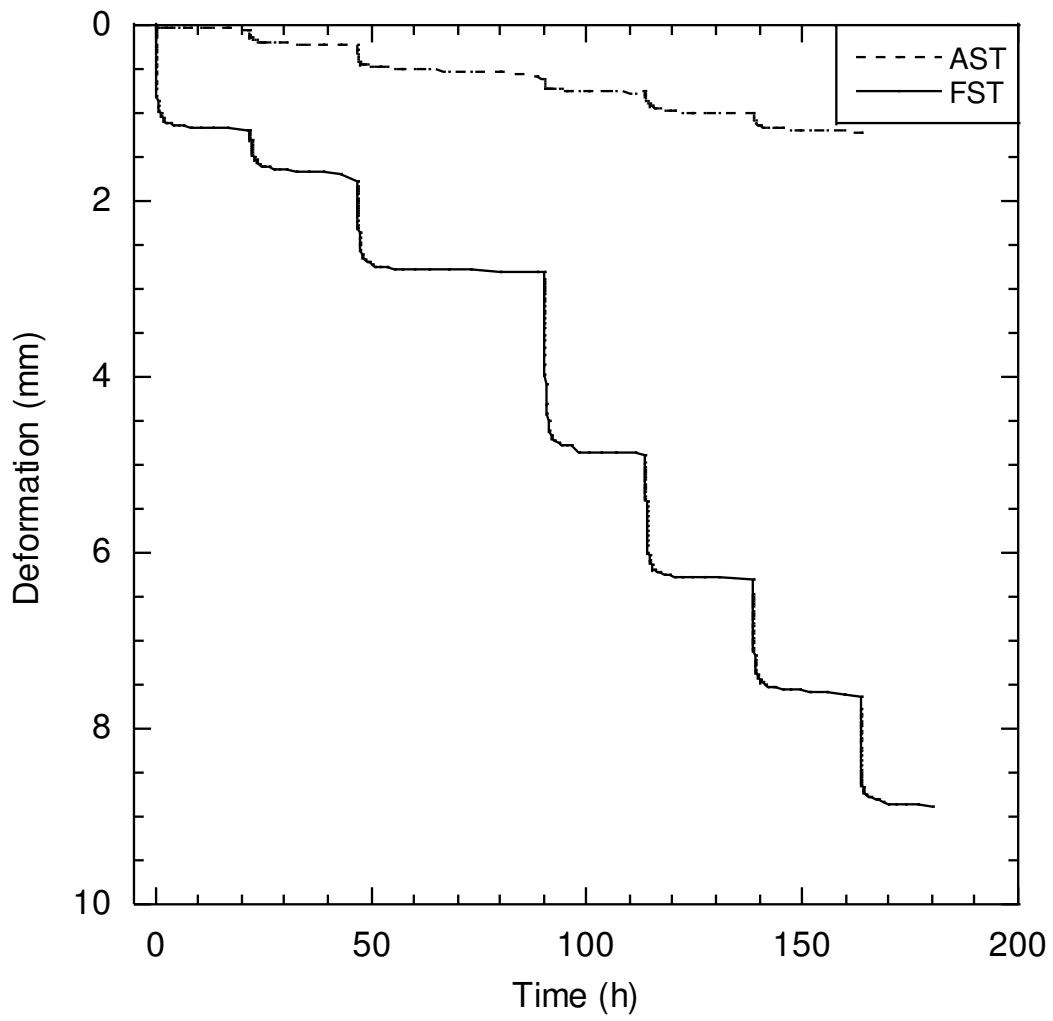


Fig. 5.17. Deformation of AST and FST in odometer test.

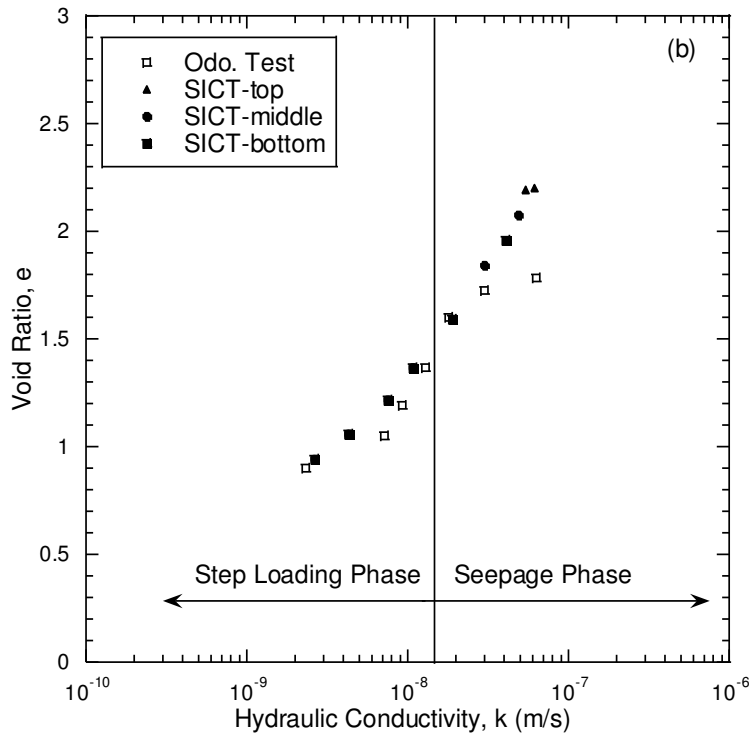
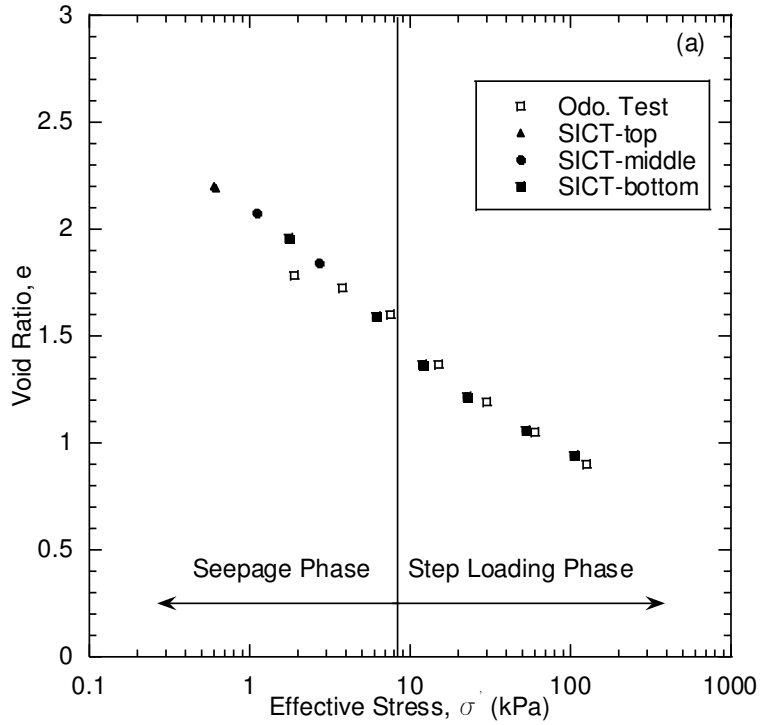


Fig. 5.18. Constitutive relationships of FST in SICT and odometer test (a) effective stress-void ratio relationship (b) hydraulic conductivity-void ratio relationship.

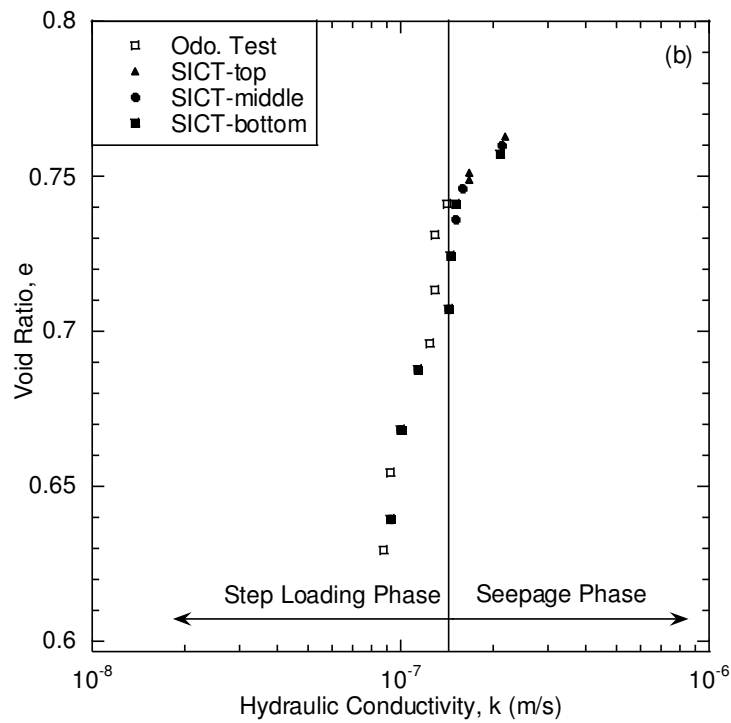
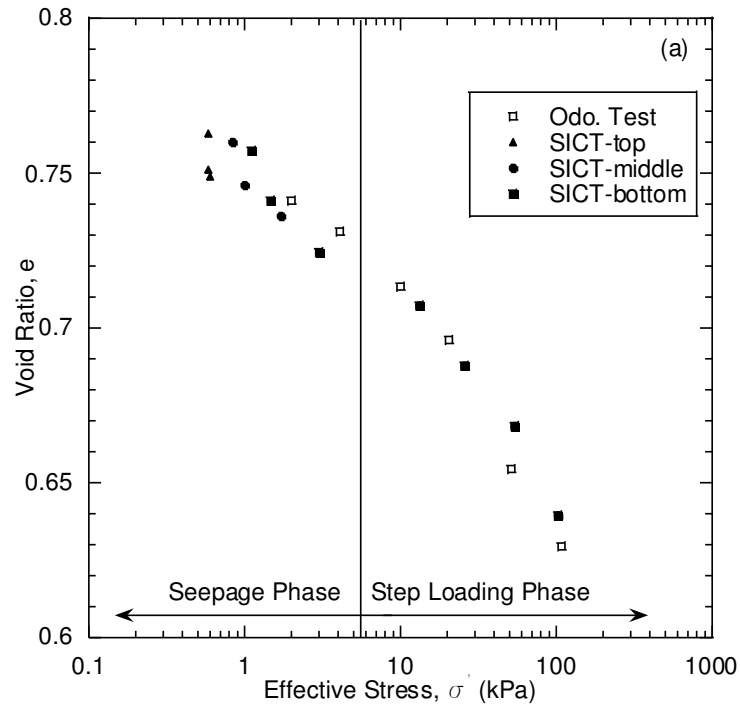


Fig. 5.19. Constitutive relationships of AST in SICT and odometer test (a) effective stress-void ratio relationship (b) hydraulic conductivity-void ratio relationship.

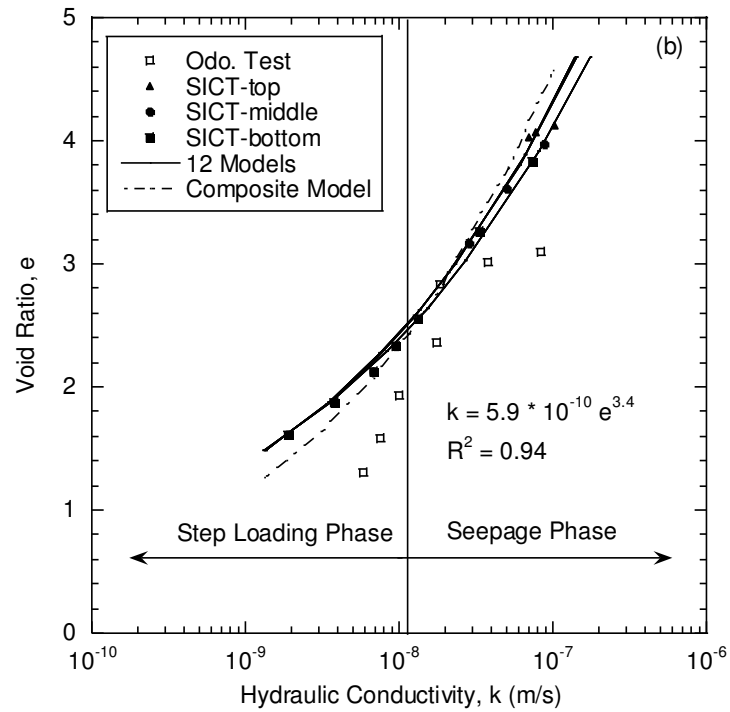
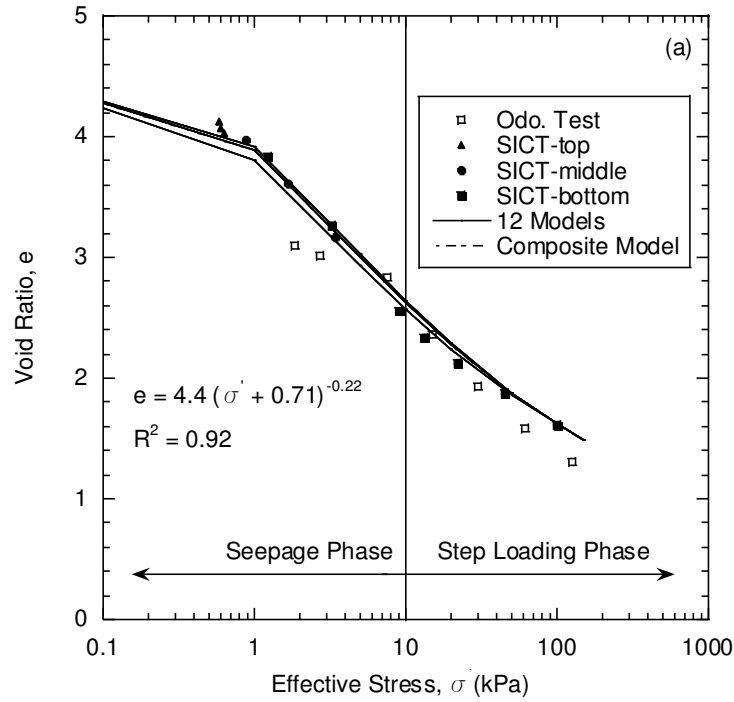


Fig. 5.20. Compilation of constitutive relationship models of three kaolin clay (a) effective stress-void ratio relationship (b) hydraulic conductivity-void ratio relationship.

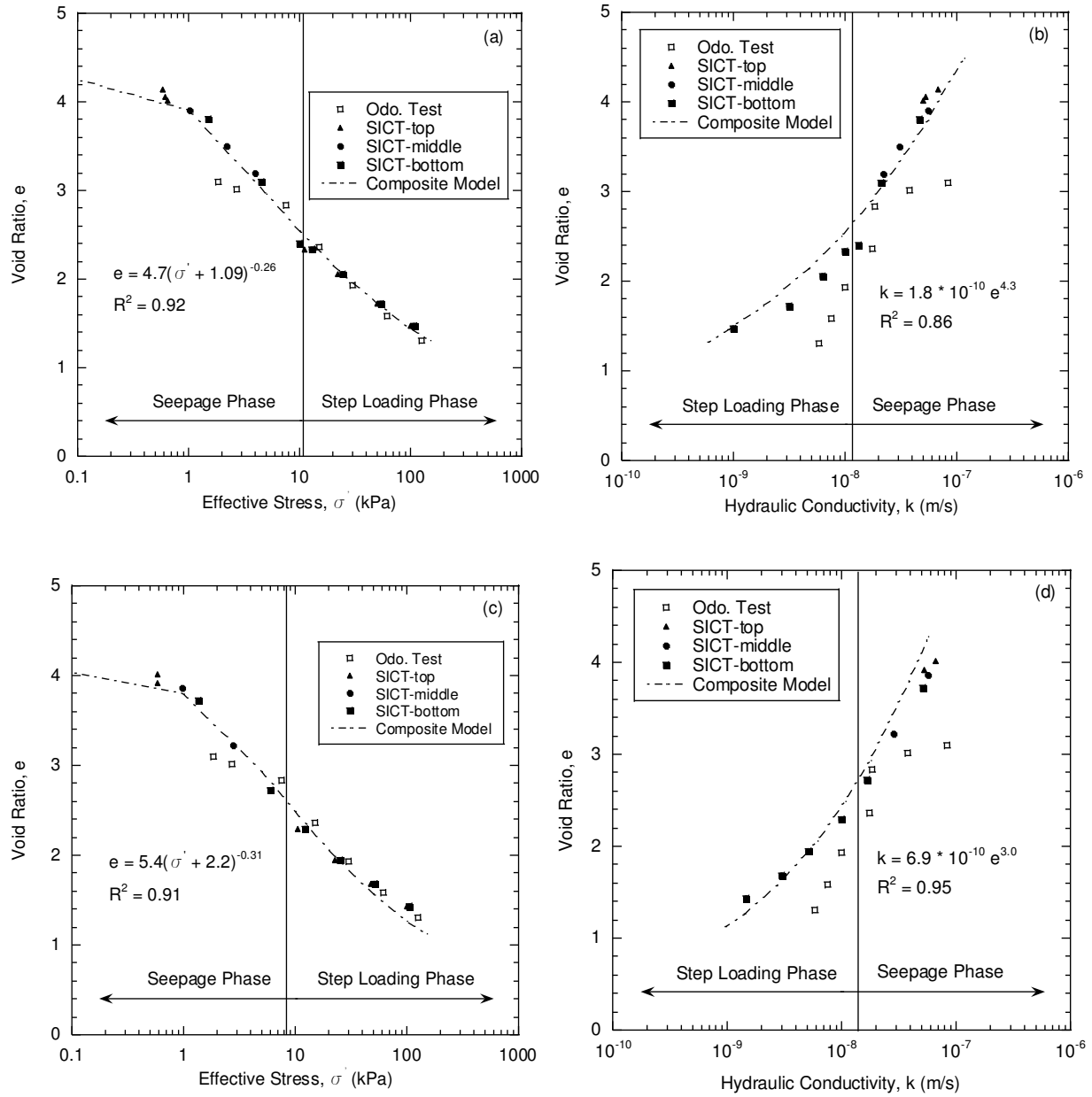


Fig. 5.21. Compilation of composite models for (a) kaolin-2 (e versus effective stress), (b) kaolin-2 (e versus k), (c) kaolin-3 (e versus effective stress), and (d) kaolin-3 (e versus k).

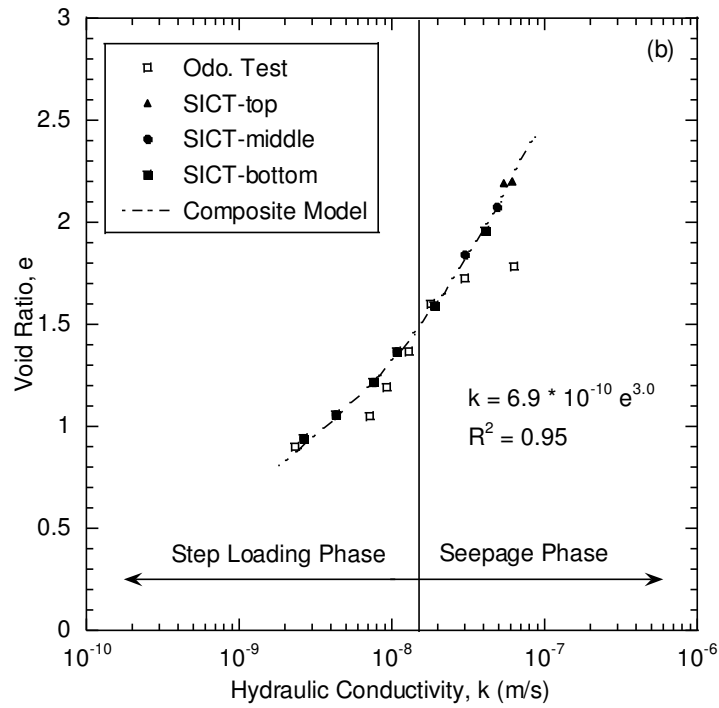
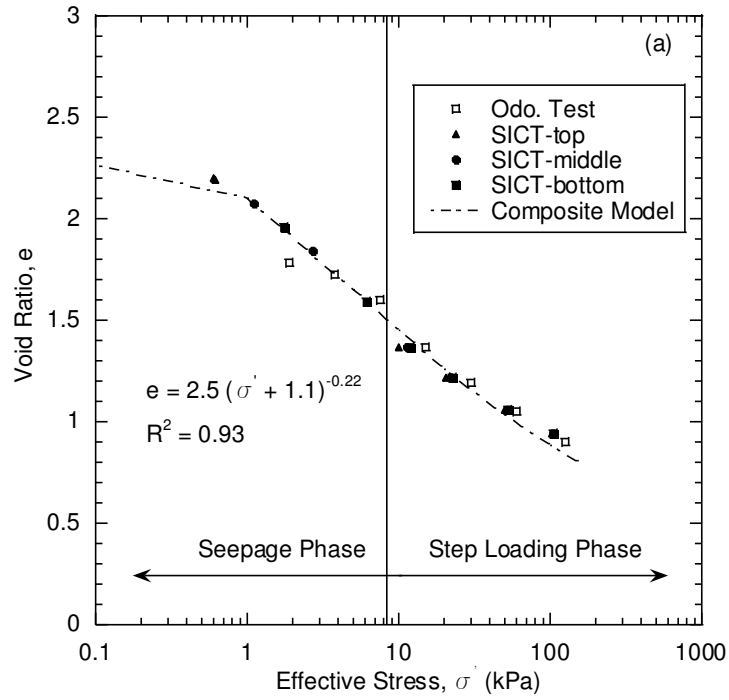


Fig. 5.22. Composite models for FST (a) effective stress-void ratio relationship, (b) hydraulic conductivity-oid ratio relationship.

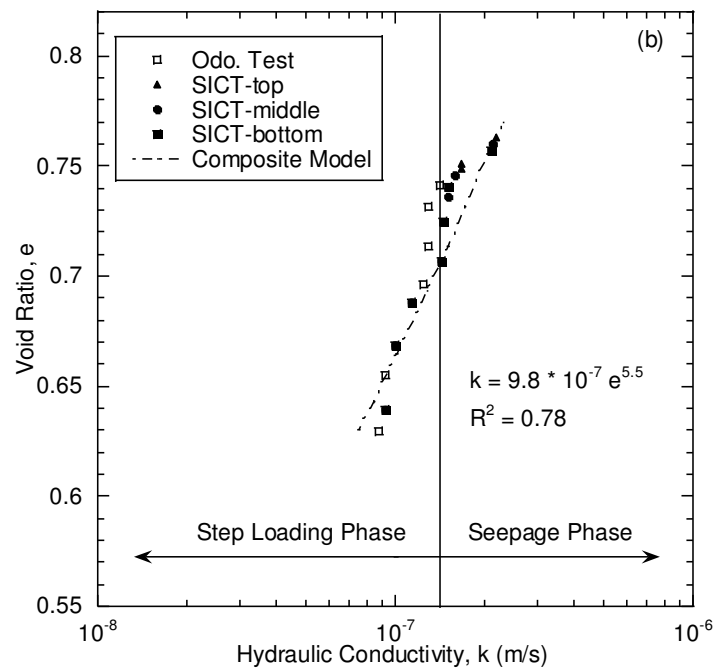
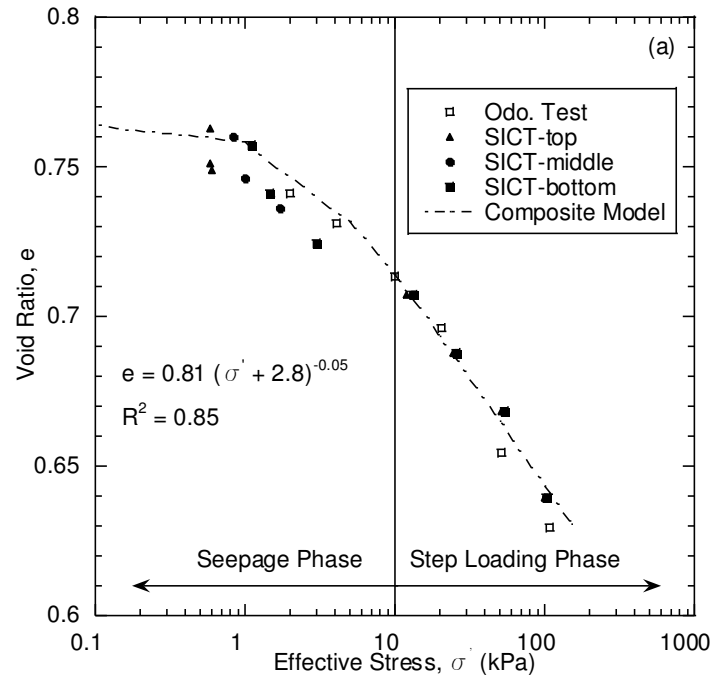


Fig. 5.23. Composite models for AST (a) effective stress-void ratio relationship, (b) hydraulic conductivity-void ratio relationship.

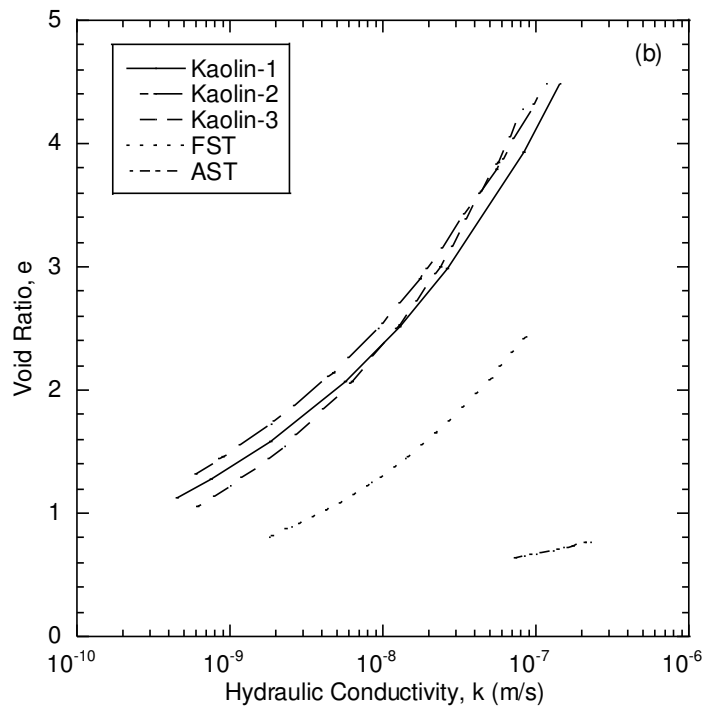
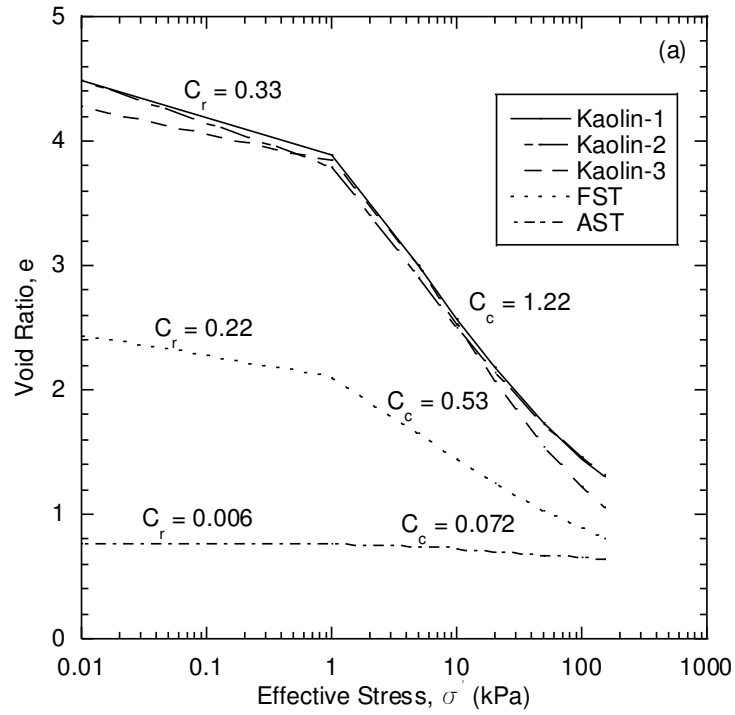


Fig. 5.24. Compilation of constitutive relationships of kaolin, FST and AST (a) effective stress-void ratio relationship (b) hydraulic conductivity-void ratio relationship.

Table 5.1 Material Properties of Slurry Samples in SICT and Odometer Test

Test	Material	SC (%)	e_i	e_0	H_i (m)	H_s (m)
SICT	Kaolin-1	35	4.70	4.50	44.0	7.3
	Kaolin-2	35	4.70	4.50	42.0	7.2
	Kaolin-3	35	4.63	4.28	38.0	7.1
	FST	50	2.63	2.43	46.0	12.0
	AST	73	0.89	0.77	39.0	21.0
Odometer Test	Kaolin	44	3.27	3.20	25.0	5.9
	FST	60	2.10	1.93	25.0	8.6
	AST	75	0.95	0.75	25.0	12.0

Notes: SC = solids content of slurry sample; e_i = initial void ratio; e_0 = void ratio at zero effective stress; H_i = initial height of slurry sample; H_s = initial height of solids in sample; specific gravity (G_s) for these three materials are 2.65.

Table 5.2 SICT Experimental Results on Kaolin-1 at Steady State

Load Stages	u_T (kPa)	u_B (kPa)	$i_{ave.}$	σ_0 (kPa)	σ_a (kPa)	σ_s (kPa)	σ_f (kPa)	Q (ml/min)	v (m/s)	H_f (mm)	k_{tf} (m/s)	k_{mf} (m/s)	k_{bf} (m/s)	e_{tf}	e_{mf}	e_{bf}
Load Platen	2.9	2.9	0	0.58	0	0	0.7	0	0	40.5	1.3×10^{-7}	1.3×10^{-7}	1.3×10^{-7}	4.3	4.3	4.3
Seepage 1	2.9	2.4	1.4	0.58	0	0.5	1.2	0.14	1.3×10^{-7}	38.4	1.0×10^{-7}	7.4×10^{-8}	8.9×10^{-8}	4.1	3.9	3.8
Seepage 2	2.9	0.4	7.2	0.58	0	2.5	3.2	0.4	3.7×10^{-7}	35.8	7.7×10^{-8}	5.1×10^{-8}	3.4×10^{-8}	4.1	3.6	3.3
Seepage 3	2.9	5.4	26.4	0.58	0	8.3	9.0	0.8	7.3×10^{-7}	32.2	7.1×10^{-8}	2.8×10^{-8}	1.3×10^{-8}	4.1	3.2	2.5
Loading 1	2.9	1.7	4.9	0.58	12	1.2	13.9	0.05	4.6×10^{-8}	25.7	9.4×10^{-9}			2.3		
Loading 2	2.9	1.4	6.7	0.58	20	1.6	22.3	0.05	4.6×10^{-8}	24.1	6.9×10^{-9}			2.1		
Loading 3	2.9	0.3	12.0	0.58	42	2.6	45.3	0.05	4.6×10^{-8}	22.1	3.8×10^{-9}			1.9		
Loading 4	2.9	0.8	19.3	0.58	97	3.8	101.5	0.04	3.7×10^{-8}	20.2	1.9×10^{-9}			1.6		

Notes: u_T and u_B represent the top and bottom pressure of soil specimen; $i_{ave.}$ = hydraulic gradient across the specimen; σ_0 = surcharge caused by load platen and two LPs; σ_a = applied load via air cylinder. σ_s = seepage stress caused by flow pump; σ_f = total stress at the bottom of soil specimen; Q = flow rate; v = Darcy velocity; H_f = final sample height; k_{tf} = final hydraulic conductivity at surface of slurry; k_{mf} = final hydraulic conductivity at middle of slurry; k_{bf} = final hydraulic conductivity at bottom of slurry; e_{tf} = final void ratio at surface of slurry; e_{mf} = final void ratio at middle of slurry; e_{bf} = final void ratio at bottom of slurry.

Table 5.3 Experimental Results of Kaolin from Oedometer Test

Day	σ_a (kPa)	c_v (cm ² /s)	a_v (1/kPa)	e_f	k_f (m/s)
1	1.9	6.70×10^{-3}	1.15×10^{-1}	3.04	8.28×10^{-8}
2	2.9	6.70×10^{-2}	2.30×10^{-2}	3.01	3.76×10^{-8}
3	7.5	6.67×10^{-3}	1.09×10^{-1}	2.62	1.86×10^{-8}
4	14.2	9.51×10^{-3}	6.30×10^{-2}	2.14	1.75×10^{-8}
5	29.8	1.18×10^{-3}	2.50×10^{-2}	1.76	9.99×10^{-9}
6	62.0	2.38×10^{-3}	8.41×10^{-3}	1.49	7.61×10^{-9}
7	124.6	3.22×10^{-3}	4.22×10^{-3}	1.26	5.58×10^{-9}

Notes: σ_a = applied load. c_v = coefficient of consolidation (Eq. 2.3); a_v = coefficient of compressibility (Eq. 2.2); e_f = final void; k_f = final hydraulic conductivity across the soil specimen (Eq. 2.1).

Table 5.4 SICT Experimental Results on Kaolin-2 at Steady State

Load Stages	u_T (kPa)	u_B (kPa)	i_{ave}	σ_0 (kPa)	σ_a (kPa)	σ_s (kPa)	σ_f (kPa)	Q (ml/min)	v (m/s)	H_f (mm)	k_{tf} (m/s)	k_{mf} (m/s)	k_{bf} (m/s)	e_{tf}	e_{mf}	e_{bf}
Load Platen	2.9	2.9	0	0.7	0	0	0.7	0	0	38.5	9.0×10^{-8}	9.0×10^{-8}	9.0×10^{-8}	4.3	4.3	4.3
Seepage 1	2.9	2.7	0.6	0.7	0	0.2	0.9	0.14	1.3×10^{-7}	36.5	6.8×10^{-8}	5.5×10^{-8}	4.6×10^{-8}	4.3	4.1	3.8
Seepage 2	2.9	2.3	1.6	0.7	0	0.6	1.3	0.4	3.7×10^{-7}	33.0	5.2×10^{-8}	3.1×10^{-8}	2.1×10^{-8}	4.1	3.6	3.3
Seepage 3	2.9	0.8	5.9	0.7	0	2.1	2.8	0.8	7.3×10^{-7}	30.2	5.0×10^{-8}	2.8×10^{-8}	1.3×10^{-8}	4.1	3.3	2.9
Loading 1	2.9	2.6	0.9	0.7	12	0.3	13	0.05	4.6×10^{-8}	24.5	9.4×10^{-9}			2.3		
Loading 2	2.9	2.3	1.6	0.7	25	0.6	26.3	0.05	4.6×10^{-8}	22.5	6.9×10^{-9}			2.1		
Loading 3	2.9	2.3	1.8	0.7	52	0.6	53.3	0.05	4.6×10^{-8}	20	3.8×10^{-9}			1.9		
Loading 4	2.9	2.2	2.0	0.7	101	0.7	102.4	0.05	4.6×10^{-8}	18.2	1.9×10^{-9}			1.6		

Notes: u_T and u_B represent the top and bottom pressure of soil specimen; i_{ave} = hydraulic gradient across the specimen; σ_0 = surcharge caused by load platen and two LPs; σ_a = applied load via air cylinder. σ_s = seepage stress caused by flow pump; σ_f = total stress at the bottom of soil specimen; Q = flow rate; v = Darcy velocity; H_f = final sample height; k_{tf} = final hydraulic conductivity at surface of slurry; k_{mf} = final hydraulic conductivity at middle of slurry; k_{bf} = final hydraulic conductivity at bottom of slurry; e_{tf} = final void ratio at surface of slurry; e_{mf} = final void ratio at middle of slurry; e_{bf} = final void ratio at bottom of slurry.

Table 5.5 SICT Experimental Results on Kaolin-3 at Steady State

Load Condition	u_T (kPa)	u_B (kPa)	$i_{ave.}$	σ_0 (kPa)	σ_a (kPa)	σ_s (kPa)	σ_f (kPa)	Q (ml/min)	v (m/s)	H_f (mm)	k_{tf} (m/s)	k_{mf} (m/s)	k_{bf} (m/s)	e_{tf}	e_{mf}	e_{bf}
Load Platen	2.9	2.9	0	0.7	0	0	0.7	0	0	34.0	6.8×10^{-8}	1.3×10^{-7}	1.3×10^{-7}	4.0	4.0	4.0
Seepage 1	2.9	2.2	2.1	0.7	0	0.7	1.4	0.14	1.3×10^{-7}	32.8	6.6×10^{-8}	5.8×10^{-8}	5.1×10^{-8}	4.0	3.8	3.7
Seepage 2	2.9	2.4	19.1	0.7	0	5.3	6.0	0.6	5.5×10^{-7}	28.6	5.3×10^{-8}	2.8×10^{-8}	1.7×10^{-8}	3.9	3.2	2.7
Loading 1	2.9	1.9	4.6	0.7	11	1.0	12.7	0.05	4.6×10^{-7}	22.2	9.9×10^{-9}			2.3		
Loading 2	2.9	1.2	8.9	0.7	23	1.7	25.4	0.05	4.6×10^{-8}	19.9	5.2×10^{-9}			1.9		
Loading 3	2.9	0.2	15.4	0.7	48	2.7	51.4	0.05	4.6×10^{-8}	18.1	3.0×10^{-9}			1.7		
Loading 4	2.9	1.0	24.7	0.7	100	4.0	102.4	0.04	3.7×10^{-8}	16.4	1.5×10^{-9}			1.4		

Notes: u_T and u_B represent the top and bottom pressure of soil specimen; $i_{ave.}$ = hydraulic gradient across the specimen; σ_0 = surcharge caused by load platen and two LPs; σ_a = applied load via air cylinder. σ_s = seepage stress caused by flow pump; σ_f = total stress at the bottom of soil specimen; Q = flow rate; v = Darcy velocity; H_f = final sample height; k_{tf} = final hydraulic conductivity at surface of slurry; k_{mf} = final hydraulic conductivity at middle of slurry; k_{bf} = final hydraulic conductivity at bottom of slurry; e_{tf} = final void ratio at surface of slurry; e_{mf} = final void ratio at middle of slurry; e_{bf} = final void ratio at bottom of slurry.

Table 5.6 SICT Experimental Results on FST at Steady State

Load Condition	u_T (kPa)	u_B (kPa)	$i_{ave.}$	σ_0 (kPa)	σ_a (kPa)	σ_s (kPa)	σ_f (kPa)	Q (ml/min)	v (m/s)	H_f (mm)	k_{tf} (m/s)	k_{mf} (m/s)	k_{bf} (m/s)	e_{tf}	e_{mf}	e_{bf}
Load Platen	2.9	3.0	0	0.7	0	0	0.7	0	0	41.0	6.8×10^{-8}	6.8×10^{-8}	6.8×10^{-8}	2.2	2.2	2.2
Seepage 1	2.9	2.00	2.5	0.7	0	1.0	1.7	0.14	1.3×10^{-7}	38.9	6.2×10^{-8}	5.0×10^{-8}	4.1×10^{-8}	2.2	2.1	2.0
Seepage 2	2.9	-2.3	15.0	0.7	0	5.3	6.0	0.5	5.5×10^{-7}	36.0	5.6×10^{-8}	3.0×10^{-8}	1.9×10^{-8}	2.2	1.8	1.6
Loading 1	2.9	1.7	4.2	0.7	10	1.2	11.9	0.05	4.6×10^{-8}	23.0	1.1×10^{-8}			1.4		
Loading 2	2.9	1.3	6.0	0.7	21	1.7	23.4	0.05	4.6×10^{-8}	28.1	7.6×10^{-9}			1.2		
Loading 3	2.9	0.3	10.5	0.7	50	2.7	53.4	0.05	4.6×10^{-8}	26.1	4.4×10^{-9}			1.1		
Loading 4	2.9	-0.3	13.7	0.7	102	3.3	106.0	0.04	3.7×10^{-8}	24.6	2.7×10^{-9}			0.9		

Notes: u_T and u_B represent the top and bottom pressure of soil specimen; i_{ave} = hydraulic gradient across the specimen; σ_0 = surcharge caused by load platen and two LPs; σ_a = applied load via air cylinder. σ_s = seepage stress caused by flow pump; σ_f = total stress at the bottom of soil specimen; Q = flow rate; v = Darcy velocity; H_f = final sample height; k_{tf} = final hydraulic conductivity at surface of slurry; k_{mf} = final hydraulic conductivity at middle of slurry; k_{bf} = final hydraulic conductivity at bottom of slurry; e_{tf} = final void ratio at surface of slurry; e_{mf} = final void ratio at middle of slurry; e_{bf} = final void ratio at bottom of slurry.

Table 5.7 SICT Experimental Results on AST at Steady State

Load Stages	u_T (kPa)	u_B (kPa)	i_{ave}	σ_0 (kPa)	σ_a (kPa)	σ_s (kPa)	σ_f (kPa)	Q (ml/min)	v (m/s)	H_f (mm)	k_{tf} (m/s)	k_{mf} (m/s)	k_{bf} (m/s)	e_{tf}	e_{mf}	e_{bf}
Load Platen	2.9	2.8	0	0.7	0	0	0.7	0	0	36.5	2.3×10^{-7}	2.3×10^{-7}	2.3×10^{-7}	0.77	0.77	0.77
Seepage 1	2.9	2.7	0.6	0.7	0	0.2	0.9	0.14	1.3×10^{-7}	36.3	2.2×10^{-7}	2.1×10^{-7}	2.1×10^{-7}	0.76	0.76	0.76
Seepage 2	2.9	2.3	1.6	0.7	0	0.6	1.3	0.28	2.6×10^{-7}	36.1	1.7×10^{-7}	1.6×10^{-7}	1.5×10^{-7}	0.75	0.75	0.74
Seepage 3	2.9	0.8	5.9	0.7	0	2.1	2.8	1	9.1×10^{-7}	35.9	1.7×10^{-7}	1.5×10^{-7}	1.4×10^{-7}	0.75	0.74	0.73
Loading 1	2.9	2.6	0.9	0.7	12	0.3	13.0	0.14	1.3×10^{-7}	35.3	1.3×10^{-7}			0.71		
Loading 2	2.9	2.3	1.6	0.7	25	0.6	26.3	0.2	1.8×10^{-7}	34.9	1.1×10^{-7}			0.69		
Loading 3	2.9	2.3	1.8	0.7	52	0.6	53.3	0.2	1.8×10^{-7}	34.5	7.1×10^{-8}			0.67		
Loading 4	2.9	2.2	2.0	0.7	101	0.7	102.4	0.2	1.8×10^{-7}	33.9	2.8×10^{-9}			0.64		

Notes: u_T and u_B represent the top and bottom pressure of soil specimen; i_{ave} = hydraulic gradient across the specimen; σ_0 = surcharge caused by load platen and two LPs; σ_a = applied load via air cylinder. σ_s = seepage stress caused by flow pump; σ_f = total stress at the bottom of soil specimen; Q = flow rate; v = Darcy velocity; H_f = final sample height; k_{tf} = final hydraulic conductivity at surface of slurry; k_{mf} = final hydraulic conductivity at middle of slurry; k_{bf} = final hydraulic conductivity at bottom of slurry; e_{tf} = final void ratio at surface of slurry; e_{mf} = final void ratio at middle of slurry; e_{bf} = final void ratio at bottom of slurry.

Table 5.8 Experimental Results of FST from Odometer Test

Day	σ'_a (kPa)	c_v (cm ² /s)	a_v (1/kPa)	e_f	k_f (m/s)
1	1.89	2.55×10^{-3}	7.20×10^{-2}	1.78	6.36×10^{-8}
2	3.50	1.41×10^{-3}	5.90×10^{-2}	1.73	2.97×10^{-8}
3	7.90	1.56×10^{-3}	3.14×10^{-2}	1.60	1.81×10^{-8}
4	15.15	1.05×10^{-3}	3.10×10^{-2}	1.37	1.30×10^{-8}
5	30.10	2.0×10^{-3}	1.07×10^{-2}	1.19	9.24×10^{-9}
6	60.62	3.15×10^{-3}	4.91×10^{-3}	1.05	7.24×10^{-9}
7	126.05	2.10×10^{-3}	2.21×10^{-3}	0.90	2.35×10^{-9}

Notes: σ'_a = applied load. c_v = coefficient of consolidation (Eq. 2.3); a_v = coefficient of compressibility (Eq. 2.2); e_f = final void; k_f = final hydraulic conductivity across the soil specimen (Eq. 2.2).

Table 5.9 Experimental Results of AST from Odometer Test

Day	σ'_a (kPa)	c_v (cm ² /s)	a_v (1/kPa)	e_f	k_f (m/s)
1	2.02	1.50×10^{-1}	1.68×10^{-3}	0.74	1.42×10^{-5}
2	4.04	3.80×10^{-2}	6.05×10^{-3}	0.73	1.30×10^{-5}
3	10.13	1.10×10^{-1}	2.05×10^{-3}	0.72	1.29×10^{-5}
4	20.26	1.81×10^{-1}	1.18×10^{-3}	0.69	1.23×10^{-5}
5	51.92	1.86×10^{-1}	8.37×10^{-4}	0.66	9.24×10^{-8}
6	107.12	3.65×10^{-1}	4.03×10^{-4}	0.63	8.84×10^{-9}

Notes: σ'_a = applied load. c_v = coefficient of consolidation (Eq. 2.3); a_v = coefficient of compressibility (Eq. 2.2); e_f = final void; k_f = final hydraulic conductivity across the soil specimen (Eq. 2.2).

CHAPTER 6: SUMMARY AND CONCLUSION

The consolidation behavior of kaolin clay and synthetic tailings was evaluated by a seepage induced consolidation test (SICT) and odometer to study the following functions of a SICT apparatus constructed at Colorado State University (CSU): (i) the reliability and repeatability of the developed SICT apparatus; (ii) the effect of slurry composition on the consolidation behavior of mine tailings; (iii) methods to calculate the constitutive relationships of slurried mine tailings. SICT is based on large-strain consolidation theory and odometer test is based on small-strain consolidation theory.

The following conclusions are drawn from this study:

- Consolidation behavior (void ratio vs. effective stress; $e-\sigma'$) of kaolin generated from SICT and odometer are comparable, and repeatable. Hydraulic conductivities (k) measured from three tests on kaolin are comparable; however, k measured from odometer tests underestimate k directly measure by the SICT.
- Different consolidation behavior ($e-\sigma'$ and $e-k$) are observed from FST and AST due to different slurry composition (different fractions of clay, silt, and sand sized particles). The variations of e and k for FST have a greater magnitude than AST because FST contains 60% clay and 40% silt, while AST contains 20% sand and 80% silt.
- Twelve sets of constitutive relationship parameters were generated from twelve possible combinations of seepage test phase and step loading test phase data from kaolin slurry. Compression and permeability relationships modeled from the twelve permutations of constitutive parameters closely matched, and fit measured kaolin data. A composite model incorporating all measured data from seepage test phases and step loading test phases from a given SICT is used to simulate the consolidation behavior of kaolin and compare the consolidation-permeability data of different materials. Composite and

paired seepage-step test phase constitutive models are comparable. The composite model is used to simulate consolidation behavior of three replicate tests on kaolin, as well as FST and AST; simulated relationships match experimental data.

- Consolidation behavior ($e-\sigma'$ and $e-k$) of kaolin clay, FST, and AST modeled based on data from the SICT show a substantial difference because of slurry composition.

REFERENCES

- Abu-Hejleh, A. N. & Znidarčić, D., (1992). User Manual for Computer Program SICTA, Bartaw, Florida: FIPR: *Florida Institute of Phosphate Research*.
- Abu-Hejleh, A. N. & Znidarčić, D., (1994). Estimation of the Consolidation Constitutive Relations. *Computer Methods and Advances in Geomechanics*, pp. 499-504.
- Abu-Hejleh, A. N., and Znidarcic D. (1992). User manual for computer program SICTA, Report prepared for FIPR, Dept, of Civil Engineering, University of Colorado, Boulder, Co.
- Abu-Hejleh, A. N., Znidarcic D., and Barnes B. (1996). Consolidation characteristics of phosphatic clays. *Journal of Geotechnical Engineering*, 122(4), pp. 295-301.
- Alhomair, A. Sultan (2016). Hydraulic conductivity of fly ash-amended mine tailings, M.S. Thesis, The Faculty of Graduate Studies, Department of Civil and Environmental Engineering, Colorado State University, Fort Collins, Colorado, USA.
- ASTM (2011). Standard practice for classification of soils for engineering purposes (Unified soil classification system), ASTM D 2487 - 11, ASTM International, West Conshohocken, Pennsylvania, USA.
- ASTM (2011). Standard test methods for one-dimensional consolidation properties of soils using incremental loading, ASTM D 2435 - 11, ASTM International, West Conshohocken, Pennsylvania, USA.
- Been, K., Sills, G. C., (1981). Self-weight consolidation of soft soils: an experimental and theoretical study *Géotechnique*, 31 (4) (1981), pp. 519-535
- BGC Engineering Inc. (2010). Oil sands tailings technology review, *Oil Sands Research and Information Network*.
- Bonin, M.D. et al., (2014). Experimental Study and Numerical Reproduction of Self-Weight Consolidation Behavior of Thickened Tailings. *Journal of Geotechnical and Geoenvironmental Engineering*, 140(12), pp.1–10.
- Caldwell, J.A., Ferguson K., Schiffman R.L., and Van Zyl D. (1984). Application of finite strain consolidation theory for engineering design and environmental planning of mine tailings impoundments, *Sedimentation Consolidation Models – Predictions and Validation*, 581-606.
- Carrier, D., Bromwell L., and Somogyi F. (1983). Design capacity of slurried mineral waste ponds, *Journal of Geotechnical Engineering*, 109(5): 699-716.
- Chakrabarti, S., and Horvath, P., (1986). "Conventional Consolidation Tests on Two Soils," *Proceedings on Consolidation of Soils: Testing and Evaluation: ASTM STP 892*, Baltimore, MD, ASTM International, West Conshohocken, PA, pp. 451– 464. [16]

- Chalaturnyk, R. J., Scott, J. D. & Ozum, B., (2002). Management of Oil Sand Tailings. *Petroleum Science and Technology*, 20(9 & 10), pp. 1025-1046.
- Coduto, P. D., Yeung, R. M., Kitch, A. W. (2014). *Geotechnical Engineering: principles and practices*, 2nd ed. Upper Saddle River, New Jersey 07458, U.S.A.
- Estepho, M. (2014). Seepage induced consolidation test: characterization of mature fine tailings, M.S. Thesis, The Faculty of Graduate Studies, Mining Engineering, The University of British Columbia, Vancouver.
- Fox, P. J. and Berles, J. D. (1997). CS2: a piecewise-linear model for large-strain consolidation, *International Journal for Numerical and Analytical Methods in Geomechanics*, 21(7), 453-475.
- Gibson, R.E., England, G.L., and Hussey M.J. (1967). The theory of one-dimensional consolidation of saturated clays, *Geotechnique*, 17(3), 261-273
- Gjerapic, G., Johnson J., Coffin J., and Znidarcic D. (2008). Determination of tailings impoundment capacity via finite-strain consolidation models, *GeoCongress 2008*, ASCE, pp. 798-805.
- Hamade P. Matteus, (2016). Un-drained shear behavior of mixed min waste rock and tailings, M.S. Thesis, The Faculty of Graduate Studies, Department of Civil and Environmental Engineering, Colorado State University, Fort Collins, Colorado, USA.
- Huerta, A., Kriegsmann G., and Krizek R. (1988). Permeability and compressibility of slurries from seepage-induced consolidation, *Journal of Geotechnical Engineering*, 114(5), 614-627.
- Imai, G. (1981). Experimental studies on sedimentation mechanism and sediment formation of clay materials, *Soils and Foundations*, 21(1), 7-20.
- Imai, G., (1979). Development of a New Consolidation Test Procedure Using Seepage Force. *Soils and Foundations*, 19(3), pp. 45-60.
- Jeeravipoolvarn, S., (2005). Compression Behaviour of Thixotropic Oil Sands Tailings, Edmonton, Alberta: MASC Thesis, University of Alberta.
- Jeeravipoolvarn, S., (2005). *Compression Behaviour of Thixotropic Oil Sands Tailings*, Edmonton, Alberta: MASC Thesis, University of Alberta.
- Koppula, S. D. (1970). The consolidation of soil in two dimensions and with moving boundaries, PhD Dissertation, Department of Civil Engineering, University of Alberta, Edmonton, Canada.
- Lee, K., (1979). *An analytical and experimental study of large strain soil consolidation*, s.l.: PhD Thesis at the University of Oxford for the degree of Doctor of Philosophy. Leipzig-Vienna
- Liu, J. and Znidarcic, D. (1991). Modeling one-dimensional compression characteristics of soils, *Journal of Geotechnical Engineering*, 117(1), 162-169

- Mitchell, J. (1976). *Fundamentals of Soil Behavior*, John Wiley & Sons, Inc., New York.
- Pollock, G. W., (1988). *Large Strain Consolidation of Oil Sand Tailings Sludge*, Edmonton, Alberta: M.Sc. Thesis Department of Civil Engineering.
- Priscu, C., (1999). Behavior of mine tailings dams under high tailings deposition rates, Ph.D. Thesis, Department of Mining and Metallurgical Engineering, McGill University, Montreal, Canada.
- Schiffman, R., Vick, S., and Gibson, R. (1988). Behavior and properties of hydraulic fills. Hydraulic fill structures, *Conference of the American Society of Civil Engineer- American Institute of Mining, Metallurgical, and Petroleum Engineers (ASCE-AIME)*, Fort Collins, CO, pp. 166-202
- Somogyi, F. (1980). Large-strain consolidation of fine-grained slurries, *Annual conference, Canadian Society for Civil Engineering*, Winnipeg, Canada.
- Suthaker, N. N., (1995). *Geotechnics of Oil Sand Fine Tailings*, Edmonton: PhD; Department of Civil Engineering, University of Alberta. Pollock, G. W., 1988. *Large Strain Consolidation of Oil Sand Tailings Sludge*, Edmonton, Alberta: M.Sc. Thesis Department of Civil Engineering.
- Taylor, D. (1948). *Fundamentals of Soil Mechanics*, Wiley, New York.
- Terzaghi K (1925) *Erdbaumechanik auf Bodenphysikalischer Grundlage*. Franz Deuticke.
- West, J. (2011). Decreasing metal ore grades, *Journal of Industry Ecology*, Yale University, 15(2), pp. 165-168.
- Yilmaz. E., Belem, T., Benzaazoua, M., and Bussi re, B. (2010). Assessment of the modified CUAPS apparatus to estimate in situ properties of cemented paste backfill, *Geotechnical Testing Journal*, 33(5), 1-12.
- Znidarcic, D., Abu-Hejleh N., Fairbanks T., and Robertson A. (1992). Consolidation characteristics determination for phosphatic clays, Vol 1 Seepage Induced Consolidation Test Equipment Description and User's Manual, Prepared for Florida Institute of Phosphate Research, University of Boulder, Boulder.
- Znidarcic, D., Abu-Hejleh N., Fairbanks T., and Robertson A. (1992). Consolidation characteristics determination for phosphatic clays, Vol 2 User Manual for Computer Program SICTA, Prepared for Florida Institute of Phosphate Research, University of Boulder, Boulder.
- Znidarcic, D., Abu-Hejleh N., Fairbanks T., and Robertson A. (1992). Consolidation characteristics determination for phosphatic clays, Vol 3 Results of Seepage Induced Consolidation Tests of Phosphatic Clays, Prepared for Florida Institute of Phosphate Research, University of Boulder, Boulder.
- Znidarcic, D. (1999). Predicting the behavior of disposed dredging soils, *Geotechnical Engineering for Transportation Infrastructure*, Balkema, Rotterdam, pp. 877-886.

Znidarcic, D., Miller, R., Van Zyl, D., Fredlund, M., and Wells, S. (2011). Consolidation testing of oil sand fine tailings, Proceedings *Tailings and Mine Waste 2011*, Norman B. Keevil Institute of Mining Engineering, Vancouver, BC, Canada, pp. 251-257.

APPENDIX A: SEEPAGE-INDUCED CONSOLIDATION TESTING

A schematic of the SICT apparatus is provided in Fig. 3.2 and the step by step SICT procedure includes: (i) saturation of lines; (ii) sample preparation; (iii) seepage test; and (iv) step loading test. Step by step test procedure is provided below:

A.1 Saturation of Lines

A.1.1 Apply vacuum grease around the outside edge of the sample pedestal and on the bottom of the sample casing.

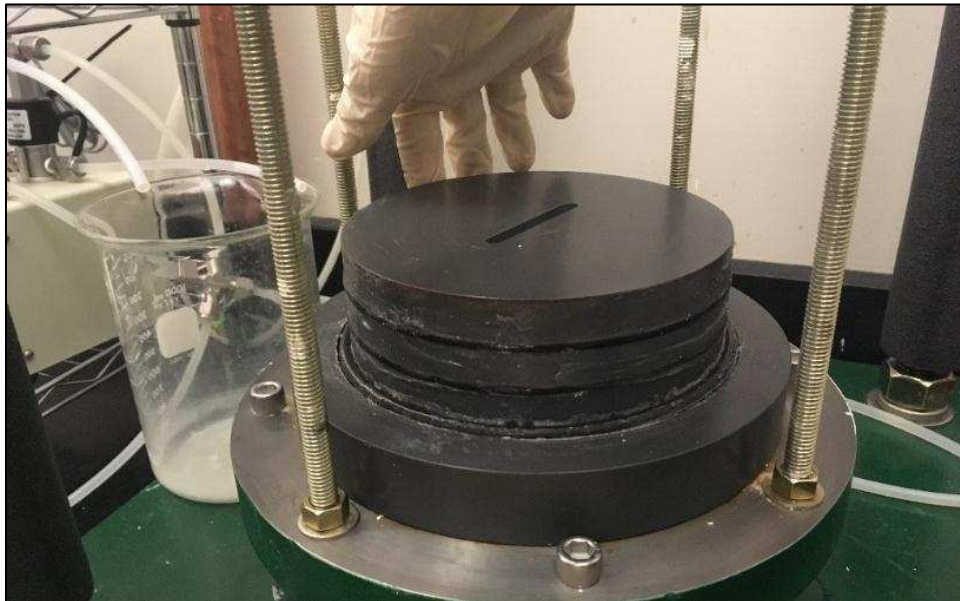


Fig. A.1. Apply vacuum grease to the edge of the sample pedestal

A.1.2 Place a saturated porous stone on top of the sample pedestal. Place a filter paper on top of the porous stone.



Fig. A.2. Filter paper and porous stone on top of the pedestal

A.1.3 Put the sample casing on top of the sample pedestal. Connect valves 11 and 12.

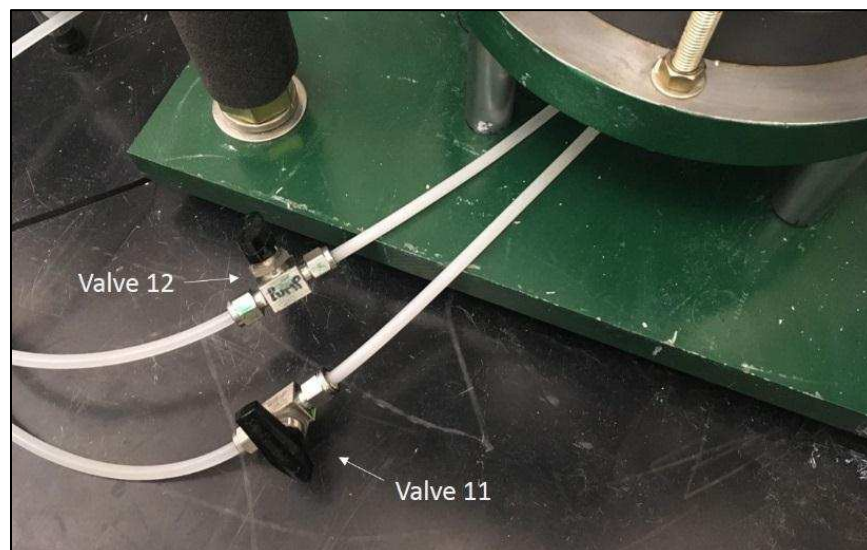


Fig. A.3. Valve 12 connects the pump to the sample; valve 11 connects to the pressure transducer

A.1.4 Saturate the lines leading into the sample casing through valves 11 and 12. To do this, open valves 5, 7, 8, 9, 11 and 17. Water from the Mariotte bottle and water bucket will flow into the sample casing. Close valves when air has been removed from the lines. Remove excess water from in sample casing using a syringe.

A.1.5 Check to ensure all other lines are free of air bubbles, including both syringes. If they are fully saturated, proceed to specimen preparation. In general, these lines should remain free of air and not require saturation.

A.1.6 If air exists in the inline pressure transducers (P1 and P2), open valves 5 and 7, 8 and 9. Unscrew P1 and water will begin to flow out. Tighten screw when air bubbles are no longer visible in the seeping water. Repeat this process for P2. Close the valves.



Fig. A.4. Removal of air bubbles at in line pressure transducers

A.1.7 If air exists in the inline differential pressure transducer (P3), open valves 5, 7, 8, 9, 18 and 19. Unscrew one side of P3 and water will begin to flow out. Tighten screw when air bubbles are no longer visible in the seeping water. Repeat this process for the other side of P3. Close the valves. This process is similar to Step 0.

A.1.8 If air exists in the syringes or the lines to the pump this should be removed. Air existing in syringes is removed by disconnecting the syringe, filling it with water and then holding it upwards and slowly squeezing the air bubble out.



Fig. A.5. Removal of air bubbles from syringe

A.1.9 Place the syringe back on the pump and fix it in place, do not reconnect the tubing yet.
Repeat with the other syringe.

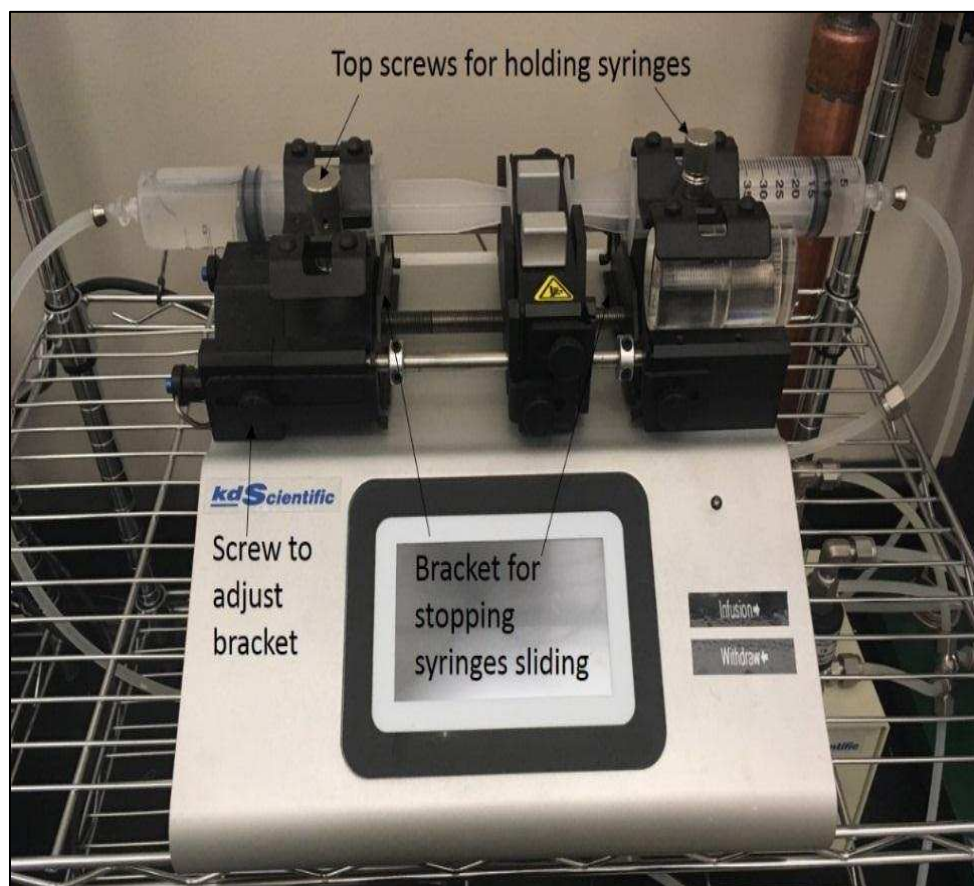


Fig. A.6. Pump Setup

A.1.10 Turn the flow pump and valve box on using the respective switch on the back of both devices. If the pump mode is set to infuse, it will move from left to right and valves 13 and 15 will be open in the valve box (the actuation light will be on when infuse is set). Open valve 17 and water should begin to flow through and out of the line to the left syringe. Attach the tube to the end of the syringe once all air bubbles have been removed. Close valve 17.



Fig. A.7. Removal of air from lines between sample and pump

A.1.11 Repeat the above step for the right syringe, but the pump should be set to withdraw, meaning that valves 14 and 16 will be open within the valve box.

A.2 Sample Preparation

A.2.1 Use a funnel to gently pour the slurry into the sample casing and stop pouring the slurry when the sample height is between 38 mm and 51 mm.

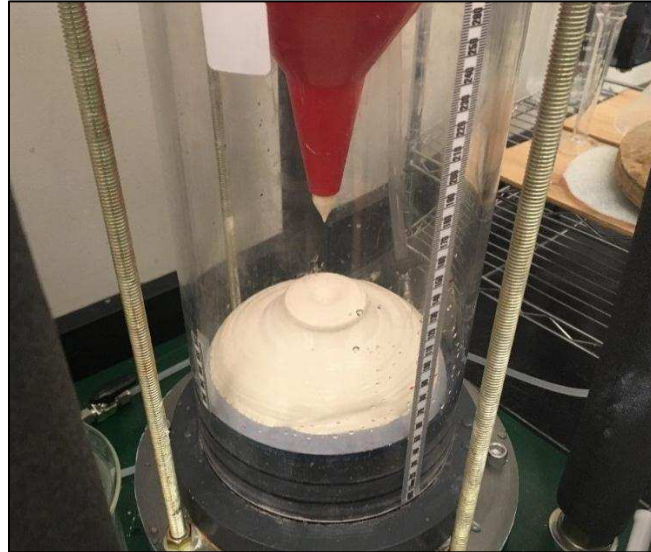


Fig. A.8. Placing slurry in sample casing

A.2.2 The prepared slurry sample should either have a horizontal surface or it should be slightly higher in the middle. With thicker slurries, gently shake the specimen to remove any voids and ensure a level surface and then record the initial height.



Fig. A.9. Shaking of specimen to provide level surface and remove any voids

A.2.3 Carefully add a filter paper to the stop of the slurry sample.

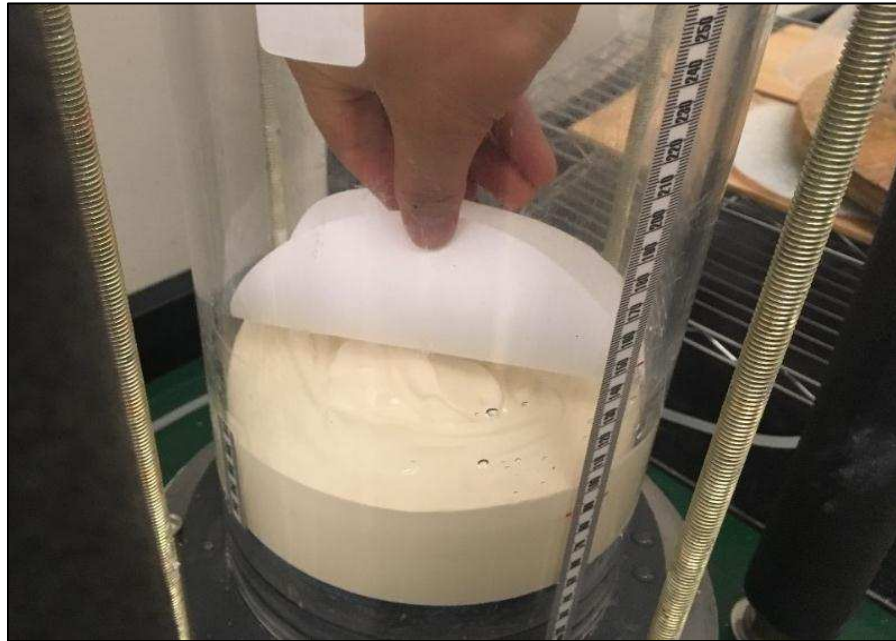


Fig. A.10. Placement of filter paper on top of specimen

A.2.4 Add water on top of the filter paper to a depth of approximately 70 mm. Use a syringe initially to avoid disturbing the sample.

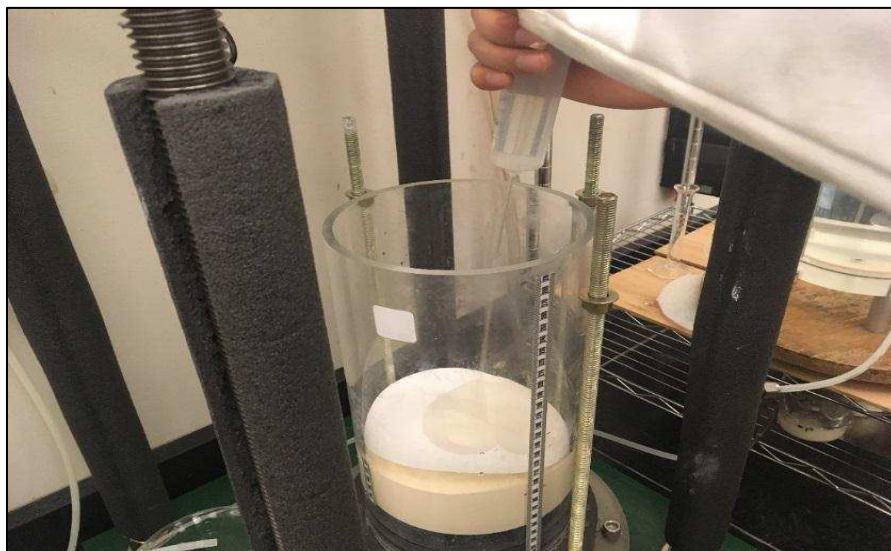


Fig. A.11. Carefully placing water on top of sample using a syringe to avoid disturbance

A.2.5 Once sufficient water is covering the sample, drop a plastic porous disc into the water. Wait two hours for the sample to consolidate under its own self weight if slurry samples are too soft.



Fig. A.12. Specimen with filter paper and porous plastic disc

A.2.6 After two hours, record the height of the sample from the attached ruler and open valves 5, 7, 11 and 12. Open the computer program and data will begin recording automatically. Be sure that the power supply regulator is also switched on. Place the loading plate on top of the sample. There should be sufficient water to completely submerge the plate. Ensure that the spaces for the LP extension rods are correctly aligned. Measure the change in height of the sample that occurs instantaneously and incorporate this in the data.

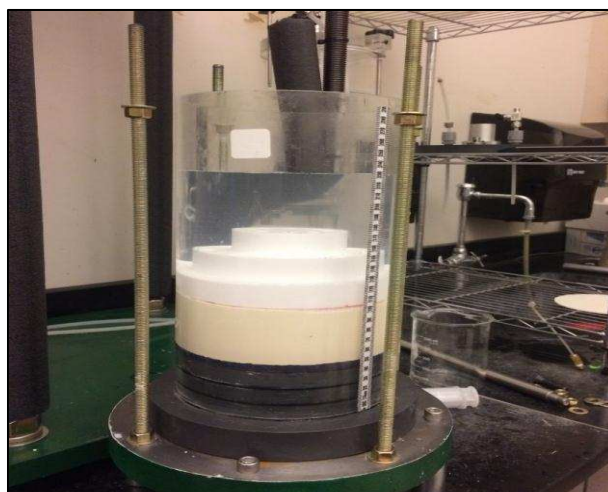


Fig. A.13. Specimen with loading plate in place

A.2.7 Put on top cap, tightening it in place with four washers and four nuts. Carefully slide the setup into position such that the loading shaft can be attached to the load cell and aligned with the center of the loading plate.



Fig. A.14. Top cap in place on top of sample casing

A.2.8 Install extension rods and two linear variable differential transformers (LP). Ensure they are vertical and that they are installed at exactly the same time. If one is installed first, the load from the single LP can cause the top cap to tip. Once LPs and extension rods are installed, zero LPs on the computer. Attach valve 6 and ensure that the height of the bottom of the bubbler tube is at or slightly above the current water height in the sample casing. The Mariotte bottle will maintain a constant pressure head at the top of the specimen.

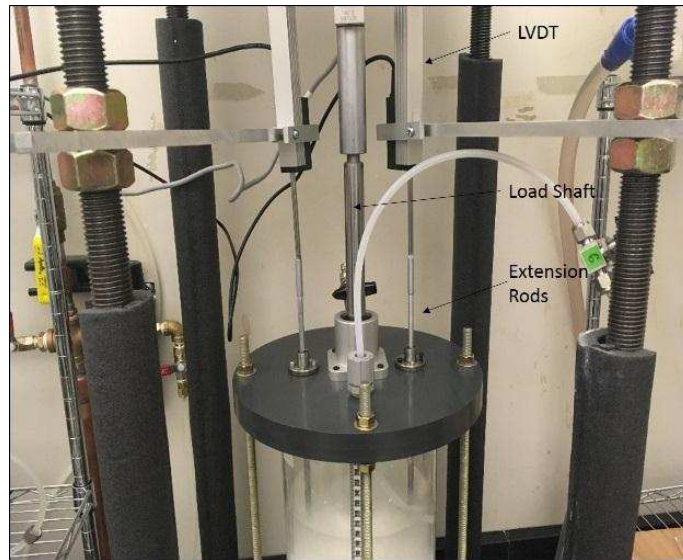


Fig. A.15. LPs, extension rods and load shaft in place and

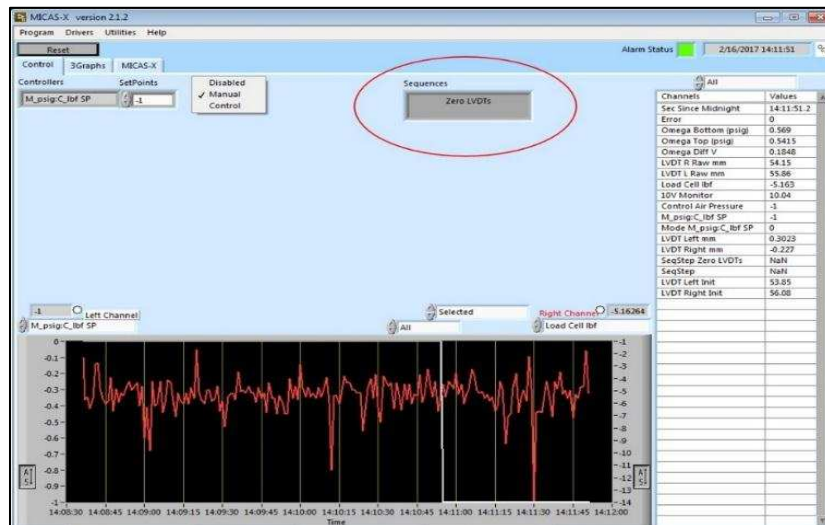


Fig. A.16. Button to zero LPs

A.2.9 Air in the line between the Mariotte bottle and the top of the sample needs to be flushed out. Ensure valve 5 and 6 are open. Using a hose attached to an external water source, slowly force water into the Mariotte bottle through the open bubbler tube. Continue until air is no longer present in the line.

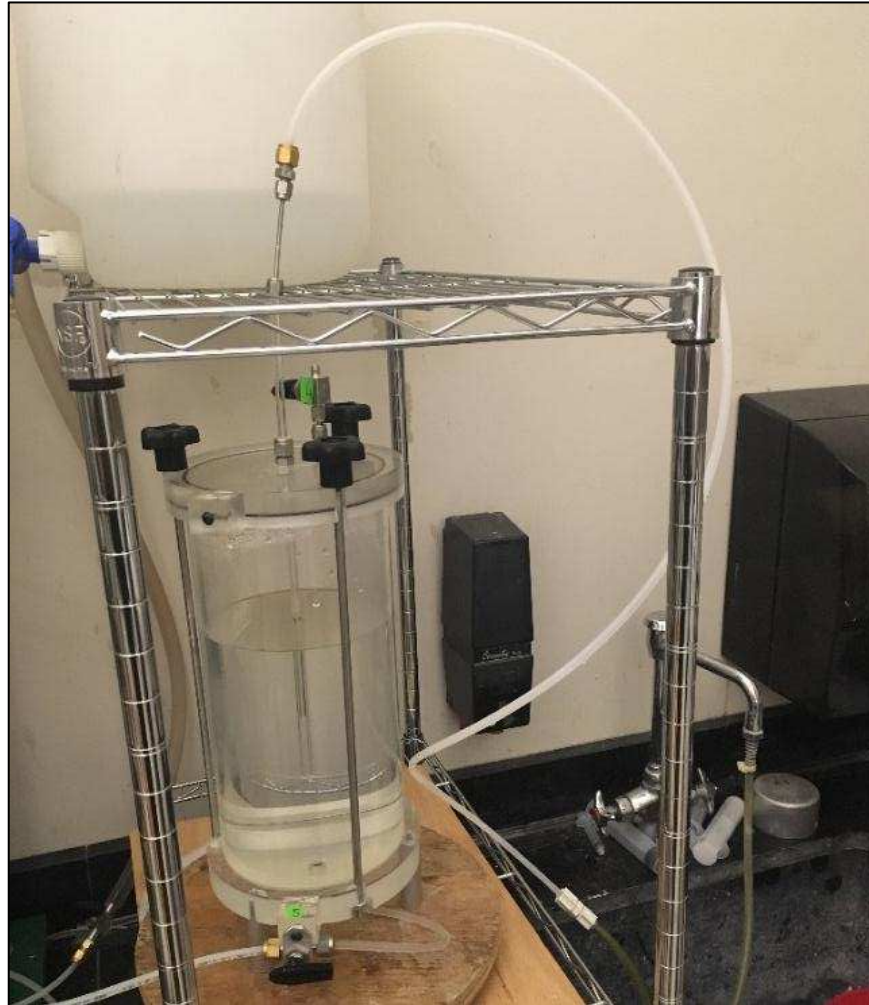


Fig. A.17. Flushing air out of line between top of sample and Mariotte bottle

A.3 Seepage Phase

A.3.1 Wait until consolidation has been completed under the external loads of the LPs and the loading plate. Consolidation is complete when the top pressure is equal to the bottom pressure.

A.3.2 Valves 5, 6, 7, 11, 12, 18 and 19 should be open during the seepage phase. The remaining valves should be closed. On the flow pump, select infuse/withdraw mode and set the flow rate to 0.14 mL/min (or any desired initial flow rate). The syringe should be custom 50 mL and the target volume should be 33 mL. The target volume refers to how far the syringe will move before switching mode to move the opposite direction. If this is too high, the pump will stall as it will have moved the maximum possible distance. Note, if the pump is stopped part way through a cycle it may be out of sync and will be unable to move the required target volume without stalling. If this is the case, when it's moved the maximum distance and is just about to stall, manually force the pump to switch in the opposite direction by selecting withdraw/infuse. It should now be in sync and not stall.

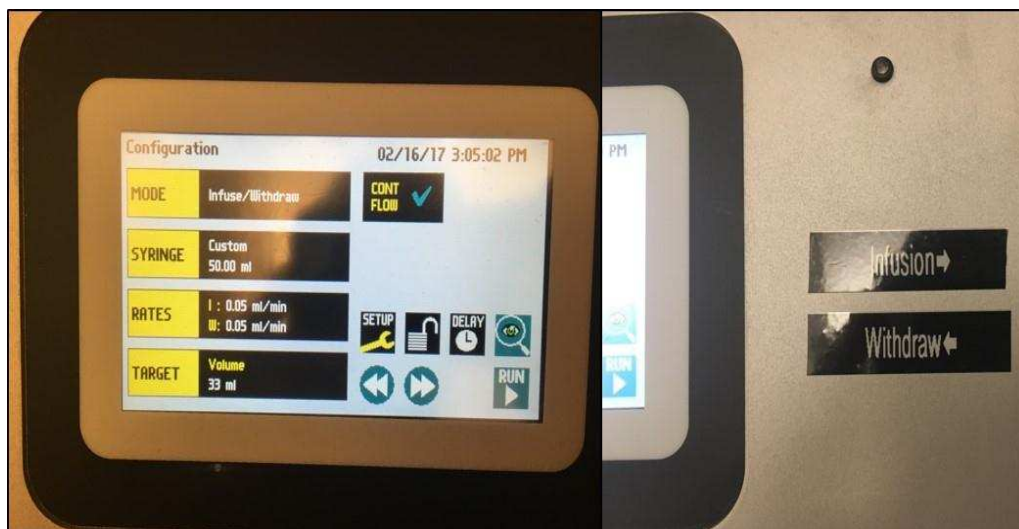


Fig. A.18. Display on flow pump (left), infusion/withdraw directions (right)

A.3.3 Press run and the first seepage phase will begin. Check the resulting seepage stress to ensure it is acceptable. If it is much lower than 1.5 kPa, increase the flow rate of the pump. If the seepage stress is larger than 10 kPa, a new slurry sample needs to be prepared as reducing the flow rate would lead to an overly consolidated sample. If the flow rate is set too high (i.e. higher than 2 mL/min), cavitation may occur (bubbles will appear where the water is being drawn from the sample – valve 12 line). If this occurs, the test is void and a new sample must be prepared.

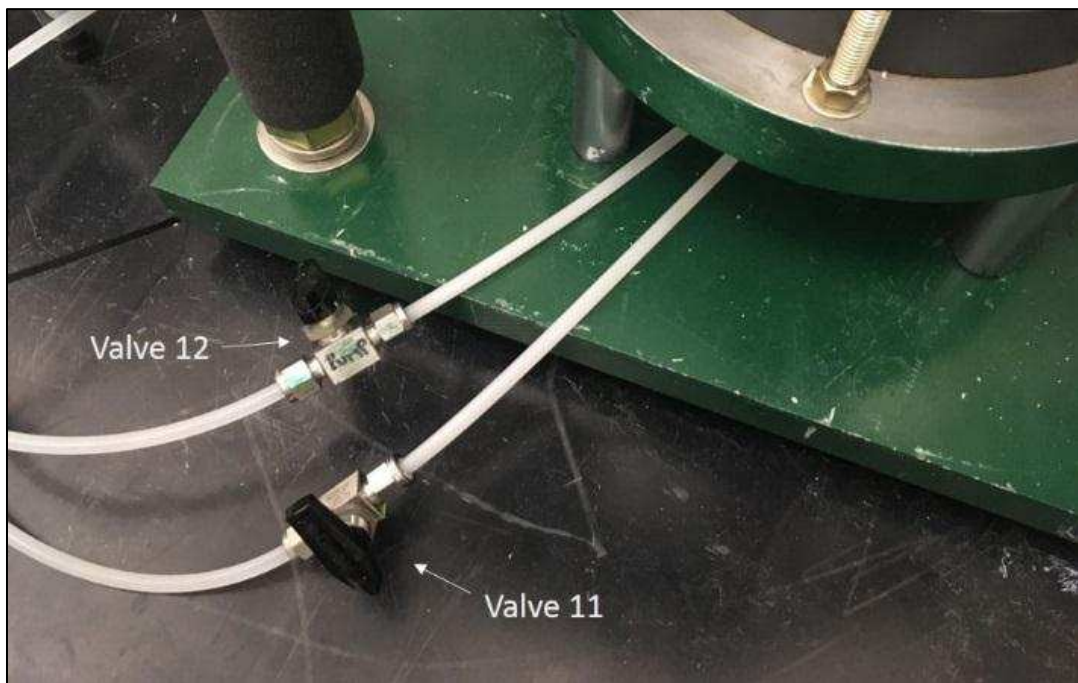


Fig. A.19. Bubbles will appear in the line connected to valve 12

A.3.4 Allow the flow pump to continue until steady state flow has been reached and deformation is no longer occurring. Record the flow rate, difference in pressure between top and bottom, and final sample height.

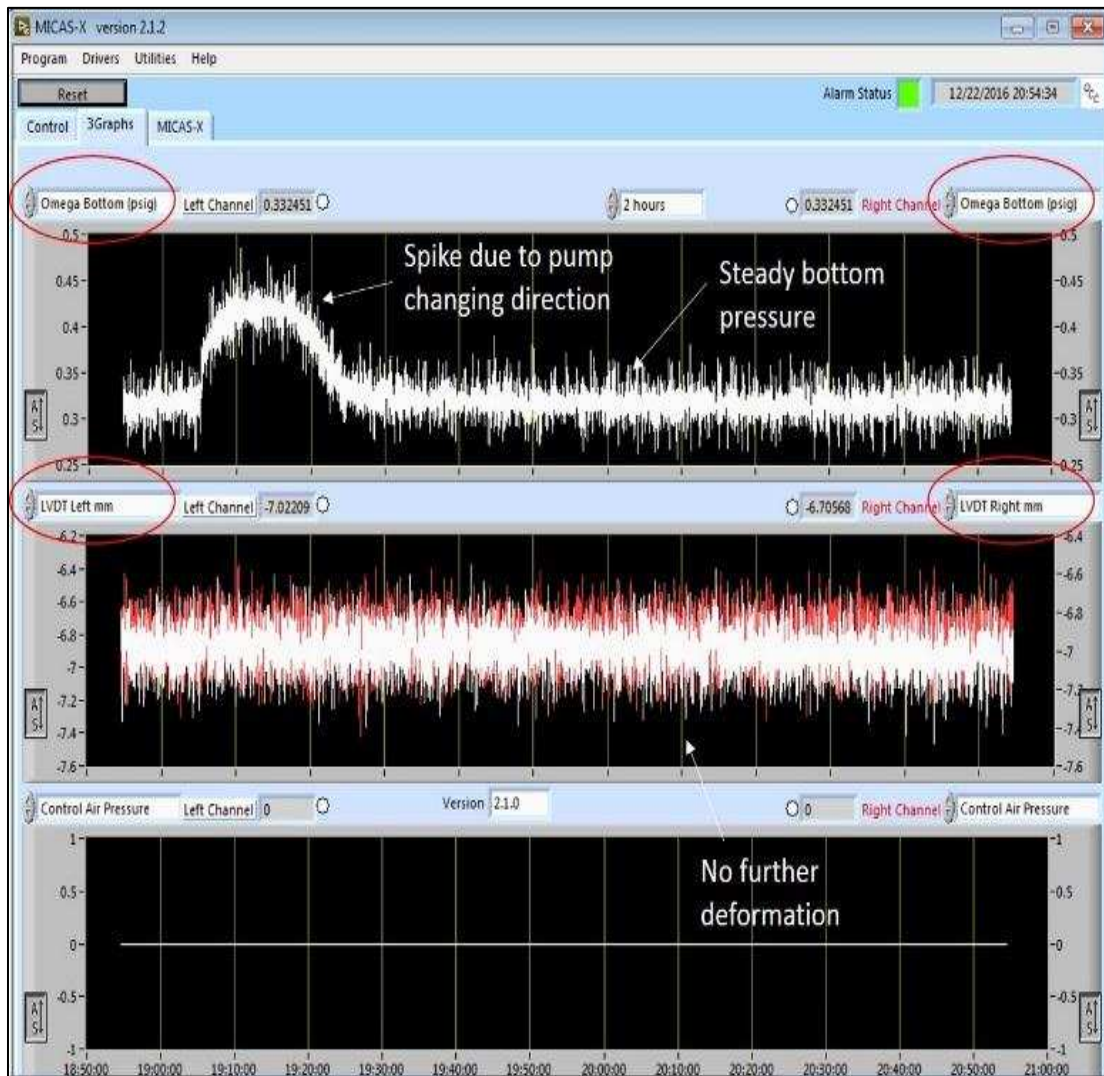


Fig. A.20. Example of steady state after seepage phase

B.3.5 Repeat for the number of load increments required.

A.4 Step Loading Phase

A.4.1 Close valves 12, 18 and 19. Valves 18 and 19 must be closed in order to avoid exceeding the capacity of the differential pressure transducer. Open valve 2. This will allow air flow into the air regulator to provide pressure for the step load.



Fig. A.21. Location of valve 2

A.4.2 Input the required load to be applied to the sample. The step load can be adjusted either using the manual or control setting. The manual setting input is in air pressure (psi) and represents the pressure that will be applied to the piston. The control setting input is in force (lbf) and represents the exact load applied to the sample.

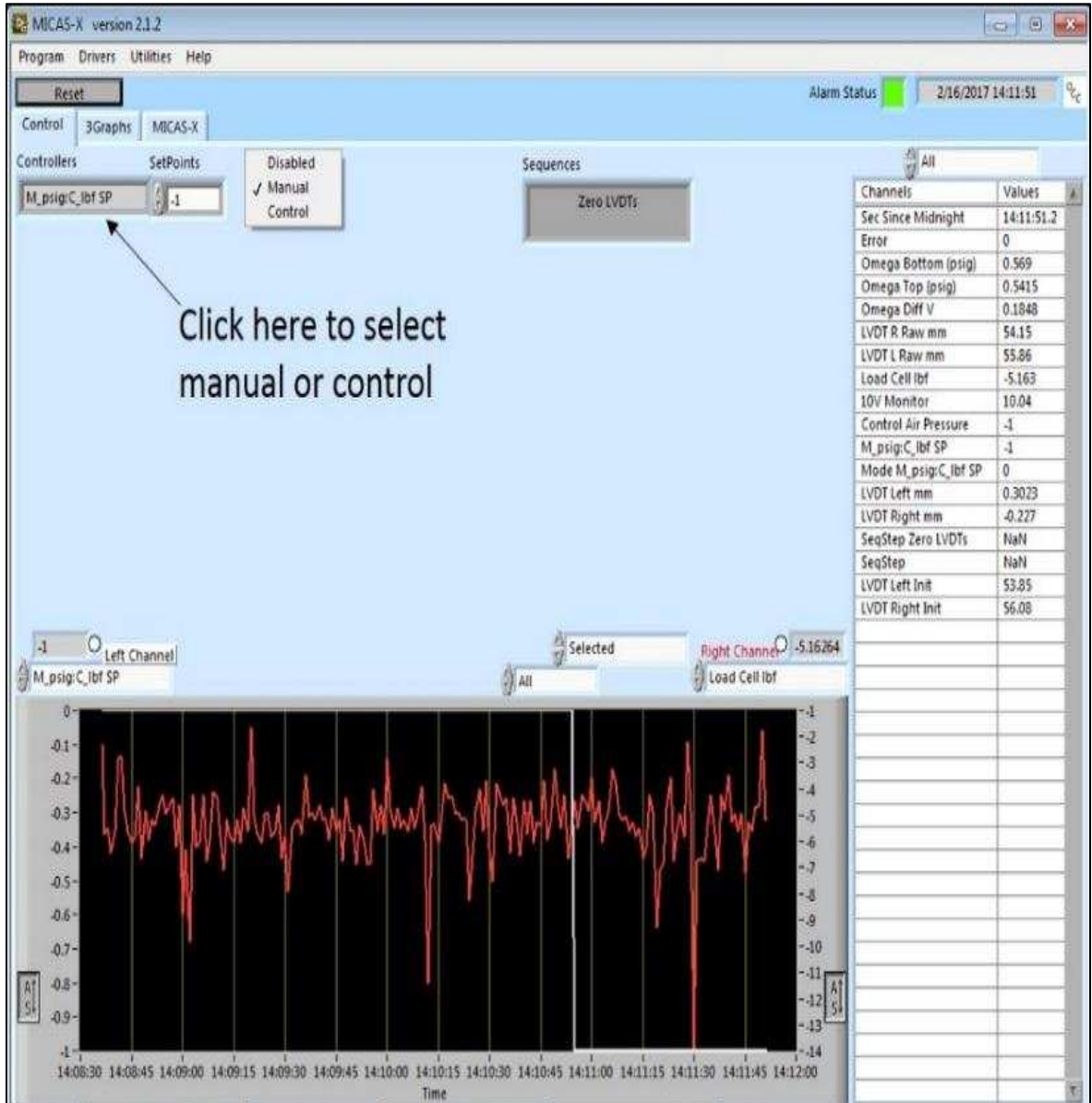


Fig. A.22. Selection of manual or control option for specifying load

A.4.3 The applied loading will cause an increase in pressure at the bottom of the specimen. This pressure will dissipate with time until a steady state has been reached where the top pressure essentially equals the bottom pressure. This is the end of the consolidation period. Record the change in height.

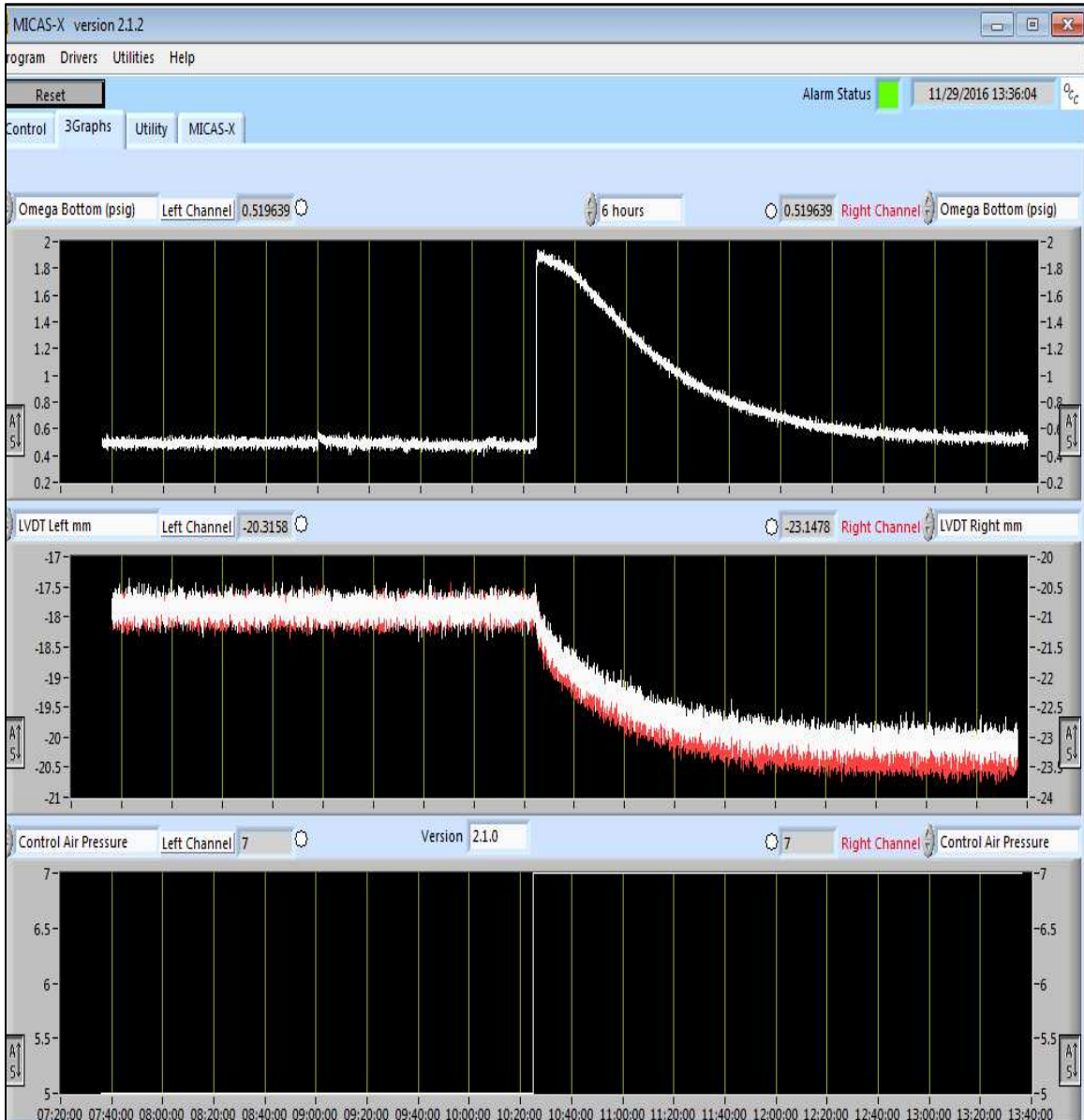


Fig. A.23. Example output showing steady state after step load phase

A.4.4 Once consolidation is complete, open valve 12 and turn the flow pump and valve box on. Open Valve 18 and 19 for more accurate measurement of pressure difference. Set the pump to approximately 1/10th of the first flow rate from the seepage phase. Allow the pump to run until steady state has been reached. Record the final steady state flow rate and pressure difference between the top and bottom. This is used to determine the hydraulic conductivity of the sample.

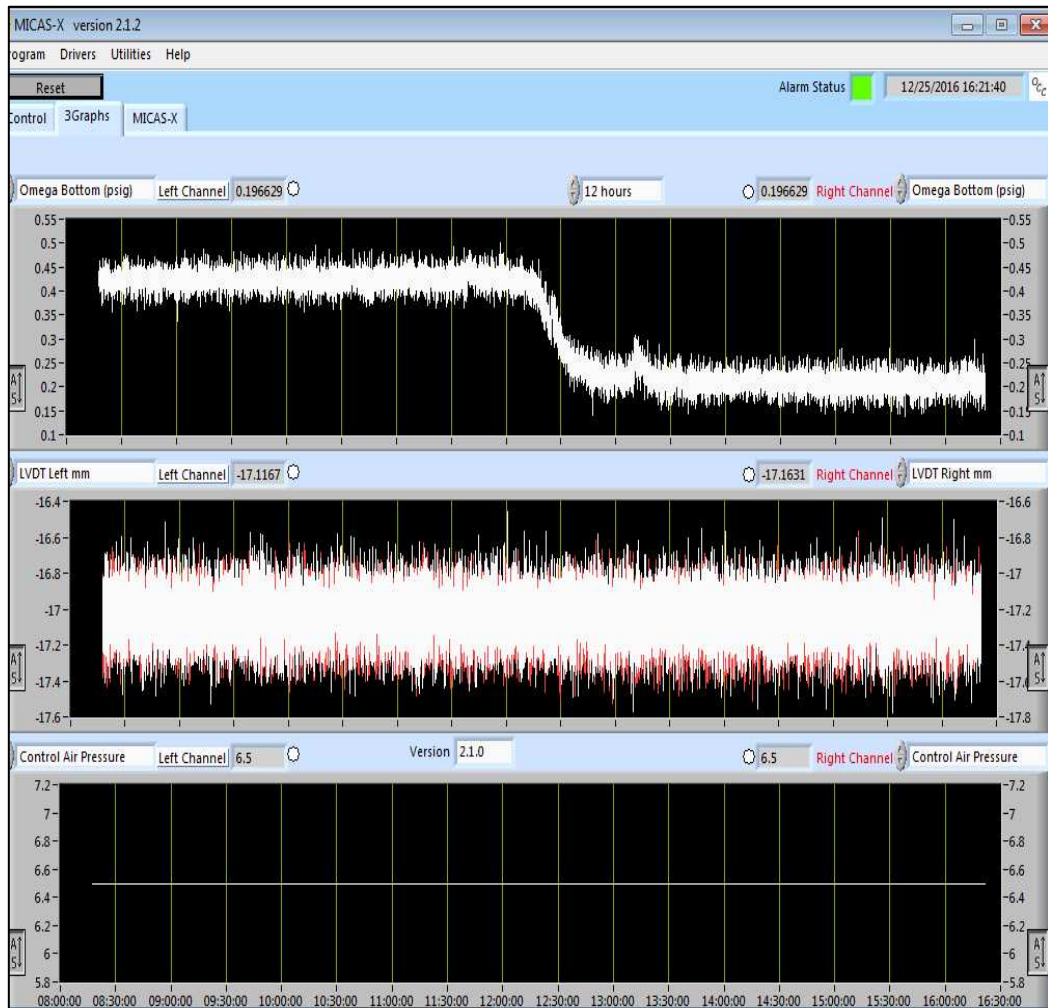


Fig. A.24. Example of steady state being reached during hydraulic conductivity test

B.4.5 Repeat the above steps for the number of required step loading increments.

A.5 Post Test

When all consolidation testing is complete, an oven test is performed on the consolidated slurry sample to calculate final void ratio and height of solids. These results are redundant but can be used to compare the results given by SICT program. ASTM D2216 requires that a specimen shall not be covered in a 105 °C oven if the specimen mass is larger than 200 grams. Typically, the consolidated slurry sample is approximately 500 grams and no cover was needed while oven drying the sample. Based on the area of soil specimen, weight of solids and unit weight of solids, height of solids was calculated by Eq. (A.1):

$$H_s = \frac{M_s}{\gamma_s \times A} = \frac{M_{cd} - M_c}{\gamma_s \times A} \quad (\text{A.1})$$

Where γ_s is the unit weight of solids, H_s is the height of solids, and A is the specimen area.

Based on phase diagram of soil sample (Fig. 2.1) and definition of void ratio, e_f shall be calculated by Eq. (A.2):

$$e_f = \frac{V_v}{V_s} = \frac{V_w}{V_s} = \frac{H_w}{H_s} = \frac{H_f - H_s}{H_s} \quad (\text{A.2})$$

Where V_v is the volume of voids, V_s is the volume of solids, V_w is the volume of water, H_w is the height of water, H_s is the height of solids, H_f is final height of soil specimen.

APPENDIX B: SICT CALIBRATIONS

B.1 Spring-return LP Calibration

Linear potentiometers (LP) are used to measure deformation during the seepage and step loading test phases and a photograph of the LP calibration device is shown in Fig. B.1. Dial gauge handle, digital dial gauge, extension rod, digital device clamp, LP clamp and flat work platform are included with the LP calibration device. A digital device clamp is used to provide a flat surface for all digital pieces. Additionally, the digital clamp holder is adjustable and allows the LP extension rod move back and forth. A digital dial gauge holder is used to accurately adjust the position of the extension rod when all digital pieces are fixed on the flat work platform. To calibrate, the position of the digital dial gauge holder is adjusted to zero before performing the test. The digital dial gauge is used to measure the deformation of the LP. A clamp is used to fix the LP on the flat work platform. The flat work platform is used to provide a flat surface for the LP calibration test. Tight LP in the LP clamp and then adjust the position of the extension rod. When the extension rod touches the LP without causing any deformation, fix all digital pieces and zero digital dial gauge. Adjust the position of extension rods from 0 mm to 4 mm by adjusting the dial gauge handler, record the voltage change generated from LP. Repeat this process until LP extension rod reaches the capacity of 28 mm. Next, place a known thickness of metal between LP and extension rod, and record the voltage change. Fig. 4.6 (a) and (b) shows calibration curves of left and right LPs developed for this study.

Because the capacity of both LPs is 100 mm, two extension rods are placed directly on top of the loading plate to make the connection between the LP and the loading plate. LP clamps are used to fix and provide a horizontal surface for the LPs. A schematic diagram of the extension rod and LP clamps is provided in Figs. 4.7 and 4.8. The LP clamp holder is shown in Fig. 4.9.

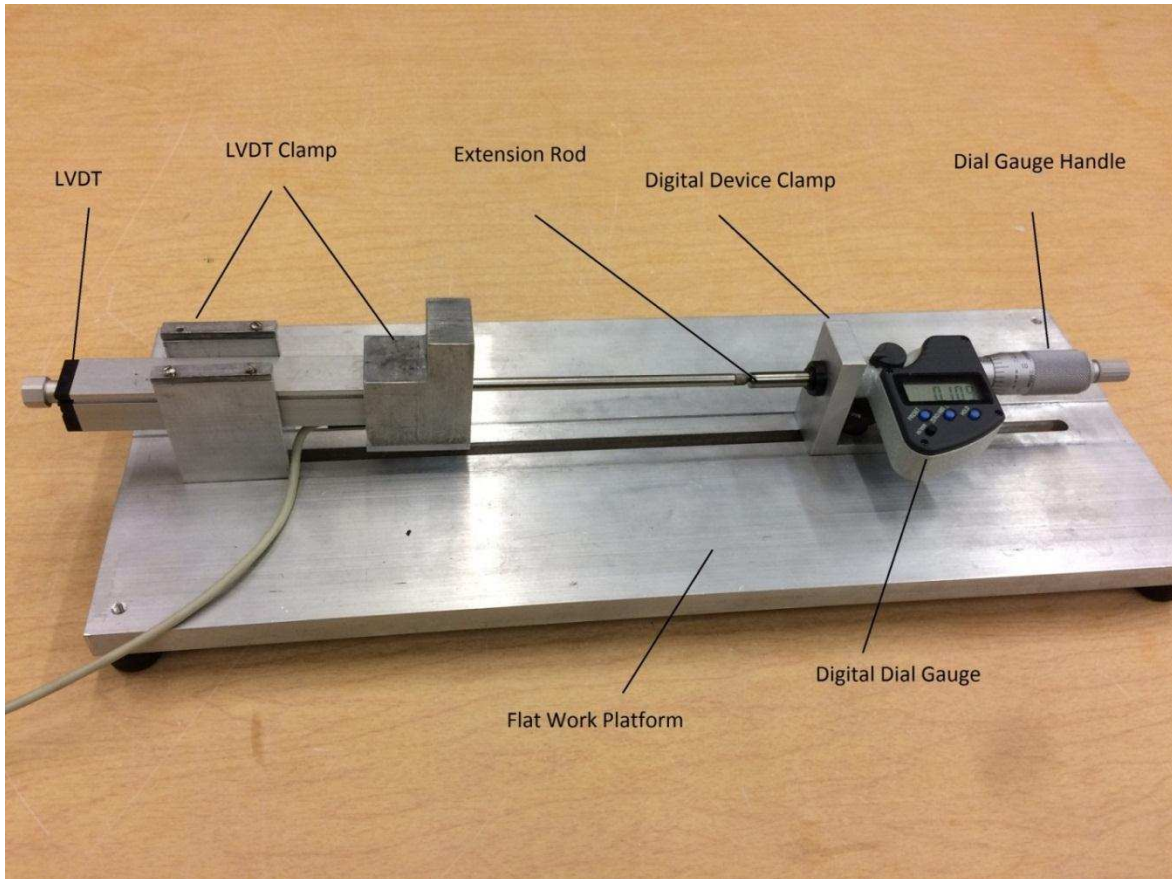


Fig. B.1. LP calibration device

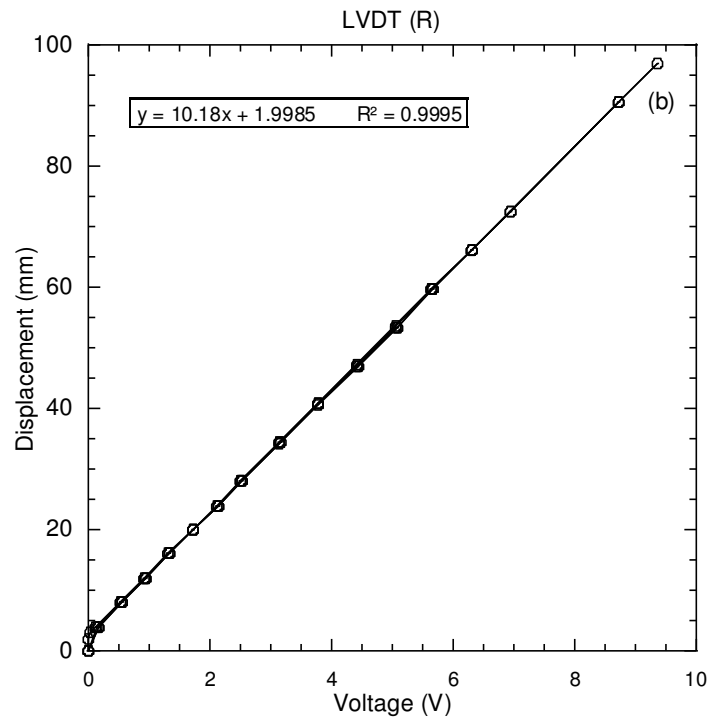
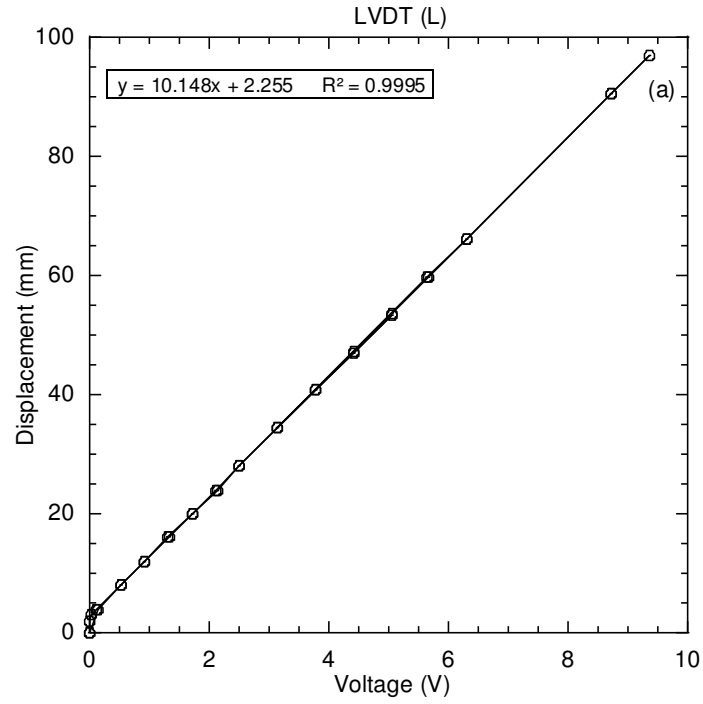


Fig. B.2. Calibration curve for (a) left LP, (b) right LP

B.2 Load Cell Calibration

A S-beam load cell (LC101-2.5K, Norwalk, CT) is used to measure the applied load from the air bellofram. The dead load method was used to calibrate the load cell. To calibrate, the load cell was placed on a rigid-flat surface and 20 kg rectangular metal plates (25.4 cm × 25.4 cm × 2.54 cm) were placed on the load cell, and the resulting voltage output was recorded. Next, a second nother 20 kg rectangular metal plate was placed on the existing weight, and the voltage was again recorded. This process was repeated in 20 kg increments until a total load of 220 kg had been added to the load cell. The resulting calibration curve for the load cell is provided in Fig. B.3.

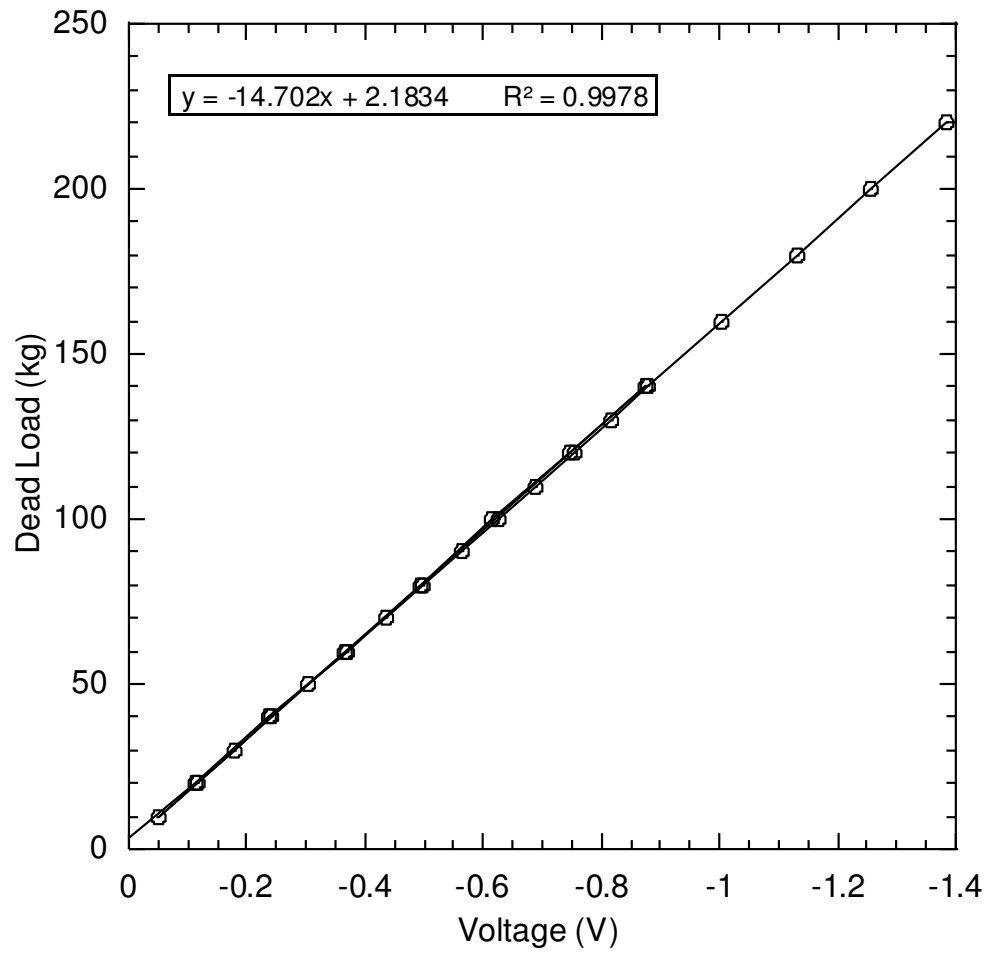


Fig. B.3. Calibration curve for load cell

APPENDIX C: VOID RATIO AT ZERO EFFECTIVE STRESS

The void ratio at zero effective stress (e_0) was determined for slurry material (kaolin clay, average synthetic tailings, fine synthetic tailings) prepared for each SICT (Znidarcic 1994). A sedimentation test was conducted with 50 g of dry soil mixed similarly to the sedimentation tests described previously, but subsequently separated and placed into two beakers with an inside diameter of 67 mm and height of 101 mm. The slurries were allowed to settle and consolidate for several days, whereupon supernatant liquid was removed and a sample of the settled materials were removed and evaluated for water content. The e_0 was then computed from the water content, G_s , and assuming complete saturation.

To study the relationship between e_0 and specimen height, five beakers with an inside diameter of 67 mm and height of 101 mm were used to store kaolin clay. Previous test showed that the sedimentation was insignificant if SC was bigger than 30%. SC of 25% was chosen for the study and slurry sample with heights of 25 mm, 38 mm, 50 mm, 64 mm, and 76 mm were poured into these five beakers through a funnel with an inflow diameter of 90 mm and outflow diameter of 5 mm. The drop height of slurry sample was 10 mm. The relationship between e_0 and ratio of inside diameter to slurry height is shown in Fig. C.1.

In Fig. C.1, no strong relationship was shown between e_0 and ID/H and the difference between the highest e_0 and lowest e_0 was smaller than 0.3. The variations of e_0 may be caused by the human error since supernatant water was hard to fully remove from the beaker resulting the variations of water content. However, the average of these five e_0 was close to 5.35 and the ratio (ID/H) 1.7 was chosen for the determination of e_0 in SICT.

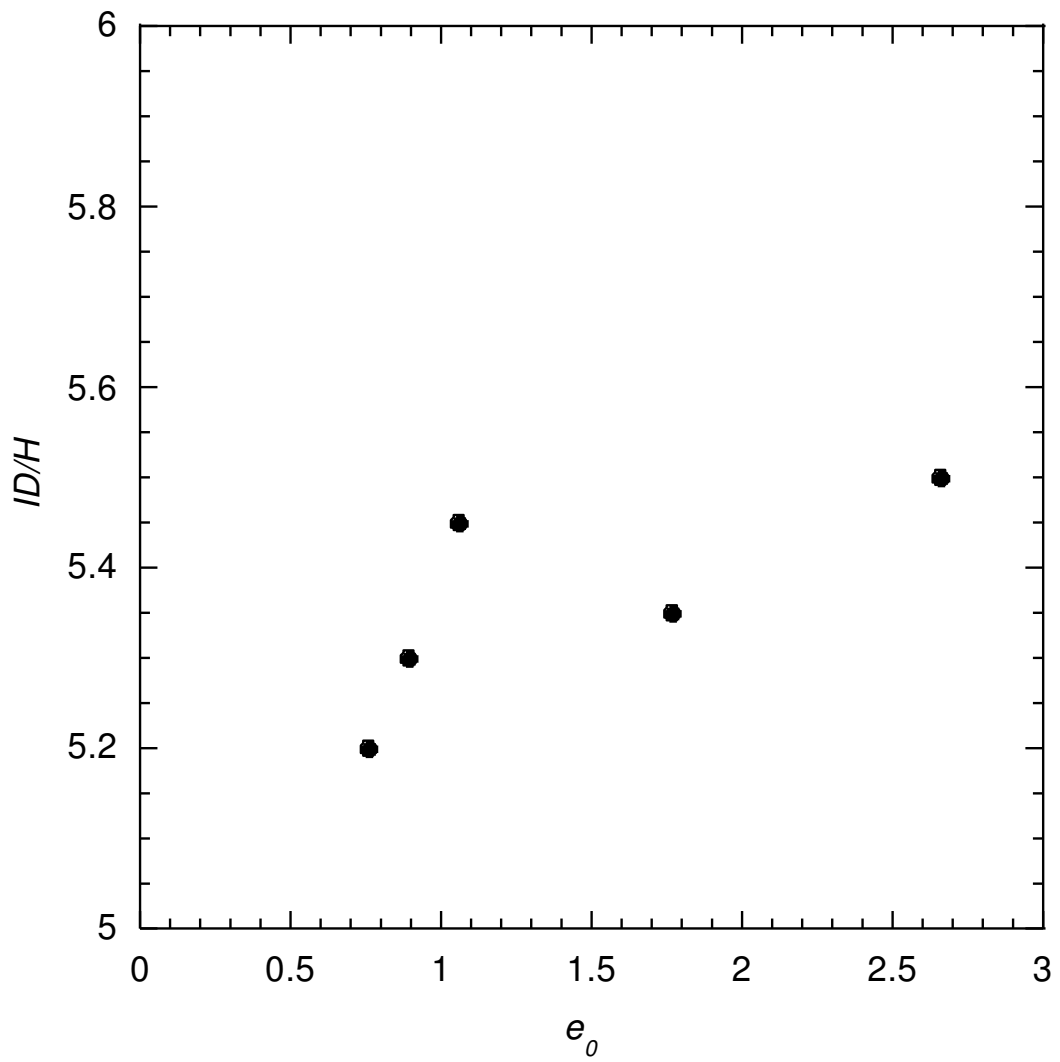


Fig. C.1. The relationship between e_0 and aspect ratio of container